

MULTIPLE SCATTERING IN WIDE-FIELD OPTICAL COHERENCE TOMOGRAPHY

THÈSE N° 3001 (2004)

PRÉSENTÉE À LA FACULTÉ SCIENCES ET TECHNIQUES DE L'INGÉNIEUR

Institut d'imagerie et optique appliquée

SECTION DE MICROTECHNIQUE

ÉCOLE POLYTECHNIQUE FÉDÉRALE DE LAUSANNE

POUR L'OBTENTION DU GRADE DE DOCTEUR ÈS SCIENCES

PAR

Boris KARAMATA

ingénieur en microtechnique diplômé EPF
de nationalité suisse et originaire de Genève (GE)

acceptée sur proposition du jury:

Prof. T. Lasser, directeur de thèse
Prof. C. Boccara, rapporteur
Prof. R. Dändliker, rapporteur
Dr M. Kempe, rapporteur
Dr P. Lambelet, rapporteur

Lausanne, EPFL
2004

“Les causes primordiales ne nous sont point connues; mais elles sont assujetties à des lois simples et constantes, que l'on peut découvrir par l'observation, et dont l'étude est l'objet de la philosophie naturelle”

J. Fourier, 1822

Théorie analytique de la chaleur (extrait du “Discours préliminaire”)

Abstract

Optical Coherence Tomography (OCT), a well-established imaging method based on low-coherence interferometry, provides cross-sectional images of the internal structure of biological samples with a resolution in the micrometer range. OCT was successfully applied on various tissues such as for instance the retina, the skin or a tooth. In highly scattering tissues like the skin, probing depth is limited to approximately 2mm, mainly due to insufficient rejection of multiply scattered light. Presently, the contribution of multiple scattering in OCT is not fully understood. Therefore, there is a strong and urgent need to develop models allowing a reliable evaluation of the system's limitations as well as the improvement of the imaging capabilities. It is generally believed that a relevant model should account for loss of correlation between the reference and the sample field due to multiple scattering.

We developed a new comprehensive model of OCT. Our preliminary study revealed that the reference and sample fields are actually fully correlated. This important result allowed us to model the OCT signal as a sum of stationary random phasors and treated it as a statistical signal. The mean of this signal can be calculated thanks to classical results of statistical optics and to a Monte Carlo simulation. Unlike other existing models, our model accounts for the source autocorrelation function. The model proved to be in excellent agreement with a whole range of experimental data gathered in a comprehensive study of cross-talk in wide-field OCT. Moreover, our results put in question the applicability of widely used models of OCT based on the "extended Huygens-Fresnel principle", which assume a partial correlation between interfering fields due to multiple scattering.

The construction of conventional OCT images is based on lateral scanning of a beam focused within the sample. To increase image acquisition speed and eliminate the need for lateral scanning, wide-field OCT was recently developed. Our experimental and theoretical investigations of the potential and limitations of wide-field OCT revealed the crucial role played by the spatial coherence of the light source. Spatially coherent illumination generates considerable coherent optical cross-talk, which prevents shot-noise-limited detection and diffraction-limited imaging in scattering samples. The dependence on several parameters of the optical system and of the sample properties was investigated in a comprehensive study. Cross-talk increases with the wide-field diameter, numerical aperture, source coherence length, and sample optical density; and strongly depends on sample anisotropy. We showed that spatially incoherent illumination realized with a thermal light source permits cross-talk suppression in wide-field OCT, i.e. rejection of multiply scattered light to a level comparable to that of point scanning OCT. We performed a theoretical study which revealed that the power per spatial mode radiated by thermal light sources is too low to permit a high signal-to-noise ratio while maintaining a fast acquisition speed. Therefore, wide-field OCT realized with either spatially coherent or spatially incoherent illumination suffers from inherent fundamental limitation.

This led us to investigate the possibility of exploiting a spatially incoherent light source brighter than a thermal light source. We came to the conclusion that such a "pseudothermal" light source can potentially lead to wide-field OCT systems devoid of cross-talk and an image acquisition speed higher than that of a point scanning OCT system. However, the attractive properties of pseudothermal light sources could be gained at the expense of the simplicity and the economical advantages offered by thermal light sources. Furthermore, fast acquisition speed also relies on a performing "smart pixel detector array". Presently, such detectors do not have sufficient sensitivity and their frequency read-out is too low as shown in our feasibility study.

We performed a theoretical investigation of the potential of thermal light sources in terms of axial resolution and power per mode. The former revealed that the maximum power per mode is radiated at a wavelength higher than the spectral peak of a blackbody radiator. This led to the important practical conclusion that, at 6000 K, the maximum power is collected in the therapeutic spectral window in OCT (600 - 1300 nm), while at 3000 K this peak is shifted out of the therapeutic window leading to significant power losses. More generally, our work provides a design tool for choosing the optimal thermal light source for a given therapeutic window in terms of signal-to-noise ratio. Currently available sources at 6000 K consist of high pressure gas arc lamps providing a spectrum endowed with

spectral lines deleterious for OCT. By suppressing a portion of the spectrum devoid of spectral lines of a mercury arc lamp, we obtained amongst the highest axial resolution so far reported in OCT.

Furthermore, the importance of the speckle statistics in OCT incited us to clarify the origin of a difference between two theoretical results reported in the literature. Indeed, two calculations of the amplitude distribution of speckles in OCT, each of them based on a different mathematical formulation, yield different results. We showed that a modification of an initial assumption in one of the formulation leads to equivalent results.

In conclusion, this thesis provides a deeper understanding of the potential and limitations of wide-field OCT, leading to important design rules. Moreover, it presents a new comprehensive model of OCT putting in question other widely used models.

Version abrégée

La tomographie par cohérence optique, plus connue sous son acronyme anglais OCT, pour “Optical Coherence Tomography”, est aujourd’hui une méthode d’imagerie reconnue. Reposant sur l’interférométrie en basse cohérence, elle permet d’obtenir des images en coupe de la structure interne d’échantillons biologiques avec une résolution micrométrique. L’OCT permet d’obtenir des images probantes de divers tissus tels que la rétine, la peau ou les dents. Dans les tissus fortement diffusants comme la peau, la profondeur observable demeure limitée à environ 2mm principalement à cause de l’élimination insuffisante de la lumière ayant subi de la diffusion multiple. Actuellement, la contribution de la lumière diffuse en OCT n’est pas encore parfaitement comprise. Par conséquent, le développement de modèles permettant une meilleure compréhension des limitations d’un système d’imagerie OCT ainsi l’amélioration de ses performances, revêt une importance grandissante. Il est généralement reconnu qu’un modèle pertinent devrait tenir compte de la perte de corrélation entre les champs provenant du bras de référence et l’échantillon, causée par la lumière ayant subi de la diffusion multiple.

Nous avons développé un nouveau modèle complet de l’OCT. Notre étude préliminaire a révélé que les champs provenant de la référence et de l’échantillon sont en fait parfaitement corrélés. Ce résultat important nous a permis de modéliser un signal OCT comme somme de phaseurs aléatoires et de la traiter comme signal statistique. La moyenne d’un tel signal OCT peut être calculée en exploitant des résultats notoires de l’optique statistique et utilisant une simulation de Monte Carlo. Contrairement à d’autres modèles existants, notre modèle tient compte de la fonction d’autocorrélation de la source lumineuse. Le modèle s’est montré être en excellent accord avec un grand nombre de données expérimentales obtenues à partir d’une vaste étude sur la lumière cohérente parasite (cross-talk) en OCT à champ large. De plus, nos résultats remettent en question l’applicabilité de modèles très répandus de l’OCT basés sur ladite “extension du principe de Huygens-Fresnel”, qui supposent une corrélation partielle entre les champs interférant à cause de la diffusion multiple.

En OCT classique, l’image est obtenue par le biais du balayage latéral d’un faisceau focalisé dans l’échantillon. Afin d’augmenter la vitesse d’acquisition et de passer outre le balayage latéral, l’OCT à champ large a été développée récemment. Nous avons réalisé une étude expérimentale et théorique sur le potentiel et les limitations intrinsèques de l’OCT à champ large, laquelle nous a permis de démontrer le rôle crucial joué par la cohérence spatiale de la source. Une illumination spatialement cohérente génère de la lumière cohérente parasite en quantité empêchant ainsi une détection de signaux limitée par le bruit quantique de même qu’une imagerie limitée par la diffraction. L’influence de plusieurs paramètres du système optique ainsi que de certaines propriétés de l’échantillon ont fait l’objet d’une étude complète. La lumière cohérente parasite augmente avec le diamètre du champ large, l’ouverture numérique, la longueur de cohérence de la source, et la diffusion de l’échantillon; et dépend fortement de l’anisotropie de l’échantillon. Nous avons démontré qu’en OCT à champ large, une illumination spatialement incohérente obtenue à partir d’une source lumineuse thermique ramène le niveau de lumière cohérente parasite, c-à-d le niveau de la lumière ayant subi de la diffusion multiple, à celui atteint en OCT par balayage de faisceau. Par une étude théorique nous avons montré que la puissance émise par une source thermique est trop faible pour parvenir à un rapport signal/bruit élevé tout en maintenant une vitesse d’acquisition élevée. Par conséquent, l’OCT à champ large, réalisée soit en illumination cohérente, soit en illumination incohérente, souffre d’une limitation spécifique fondamentale.

Ceci nous a amené à étudier la possibilité d’utiliser une source lumineuse spatialement incohérente de brillance plus élevée qu’une source thermique. Nous en avons conclu qu’une telle source dite “pseudo-thermique” rend possible la conception de systèmes OCT en champ large exempts de lumière cohérente parasite, tout en permettant une vitesse d’acquisition plus élevée qu’en OCT à balayage de faisceau. Cependant, les propriétés séduisantes de telles sources ne peuvent être obtenues qu’au détriment de la simplicité et du bas coût offert par les sources lumineuses thermiques. Autre fait à considérer; la possibilité d’obtenir une vitesse d’acquisition d’image élevée nécessite une matrice de

détecteurs “intelligents” très performants. Actuellement, de tels détecteurs ne sont pas assez sensibles et leurs cadences de lecture demeurent trop faibles comme démontré lors de notre étude de faisabilité.

Nous avons réalisé une étude théorique sur le potentiel des sources lumineuses thermiques en terme de résolution axiale et de puissance par mode. Cette première a révélé que la puissance maximale par mode est émise à une longueur d’onde plus élevée que le pic de radiation spectrale d’un corps noir. Nous en tirons la conclusion importante du point de vue pratique, à savoir qu’à 6000 K, le maximum de puissance est collecté dans la “fenêtre spectrale thérapeutique” utilisée en OCT (600 - 1300 nm), alors qu’à 3000 K ce maximum est déplacé en dehors de la fenêtre thérapeutique causant d’importantes pertes de puissance. Les sources couramment disponibles à 6000 K consistent en des lampes à arc contenant du gaz sous haute pression qui fournissent un spectre avec des lignes spectrales néfastes pour l’OCT. Toutefois, en supprimant les bandes spectrales d’une lampe à arc à mercure, nous avons obtenu une résolution axiale en OCT parmi les plus élevées rapportées à ce jour.

De plus, l’importance que revêt la statistique des speckles en OCT nous a incité à clarifier l’origine de la différence entre deux résultats théoriques publiés. En effet, deux calculs de la distribution de l’amplitude des speckles en OCT, chacun d’eux basé sur une formulation mathématique différente, mènent à des résultats différents. Nous avons montré qu’une modification d’une hypothèse de base dans l’une des formulations donne des résultats identiques dans les deux cas.

Cette thèse permet une compréhension approfondie du potentiel et des limitations de l’OCT à champ large débouchant sur d’importantes règles de conception de tels systèmes. De plus, elle présente un nouveau modèle de l’OCT remettant en cause d’autres modèles largement répandus.

Contents

Abstract	i
Version abrégée	iii
Chapter I: Introduction	1
1.1 Imaging in scattering tissues	1
1.2 Optical Coherence Tomography (OCT)	2
1.2.1 Imaging performance	2
1.2.2 Wide-field OCT	3
1.2.3 Speckles	3
1.2.3 Models for OCT	4
1.3 Goals and structure of the thesis	5
References	6
Chapter II: Light coherence and speckles	9
2.1 Light coherence	10
2.1.1 Degree of coherence	10
2.1.2 Coherence and interference	12
2.1.3 Coherence volume	15
2.2 Speckles	17
2.2.1 Background	17
2.2.2 Speckle statistics in OCT	19
References	24
Chapter III: Wide-field optical coherence tomography with spatially coherent illumination	25
3.1 Wide-field OCT in scattering samples	27
3.1.1 Introduction	27
3.1.2 Method	27
3.1.3 Results and discussion	29
3.1.4 Conclusions	32
3.2 Modeling multiple scattering in OCT	33
3.2.1 Introduction	33
3.2.2 Preliminary experiment	34
3.2.3 Multiple scattering and interference	35
3.2.4 Model	37
3.2.5 Preliminary results and analyses	42

3.2.6 Discussion	43
3.2.7 Conclusions	45
3.3 Experimental and theoretical investigation of cross-talk in wide-field OCT	47
3.3.1 Introduction	47
3.3.2 Method	47
3.3.3 Cross- talk measurements	49
3.3.4 Results and discussion	51
3.3.4 Conclusions	56
References	58
Chapter IV: Wide-field optical coherence tomography	
with spatially incoherent illumination	61
4.1 Cross-talk suppression	61
4.2. Spatial coherence gating with a thermal light source	64
4.2.1 Method	64
4.2.2 Results	66
4.2.3 Conclusions	68
4.3. Ultrahigh axial resolution	69
4.4 Power considerations for thermal light sources	73
4.4.1 Theory	73
4.4.2 Results and analyses	75
4.4.3 Signal to noise ratio	77
4.5. Wide-field OCT with a pseudothermal light source	79
4.5.1 Method and principle	79
4.5.2 Results and discussion	81
4.5.3 Conclusions	82
Reference	84
Chapter V: Conclusions and perspectives	85
Acknowledgements	89
Curriculum Vitae	91

CHAPTER I

Introduction

1.1 Imaging in scattering tissues

Scientific progress is often triggered by improved instrumentation extending the perception of our environment. Charles-Eugene Guye wrote: “C'est l'échelle d'observation qui créé le phénomène”¹. Optical instruments undoubtedly had a tremendous impact on the development of science, while the telescope and the microscope helped unravel many mysteries of the macro and microscopic world. In particular, biology largely benefited from the advent of the microscope. However, in the field of medical imaging, instruments based on other physical principles such as magnetic resonance, ultrasounds, or computerized tomography with X-rays, are preferred to optical modalities. The main reason for this is the size of relevant biological structures in the range of optical wavelengths, which leads to considerable scattering and prevents in-depth imaging.

However, the past decade witnessed the emergence of several valuable optical methods allowing in-depth imaging through turbid biological samples. In medicine, their ultimate goal is a non-invasive diagnosis with a resolution sufficient to avoid biopsy. These novel methods are based on technological developments, rather than on a major physical breakthrough. New laser light sources and increasingly performing computers made possible the implementation or improvement of traditional optical detection methods. In addition to avoiding contact with and ionization within tissues, optical modalities have the advantage of higher a resolution than that of the above mentioned methods. Their main weakness, the limited penetration depth due to scattering, makes optical methods complementary to other existing methods.

A major issue with all optical methods is the detection of extremely weak signals, i.e. the achievement of the highest possible signal to noise ratio. In most practical cases, very little light is backscattered from biological structures due to the low refractive index difference between them and the surrounding aqueous media. In addition, most of the light is lost through scattering. For diffraction-limited imaging, only ballistic light, whose intensity decreases exponentially with the sample thickness according to the Lambert-Beer law, mediates useful information. Therefore, for a given source brightness and a shot-noise limited system, the probing depth is in principle ultimately

¹ “It is the scale of observation that generates the phenomenon”

limited by the number of scattering mean-free paths [1,2]. However, residual multiply scattered light reduces the contrast, the resolution as well as the maximum probing depth. The major challenge for imaging in turbid media with diffraction-limited performance is to efficiently reject multiply scattered light while keeping ballistic light. To realise this, various physical principles are exploited, such as for instance spatial filtering, time resolved detection or coherent detection [3]. The well known confocal microscope is based on spatial filtering. Multiply scattered light rejection accomplished in confocal imaging system has been extensively investigated both theoretically and experimentally [4]. Substantially better discrimination can be obtained when combining confocal spatial filtering with temporal coherence gating, as in optical coherence tomography (OCT) [5,6]. However multiple scattering still remains the main limiting factor in highly scattering media as shown by various studies [2,7].

1.2 Optical coherence tomography

Optical coherence tomography (OCT) is now a well-established imaging method based on low-coherence interferometry providing cross-sectional images of the internal structure of biological samples with a resolution in the micrometer range. Besides its excellent rejection of multiply scattered light as seen in 1.1, OCT achieves a high signal to noise ratio (SNR) by exploiting heterodyne detection. The method was used successfully for imaging various tissues such as the retina [8], skin [9] or a tooth [10]. In highly scattering tissues such as the skin, probing depth is limited to approximately 2 mm.

Over the past few years, OCT has been reviewed by various authors e.g. [11] and most recently by Fercher et al. [12]. A short history and state of the art can be found in [13]. For more details, the reader may consult the “Handbook of OCT” [14]. The current status of OCT as an advanced imaging tool in clinical medicine and developmental biology has been the object of a recent review [15].

In subsection 1.2.1 we will focus on the key parameters of OCT systems, while the rest of the section will be dedicated to a brief review of three OCT topics of direct relevance to this thesis, namely wide-field OCT, speckles, and models.

1.2.1 Imaging performance

The key parameters in OCT systems are resolution, sensitivity, and acquisition speed. An important feature is the independence between axial and lateral resolution. The latter is determined by the numerical aperture of the imaging optics, whereas the former is given by the source spectrum. According to the Wiener-Khinchine theorem, the source bandwidth and the coherence time are a Fourier transform pair. Thus, the broader the spectrum, the higher the axial resolution. In addition, the need for high sensitivity implies a bright source as sensitivity is proportional to the source power and inversely proportional to imaging speed [16]. Since the image acquisition speed must be maximized so as to be insensitive to patient’s movements or to “freeze” fast varying phenomena, the need for a powerful source is even more imperative. A sensitivity typically above 90 dB is required for imaging biological samples [14]. These two opposite constraints (broad spectrum and high power) led, over the past decades, to the intensive development of ultra-short pulsed laser sources. Present day optimal OCT sources consist mainly of powerful mode-locked Ti:Sapphire pulsed lasers which deliver a few hundred mW with a spectral bandwidth in the order of 300 nm providing submicrometer axial resolutions [17,18]. To date, the highest axial resolution reported is 0.75 μm (FWHM in air) [19]. Supercontinuum sources leading to even broader spectra are currently investigated [18,20]. Owing to their naturally broad spectrum, thermal light sources can provide a very high resolution but requires a wide-field imaging system (see 1.2.2).

A high image acquisition speed also requires fast scanning. Intensive development of fast scanning mechanisms and methods took place during last decade [21]. Presently available fastest systems rely on phase delay lines [22]. Such state of the art systems can achieve video-rate image acquisition with SNRs above 100 dB when ultra-short pulsed lasers are used [18,23]. Another way to obtain high

acquisition speed is the parallelization of the method leading to wide-field OCT, as explained in the next subsection.

Nowadays, research is strongly oriented towards the development of the so called Fourier or spectral domain OCT where the axial depth scan is performed by a spectroscopic signal analysis instead of mechanical scanning [24]. This method, which complies with all system requirements, might be the best choice for future OCT systems.

1.2.2 Wide-field OCT

In wide-field OCT, the lateral scanning motions and acquisition with a single detector are replaced by the imaging of the whole sample onto a detector array. Parallel acquisition allows simplification of the system as well as high acquisition speed (potentially much higher than in point scanning OCT), a requirement that must be fulfilled to be insensitive to patient's movements or to "freeze" fast varying phenomena [25]. Moreover, wide-field OCT offers the possibility to use thermal light sources despite their low brightness by taking advantage of the much slower axial scan than in point scanning OCT [26,27]. Owing to a naturally broad spectrum, a thermal light source offers a micrometer resolution with the additional advantage of low cost and simplicity. However, the brightness of thermal light sources remains insufficient requiring a trade-off between sensitivity and acquisition speed [28].

In wide-field OCT, image acquisition relies on a detector array. Common charge-coupled devices (CCDs) can be used, however with some restrictions due to their relatively low dynamic range and low frame rate. Indeed, the latter does not allow fast enough sampling of the interferometric signal for heterodyne detection. This led to the implementation and development of ingenious alternative methods such as mechanical [26,29] or polarization [30] phase stepping, temporally multiplexed lock-in detection with stroboscopic illumination [31,32], or frequency synchronous detection using liquid crystal shutters [33].

However, the low dynamic range inherent to CCDs limits applications to relatively weakly scattering samples. Indeed, the much higher amount of light collected from the reference arm than from the sample arm for a strongly scattering sample, can easily saturate the CCD wells. Attenuation of the power from the reference arm results in a lower sensitivity. To tackle this problem, while also providing a high frame rate, CMOS based customized detectors were developed in our institute. Such detectors offer the additional functionality of OCT integrated signal processing for each pixel, thus allowing suppression of the strong reference signal by bandpass filtering. The potential of a so-called "smart pixel detector array" prototype has been demonstrated for reflecting surfaces or scattering samples [34,35]. Sensitivity, readout speed, and fill factor need to be improved.

Wide-field OCT might suffer from a more fundamental limitation. Indeed, with wide-field illumination and parallel detection, the amount of multiply scattered light collected by each detector is considerably higher than that collected with focused illumination and single channel detection like in point scanning OCT. Depending on the nature of the illumination, multiply scattered light can result in a strong cross-talk generated noise between parallel detection channels. Presently, little is known on the importance of cross-talk effects in wide-field OCT with spatially coherent illumination [29,35], i.e. on the rejection capabilities of multiply scattered light when relying on temporal coherence gating alone. This important issue is addressed in chapter III and IV of this thesis.

1.2.3 Speckles

Like in any coherent imaging method, the speckle phenomenon plays a major role in optical coherence tomography (OCT) [36]. With biological specimen, speckles reduce contrast and make boundaries between constitutive tissues more difficult to resolve, especially in a highly scattering tissue such as skin.

To date, most research on speckles in OCT was carried on by the group of Schmitt et al [37]. Investigations were focused mainly on the origin and formation of speckles in tissues as well as on their influence on OCT images. Considerable attention was also devoted to methods for speckle reduction. The latter require the generation of mutually uncorrelated speckle patterns by either of the "physical means" classified by Goodman as "polarization, frequency, space and time diversity" [38].

Practical implementations of these means for obtaining diversity, which are widely applied to ultrasound and astronomy, have been adapted to OCT [37,39-42]. In addition, post-processing methods can also help reducing speckle contrast to a certain extent [43].

Alternatively, like in metrology with coherent illumination of a rough surface, speckles can be considered as either a source of noise or a carrier of information. Speckle pattern properties, such as contrast or decorrelation, directly depend on the sample microscopic structure. Preliminary analyses of the speckle contrast and texture show that it is possible to differentiate between different types of tissues [44,45].

In the framework of this thesis, we address some issues regarding the amplitude distribution of speckles in an OCT signal.

1.2.4 Models for OCT

The primary motivation of modeling OCT is to better evaluate the system limitations and to improve the imaging capabilities by providing some guidance on instrument design and data processing algorithms. The most simple theoretical model, the “single backscattering model”, neglects multiple scattering and can be applied successfully only to moderate probing depths or weakly scattering samples [46]. However, as seen in section 1.1, multiple scattering is a major limiting factor to the OCT method, and should thus be accounted for in a comprehensive model. The way coherence properties of signals are affected by multiple scattering is not fully understood and still remains an area of intense research [47,48].

A comprehensive model of OCT requires modeling both the light propagation in random media and the interference process, which depends on coherence properties of the sample field. Light propagation in random media, including temporal aspects, can be described quite successfully by the time-resolved diffusion theory as reported by Ishimaru [49] or Patterson [50]. However, this theory is based on the diffusion approximation, which becomes valid only after a few scattering events [51], yielding delays of a few picoseconds [50,52]. Such delays, which largely exceed typical source coherence times in OCT, correspond to considerable pathlengths, i.e. in the order of one millimeter. Therefore, models based on the diffusion approximation fail to properly describe multiply scattered light distribution in the range of interest met in OCT where pathlengths are one to three orders of magnitude lower. The statistical model introduced by Gandjbakhche also requires many scattering events to become applicable [53].

A numerical calculation performed by a Monte Carlo simulation can provide the spatio-temporal distribution of light within the entire range of interest [50,52]. Several existing models of OCT are based on Monte Carlo simulation e.g. [54,55]. However, the latter cannot, in principle, account for the coherence properties of multiply scattered light, whose knowledge is indispensable in the context of coherent detection techniques. Models based on the linear systems theory suffer from the same limitation [56].

It is generally believed that multiple scattering causes a loss of spatial coherence of the sample field causing reduction of the interference contrast. A model of OCT, first introduced by Schmitt and Knuettel [57], and further improved by Thrane et al. who included the “shower curtain effect” [58], accounts for spatial coherence properties of the sample field. This model is based on the so-called extended Huygens-Fresnel principle [59], an analytical model based on the radiative transport theory, and the use of mutual coherence functions. To date, it is the most comprehensive model of OCT.

Although it is generally believed that a relevant model should account for a reduction of spatial coherence due to multiple scattering, it remains an open issue which is addressed in this thesis. In section 3.1, a new model resting on different assumptions is developed and the applicability of models based on the extended Huygens-Fresnel principle is discussed.

1.3 Goals and structure of the thesis

This thesis aims to explore the performance and limitations of wide-field OCT. We address the issue of coherent noise generated by optical cross-talk, and develop a new model which offers a general account of multiple scattering in OCT. Investigation of the influence of the source spatial coherence properties is at the heart of this work. As appearing in the thesis structure given below, several related problems and solutions are investigated as well. The 3 main chapters of this thesis are:

Chapter II which provides notions related to light coherence and to speckles indispensable for the understanding of this thesis. Particular emphasis is put on the relation between the degree of spatial coherence and interference. This important relation is demonstrated for a simple case by an original and hopefully didactic approach.

In section 2.2 relevant basic notions of speckle formation and statistics are introduced. Presently, two different theoretical results for the amplitude distribution of speckles in an OCT signal, each of them based on a different mathematical formulation, exist in the literature. We show that a modification of an initial assumption in one of the formulation leads to equivalent results. This demonstration has made the object of a publication.

The material of this chapter is however not an essential piece of the thesis and can be skipped at first reading.

Chapter III is mainly devoted to wide-field OCT with coherent illumination. It is divided into three main sections each of them corresponding to a publication of direct relevance to this topic.

Section 3.1 provides the experimental proof of feasibility of wide-field OCT in scattering samples using a smart-pixel detector array. Demonstration is made with a resolution target covered by an intralipid solution with different scattering coefficients as well as onion cells. Analyses of the results raise fundamental questions, which are addressed in the rest of the chapter.

Section 3.2 begins with a careful investigation of the coherence properties of the sample field. Based on our conclusions we present a new model of OCT taking into account multiple scattering. To calculate the mean of an OCT signal, we exploit classical results of statistical optics and a Monte Carlo simulation. We discuss the applicability of other widely used models of OCT, which rest on different assumptions.

In section 3.3, we present a comprehensive study of optical cross-talk in wide-field OCT realized with spatially coherent illumination. We investigate the dependence of cross-talk on important system design parameters, as well as on some relevant sample properties. Theoretical results obtained with our model are compared to experimental data for a wide range of parameters.

Chapter IV consists of five sections dedicated to wide-field OCT with incoherent illumination. In sections 4.1 we explain how spatially incoherent illumination can lead to efficient cross-talk suppression in wide-field OCT. We introduce the concept of “spatial coherence gating”. Section 4.2, which is based on a publication, provides the experimental demonstration of cross-talk suppression with a thermal light source in wide-field OCT. Images of a resolution target covered by a microbeads’ solution, as well as of an ex-vivo human tooth, obtained with spatially coherent and incoherent illumination are directly compared. In section 4.3 and 4.4, we investigate the potential of thermal light sources in terms of axial resolution and power per mode, respectively. Emphasis is put on the dependence of the signal to noise ratio with the source temperature and the OCT therapeutic window. Section 4.5 provides a preliminary study showing the possibility of using a pseudo-thermal light source in wide-field OCT. We derive basic design rules and discuss some inherent limitations.

We will end our dissertation with a general conclusion and discussion on perspectives for further developments.

References

- [1] M.R. Hee, J.A. Izatt, J.M. Jacobson, J.G. Fujimoto, and E.A. Swanson, "Femtosecond transillumination optical coherence tomography," *Opt. Lett.* **18**, 950-952 (1993).
- [2] M. Kempe, W. Rudolph, and E. Welsh, "Comparative study of confocal and heterodyne microscopy for imaging through scattering media," *J. Opt. Soc. Am. A* **13**, 46-52 (1996).
- [3] W. Rudolph and M. Kempe, "Topical review: Trends in optical biomedical imaging," *J. Mod. Opt.* **44**, 1617-1642 (1997).
- [4] J.B. Pawley, "Handbook of biological confocal microscopy," New York Plenum, (1990).
- [5] J.A. Izatt, M.R. Hee, G.M. Owen, E.A. Swanson, J.G. Fujimoto, "Optical coherence microscopy in scattering media," *Opt. Lett.* **19**, 590-592 (1994).
- [6] M. Kempe, A.Z. Genack, W. Rudolph, and P. Dorn, "Ballistic and diffuse light detection in confocal and heterodyne imaging systems," *J. Opt. Soc. Am. A* **14**, 216-223 (1997).
- [7] M.J. Yadlowsky, J.M. Schmitt, R.F. Bonner, "Multiple scattering in optical coherence microscopy," *Appl. Opt.* **34**, 5699-5707 (1995).
- [8] A.F. Fercher, C.K. Hitzenberger, W. Drexler, G. Kamp, and H. Sattmann, "In vivo optical coherence tomography," *Am. J. Ophth.* **116**, 113-114 (1993).
- [9] J. Welzel, "Optical coherence tomography in dermatology: a review," *Skin Research and Technol.* **7**, 1-9 (2001).
- [10] B.T. Amaechi, A.G. Podoleanu, G.N. Kornarov, J.A. Rogers, S.M. Higham, and D.A. Jacksow, "Application of optical coherence tomography for imaging and assessment of early dental caries lesions," *Las. Phys.* **13**, 703-710 (2003).
- [11] J.M. Schmitt, "Optical Coherence Tomography (OCT): A Review," *IEEE J. Selec. Topics in Quant. electron.* **5**, 1205-1215 (1999).
- [12] A.F. Fercher, W. Drexler, C.K. Hitzenberger, and T. Lasser, "Optical coherence tomography - principles and applications," *Rep. Prog. Phys.* **66**, 239-303 (2003).
- [13] M. Laubscher, "Innovative experimental concepts for optical coherence tomography," PhD thesis 2954, Swiss Federal Institute of Technology of Lausanne, 2-13 (2004).
- [14] B.E. Bouma and G.J. Tearney, editors, "Handbook of Optical Coherence Tomography," Marcel Dekker, Inc., (2003).
- [15] C. Mason, J.F. Markusen, M.A. Markusen, M.A. Town, P. Dunhill and R.K. Wang, "The potential of optical coherence tomography in the engineering of living tissues," *Phys. Med. Biol.* **49**, 1097-1115 (2004).
- [16] E.A. Swanson, D. Huang, M.R. Hee, J.G. Fujimoto, C.P. Lin, C.A. Puliafito, "High-speed optical coherence domain reflectometry," *Opt. Lett.* **17**, 151-153 (1992).
- [17] W. Drexler, U. Morgner, F.X. Kärtner, C. Pitris, S.A. Boppart, X.D. Li, E.P. Ippen, and J.G. Fujimoto, "In vivo ultrahigh-resolution optical coherence tomography," *Opt. Lett.* **24**, 1221-1223 (1999).
- [18] A. Unterhuber, B. Povazay, K. Bizheva, et al., and W. Drexler, "Advances in broad bandwidth light sources for ultrahigh resolution optical coherence tomography," *Phys. Med. Biol.* **49**, 1235-1246 (2004).
- [19] B. Povazay, K. Bizheva, A. Unterhuber, B. Hermann, H. Sattmann, A.F. Fercher, W. Drexler et al., "Submicrometer axial resolution optical coherence tomography," *Opt. Lett.* **27**, 1800-1803 (2002).

- [20] Y. M. Wang, Y. H. Zhao, J. S. Nelson, Z. P. Chen, and R. S. Windeler, "Ultra-high-resolution optical coherence tomography by broadband continuum generation from a photonic crystal fiber," *Opt. Lett.* **28**, 182-184 (2003).
- [21] J. Szydlo, N. Delachenal, R. Gianotti, R. Walti, H. Bleuler, and R.P. Salathé, "Air-turbine driven optical low-coherence reflectometry at 28.6-kHz scan repetition rate," *Opt. Com.* (1-3):1-4, 154 (1998).
- [22] G.J. Tearney, B.E. Bouma, and J.G. Fujimoto. "High-speed phase- and group-delay scanning with a grating-based phase control delay line," *Opt. Lett.* **22**, 1811-1813 (1997).
- [23] A.M. Rollins, J. Izatt, M.D. Kulkarni, S. Yasdanfar, R. Ung, "In vivo video rate optical coherence tomography," *Opt. Exp.* **3**, 219-229 (1998).
- [24] R.A Leitgeb, W. Drexler, A. Unterhuber, B. Hermann, T. Bajraszewski, T. Le, A. Stingl, and A.F. Fercher, "Ultra-high resolution Fourier domain optical coherence tomography," *Opt. Exp.* **12**, 2156-2165 (2004).
- [25] M. Laubscher, M. Ducros, B. Karamata, T. Lasser, and R.P. Salathé "Video-rate three-dimensional optical coherence tomography," *Opt. Exp.* **9**, 429-435 (2002).
- [26] L. Vabre, A. Dubois, and A. C. Boccara, "Thermal full-field optical coherence tomography," *Opt. Lett.* **27**, 530-532 (2002).
- [27] B. Laude, A de Martino, B. Drevillon, L. Benattar, and L. Schwartz, "Full-field optical coherence tomography with thermal light," *Appl. Opt.* **41**, 6637-6645 (2002).
- [28] A.F. Fercher, C.K. Hitzenberger, M. Sticker, E. Moreno-Barriuso, R. Leitgeb, W. Drexler and H. Sattmann, "A thermal light source technique for optical coherence tomography," *Opt. Com.* **185**, 57-64 (2000).
- [29] E. Abraham, E. Bordenave, N. Tsurumachi, G. Jonusauskas, J. Oberlé, and C. Ruillère, "Real-time two-dimensional imaging in scattering media by use of a femtosecond Cr⁴⁺: forsterite laser," *Opt. Lett.* **25**, 929-931 (2000).
- [30] C. Dunsby, Y. Gu, and P.M.W. French, "Single-shot phase stepped wide-field coherence gated imaging," *Opt. Exp.* **11**, 105-115 (2003).
- [31] E. Beaufrepaire, A.C. Boccara, M. Lebec, L. Blanchot, and H. Saint-Jalmes, "Full-field optical coherence microscopy," *Opt. Lett.* **23**, 244-246 (1998).
- [32] A. Dubois, L. Vabre, A.C. Boccara, E. Beaufrepaire, "High resolution full-field optical coherence tomography with a Linnik microscope", *Appl. Opt.* **41**, 805-812 (2002).
- [33] M. Akiba, K.P. Chan, and N. Tanno, "Full-field optical coherence tomography by two-dimensional heterodyne detection with pair of CCD cameras," *Opt. Lett.* **28**, 816-818 (2003).
- [34] S. Bourquin, P. Seitz and R.P. Salathé, "Optical coherence tomography based on two-dimensional smart detector array," *Opt. Lett.* **26**, 512-514 (2001).
- [35] M.G. Ducros, M. Laubscher, B. Karamata, S. Bourquin, T. Lasser, and R.P. Salathé, "Parallel optical coherence tomography in scattering samples using a two-dimensional smart-pixel detector array," *Opt. Com.* **202**, 29-35 (2002).
- [36] J.W. Goodman, "Statistical properties of laser speckle patterns," in *Laser speckle and related phenomena*, Topics in applied physics: Vol. 9, ed. J.C. Dainty, (1975).
- [37] J.M. Schmitt, S.H. Xiang, K.M. Yung, "Speckle in Optical Coherence Tomography", *J. Biomed. Opt.* **4**, 95-105 (1999).
- [38] J.W. Goodman, "Some fundamental properties of speckle," *J. Opt. Soc. Am.* **66**, 1145-1150 (1976).
- [39] J.M. Schmitt, "Array detection for speckle reduction in optical coherence tomography," *Phys. Med. Biol.* **42**, 2307-2320 (1997).

- [40] M. Bashkansky and J. Reintjes, "Statistics and reduction of speckle in optical coherence tomography," *Opt. Let.* **25**, 545-547 (2000).
- [41] N. Iftimia, B.E. Bouma, and G.J. Tearney, "Speckle reduction in optical coherence tomography by path length encoded angular compounding," *J Biomed Opt* **8**, 260-263 (2003).
- [42] M. Pircher, E. Goetzinger, R. Leitgeb, A.F. Fercher, C.K. Hitzenberger, "Speckle reduction in optical coherence tomography by frequency compounding," *J. Biomed. Opt* **8**, 565-569 (2003).
- [43] K.M. Jung, S.L. Lee, and J.M. Schmitt, "Phase-domain processing of optical coherence tomography images," *J. Biomed. Opt.* , 125-136 (1999).
- [44] K.W. Gossage, T.S. Tkaczyk, J.J. Rodriguez, et al., "Texture analysis of optical coherence tomography images: feasibility for tissue classification," *J Biomed Opt* **8**, 570-575 (2003).
- [45] D.A. Zimnyakov, V.V. Tuchin, A.A. Mishin, "Spatial speckle correlometry in applications to tissue structure monitoring," *Appl. Opt* **36**, 5594-5607 (1997).
- [46] J.M. Schmitt, A. Knuettel, and R.F. Bonner, "Measurement of optical properties of biological samples in low-coherence reflectometry," *Appl. Opt.* **32**, 6032-6042 (1994).
- [47] J. Sajeev, P. Gendi, and Y. Yumin, "Optical coherence propagation and imaging in a multiple scattering medium", *J Biomed Opt* **1**, 180-191 (1996).
- [48] C. Yang, K. An, L.T. Perleman, R.R. Dasari, and M.S. Feld, "Spatial coherence in forward-scattered light in a turbid medium", *J. Opt. Soc. Am. A* **16**, 866-871 (1999).
- [49] A. Ishimaru, Y. Kuga, R. Cheung, K. Shimizu, "Diffusion of a pulse in densely distributed scatterers," *J. Opt. Soc. Am. A* **68**, 1045-1050 (1978).
- [50] M.S. Patterson, B. Chance and B. C. Wilson, "Time resolved reflectance and transmittance for the non-invasive measurement of tissue optical properties," *Appl. Opt.* **28**, 2331-2336 (1989).
- [51] A. Ishimaru, Y. Kuga, R. Cheung, K. Shimizu, "Scattering and diffusion of a beam wave in randomly distributed scatterers," *J. Opt. Soc. Am. A* **73**, 131-136 (1983).
- [52] S.L. Jacques, "Time resolved propagation of ultrashort laser pulses within turbid tissues," *Appl. Opt.* **28**, 2223-2229 (1989).
- [53] A. H. Gandjbakhche, R. Nossal, R. F. Bonner, "Scaling relationships for theories of anisotropic random walks applied to tissue optics," *Appl. Opt.* **32**, 504-516 (1993).
- [54] D.J. Smithies, T. Lindmo, Z. Chen, J.S. Nelson, and T.E. Milner, "Signal attenuation and localization in optical coherence tomography studied by Monte Carlo simulation," *Phys. Med. Biol.* **43**, 3025-3044 (1998).
- [55] G. Yao, L.V. Wang, "Monte Carlo simulation of an optical coherence tomography signal in homogeneous turbid media," *Phys. Med. Biol.* **44**, 2307-2320 (1999).
- [56] Y. Pan, R. Birngruber, J. Rosperich, R. Engelhardt, "Low-coherence optical tomography in turbid tissue: theoretical analysis," *Appl. Opt.* **34**, 6564-6574 (1995).
- [57] J.M. Schmitt and A. Knuettel, "Model of optical coherence tomography of heterogeneous tissue," *J. Opt. Soc. Am. A* **14**, 1231-1242 (1997).
- [58] L. Thrane, H.T. Yura, and P.E. Andersen, "Analysis of optical coherence tomography systems based on the extended Huygens-Fresnel principle," *J. Opt. Soc. Am. A* **17**, 484-490 (2000).
- [59] H.T. Yura, "Signal-to-noise ratio of heterodyne lidar signal systems in the presence of atmospheric turbulence," *Opt. Acta* **26**, 627-644 (1979).

CHAPTER II

Light coherence and speckles

The notion of light coherence and speckles play a major role in this thesis. Such non-deterministic phenomena belong to the field of statistical optics whose basic notions are provided in this section.

In section 2.1 we introduce concepts and definitions frequently used in this thesis, in particular the concept of coherence volume and mode. Emphasis is put on the interdependence of the degree of spatial coherence and interference visibility. This important relation is demonstrated for a simple case by an original and hopefully didactic approach.

In section 2.2 relevant basic notions of speckle formation and statistics are introduced. Presently, two different theoretical results for the amplitude distribution of speckles in an OCT signal, each of them based on a different mathematical formulation, exist in the literature. We show that a modification of an initial assumption in one of the formulation leads to equivalent results. This demonstration has made the object of a publication.

The material of this chapter is however not an essential piece of the thesis and can be skipped at first reading.

2.1 Light coherence

2.1.1 Degree of coherence

In its widest sense, the degree of coherence allows to quantify the “degree of randomness” of light fluctuations. It characterizes the phase correlation between two optical wave disturbances in space and time. For a meaningful definition of the “degree of coherence”, a statistical averaging over an ensemble of many realizations of random optical wave-functions must take place. When the random process is ergodic, i.e. the same statistics prevails at any time, statistical averaging can be obtained by time averaging. The minimum time \mathbf{t} necessary for obtaining sufficient statistical averaging must be much larger than the fluctuation time scale T_f of the random field. Thus, for $\mathbf{t} \gg T_f$, the statistical averaging of a random function $g(u)$ corresponds to:

$$\langle g(u) \rangle = \frac{1}{\mathbf{t}} \int_0^{\mathbf{t}} g[u(t)] dt \approx \lim_{T \rightarrow \infty} \frac{1}{T} \int_{-T/2}^{T/2} g[u(t)] dt, \quad (1)$$

where the symbol $\langle \rangle$ denotes an ensemble average over many realizations of the random function. The degree of coherence can be expressed in a formal mathematical way leading to useful results and definitions [1]. The degree of correlation of a random field disturbance measured in two points r_1 and r_2 can be advantageously described by means of the cross-correlation function $G(r_1, r_2, \mathbf{t})$ of $U(r_1, t)$ and $U(r_2, t)$

$$G(r_1, r_2, \mathbf{t}) = \langle U(r_1, t) U^*(r_2, t + \mathbf{t}) \rangle, \quad (2)$$

where \mathbf{t} is the time delay and $*$ the complex conjugate. This function is known as the *mutual coherence function* and its normalized form is called the *complex degree of coherence* [2]

$$g(r_1, r_2, \mathbf{t}) = \frac{G(r_1, r_2, \mathbf{t})}{\sqrt{I(r_1)I(r_2)}} \quad (3)$$

The modulus of the complex degree of coherence is bounded between zero and unity and decreases with the time delay \mathbf{t} and the distance separating r_1 and r_2 .

Remarkably, the modulus of the complex degree of coherence, expressed with the cross-correlation coefficient of the random variables $U(r_1, t)$ and $U(r_2, t)$, also corresponds to the fringe visibility obtained by the Young’s experiment with pinholes placed in r_1 and r_2 [2]

$$V = |g(r_1, r_2, \mathbf{t})| \quad (4)$$

The visibility is a physical manifestation of the degree of light coherence that can be directly observed.

Although relying on the same physical phenomenon, coherence effects are usually divided into two classes namely the temporal and the spatial coherence.

Temporal coherence

The degree of temporal coherence is a measure of correlation between one single point ($r_1 = r_2 = r$) at two different instants. It can be obtained by simultaneously measuring the degree of spatial coherence at two points along the same light ray. The corresponding time difference is equal to the speed of light in the medium divided by the distance separating r_1 and r_2 . Practically the degree of temporal

coherence can be measured with an amplitude splitting interferometer. The *temporal coherence function* is defined as

$$G(\mathbf{t}) = \langle U(\mathbf{t})^* U(\mathbf{t} + \mathbf{t}) \rangle, \quad (5)$$

and, in turn, its normalized form, the *complex degree of temporal coherence*, as

$$g(\mathbf{t}) = \frac{G(\mathbf{t})}{I} \quad (6)$$

The Wiener-Khinchine theorem relates the finite spectral bandwidth of the source to the complex degree of temporal coherence $g(\mathbf{t})$.

A broadband source can be characterized by its power spectral density $S(\mathbf{n})$. The Wiener-Khinchine theorem states that $S(\mathbf{n})$ and $G(\mathbf{t})$ form a Fourier transform pair:

$$S(\mathbf{n}) = \int_{-\infty}^{\infty} G(\mathbf{t}) \cdot e^{-j2\pi\mathbf{n}\mathbf{t}} d\mathbf{t} \quad (7)$$

Normalizing the inverse Fourier transform of this relationship yields:

$$g(\mathbf{t}) = \frac{1}{I_0} \int_{-\infty}^{\infty} S(\mathbf{t}) \cdot e^{j2\pi\mathbf{n}\mathbf{t}} d\mathbf{t}, \quad (8)$$

where I_0 is the source average intensity.

Spatial coherence

The degree of spatial coherence is a measure of the field correlation between two points in space when the time delay $\mathbf{t} = 0$. This means that either the wave is monochromatic or that the measurement takes place within the coherence length l_c (see 2.1.3). Thus, the *mutual intensity* is defined as

$$G(r_1, r_2) = \langle U(r_1, t)^* U(r_2, t) \rangle, \quad (9)$$

and, in turn, its normalized form, called the *complex coherence factor*, as

$$g(r_1, r_2) = \frac{G(r_1, r_2)}{\sqrt{I(r_1)I(r_2)}} \quad (10)$$

Analogous to the Wiener-Khinchine theorem relating the source finite spectral bandwidth to the complex degree of temporal coherence $g(\mathbf{t})$, the Van Cittert-Zernike theorem [2] relates the incoherent source spatial extent, which determines a spatial frequency bandwidth, to the degree of spatial coherence, i.e. to the mutual intensity. The Van Cittert-Zernike theorem states that $I(r)$ and $G(r_1, r_2)$ form a double integral Fourier transform pair. The normalized form of this theorem is:

$$g(r_1, r_2) = \frac{e^{-jz}}{I_0} \iint_{-\infty}^{\infty} I(\mathbf{x}, \mathbf{h}) \cdot \exp \left[j \frac{2\mathbf{p}}{Iz} (\Delta x \cdot \mathbf{x} + \Delta y \cdot \mathbf{h}) \right] d\mathbf{x} d\mathbf{h}, \quad (11)$$

where:

- (\mathbf{x}, \mathbf{h}) corresponds to the coordinates of a point P in the source plan
- $\Delta x = |r_1(x) - r_2(x)|$
- $\Delta y = |r_1(y) - r_2(y)|$

- $e^{i\phi}$ is a phase factor which can be omitted under certain conditions [2]
- $I(\mathbf{x}, \mathbf{h})$ is the source intensity distribution whose value is zero when (\mathbf{x}, \mathbf{h}) lies outside the source finite region Σ
- I_0 is the total intensity obtained after integration over the source spatial extent

These parameters are illustrated in Fig. 1.

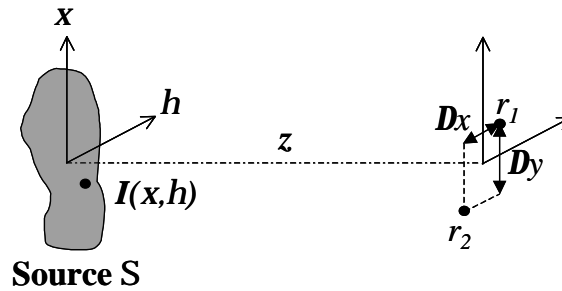


Fig. 1 Geometry for the derivation of the Van Cittert-Zernike theorem. The parameters are explained above.

Like all functions describing the degree of coherence, the normalized mutual intensity can be interpreted in terms of fringe visibility in the Young's experiment.

$$V = |g(r_1, r_2)| \tag{12}$$

This leads to a very intuitive and straightforward interpretation of the degree of coherence and its dependence on physical parameters involved, as shown in the next section.

2.1.2 Coherence and interference

To fully appreciate the equivalence between the degree of spatial coherence and the fringe visibility we will calculate the loss of contrast for a simple case and show that the Van Cittert-Zernike theorem yields the same result.

Let us first consider a deterministic optical wave propagating in space sampled in two points arbitrary located at positions r_1 and r_2 separated by a distance Dr (Fig. 2). According to the Huygens principle, spherical waves are scattered from the two sampling points. The interference between these two spherical waves generates a sinusoidal intensity pattern at a distance D large compared to Dr (Fresnel approximation).

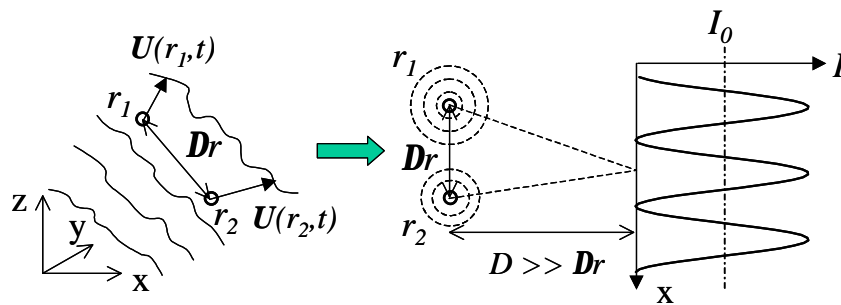


Fig. 2 Interference pattern produced by two arbitrarily located pinholes sampling a deterministic optical wave propagating in space.

Taking into account the physical dimensions involved, the intensity fringe pattern can be expressed as follows:

$$I(x) = 2I_0 \left[1 + V \cos \left(\frac{4p\Delta r}{DI} x + \mathbf{j} \right) \right], \quad (13)$$

where λ is the wavelength, \mathbf{j} a constant phase factor and V is the visibility or fringe contrast defined as (see Fig. 3)

$$V = \frac{I_{\max} - I_{\min}}{I_{\max} + I_{\min}} \quad (14)$$

The position along the X-axis of a peak of the intensity pattern relative to either r_1 or r_2 is determined by the phase \mathbf{j} , which is equal to the phase difference between the fields $U(r_1)$ and $U(r_2)$. For a stationary wavefront, i.e. for a constant phase relationship between r_1 and r_2 , the maximum fringe visibility, i.e. $V=1$, is reached (Fig. 2). Each different deterministic wavefront would produce a sinusoidal intensity fringe pattern with maximum visibility shifted by a different phase argument \mathbf{j} .

A random wavefront induces a random phase difference between r_1 and r_2 . This yields a multitude of randomly laterally shifted sinusoidal fringe patterns. Assuming a fast phase fluctuation relative to measurement time (condition required for statistical averaging), a multitude of patterns are averaged. The sum of many sines of equal period but different phase arguments \mathbf{j} yields a single sine with identical period but lower visibility, as illustrated in Fig. 3. For \mathbf{j} values randomly distributed between zero and 2π the visibility is null, i.e. the degree of coherence is null.

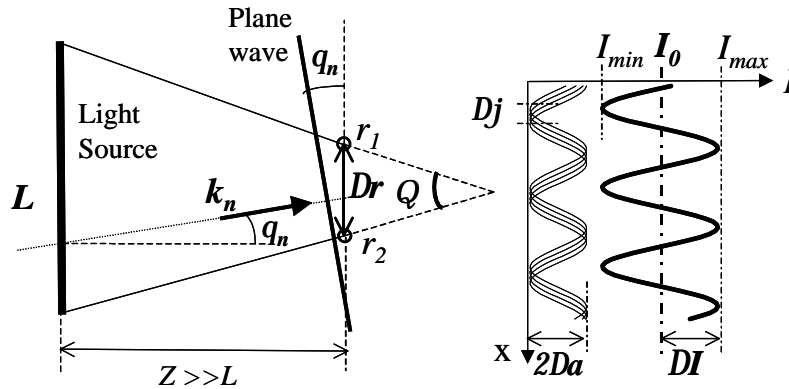


Fig. 3 Schematic representation of the relationship between the degree of spatial coherence, caused by a spatially incoherent (extended) light source viewed under an angle Q , and the visibility measured with 2 pinholes distant by Dr . Details are in text.

Let us now calculate, by using purely geometrical arguments, the visibility for an intermediate case corresponding to a degree of coherence ranging between zero and one. Consider an extended source consisting of a uniformly illuminated slit of length L . When $Z \gg L$ (a hypothesis made in the Van Cittert-Zernike theorem as well), the slit source, viewed from the pinhole pair $r_{1/2}$ of Young's experiment, appears under an angle $Q = L/Z$. The extended source produces a collection of n independent plane waves with a wave-vector k_n forming an angle q_n with the line defined by r_1 and r_2 (Fig. 3). The maximal angular range of incidence angles q_n is determined by Q , which, in turn, determines the range $D\mathbf{j}$ corresponding to the maximum phase shift of the fringe pattern. These geometrical relationships yield:

$$\Delta \mathbf{j} = \frac{2\mathbf{p}\Theta\Delta r}{l}, \quad (15)$$

where $\mathbf{D}r$ is the distance between r_1 and r_2 .

Like in the van Cittert-Zernike theorem, we assume a coherence length of the radiation much larger than Z and a spatially totally incoherent field at the slit. The visibility of the fringe intensity pattern produced at a distance Z from the slit of length L (in the slit plane) corresponds to the sum of n sinusoids of equal period and equal amplitude $\mathbf{D}a$ shifted by a phase factor \mathbf{j}_n . This sum, corresponding to an integration over the whole range $\mathbf{D}\mathbf{j}$, is equal to a constant intensity background I_0 plus a sinusoid of amplitude $\mathbf{D}I$ with identical period (Fig. 3).

$$\int_0^{\Delta \mathbf{j}} 1 + \Delta a \cos(x - \mathbf{j}) d\mathbf{j} = I_0 + \Delta I \cos(x - \mathbf{y}) \quad (16)$$

After integration and application of trigonometric relationships, Eq. (16) yields:

$$\Delta \mathbf{j} + \sin x (\cos \Delta x - 1) - \cos x \sin \Delta \mathbf{j} = I_0 + \Delta I (\cos x \cos \mathbf{y} + \sin x \sin \mathbf{y}), \quad (17)$$

leading to the following relationships:

$$\begin{cases} \Delta \mathbf{j} = I_0 \\ \cos \Delta \mathbf{j} - 1 = \Delta I \sin \mathbf{y} \\ -\sin \Delta \mathbf{j} = \Delta I \cos \mathbf{y} \end{cases}$$

Combining these 3 equations and using the equivalence $\sin^2 \mathbf{y} + \cos^2 \mathbf{y} = 1$ yields:

$$\Delta I = \Delta a \sqrt{2 - 2 \cos(\Delta \mathbf{j})} \quad (18)$$

The visibility V corresponds to the ratio between $\mathbf{D}I$ and I_0

$$V = \frac{\Delta I}{I_0} = \frac{\sqrt{2 - 2 \cos(\Delta \mathbf{j})}}{\Delta \mathbf{j}} \quad (19)$$

Application of basic trigonometric rules and substitution of Eq. (15) reveal that

$$V = \left| \mathbf{p} \cdot \text{sinc} \left(\frac{\Delta \mathbf{j}}{2\mathbf{p}} \right) \right| = \left| \mathbf{p} \cdot \text{sinc} \left(\frac{\Theta \Delta r}{l} \right) \right| \quad (20)$$

Remarkably, this result is identical to the solution provided by the Van Cittert-Zernike theorem applied to this case. Indeed, the theorem states that the degree of spatial coherence $g(r_1, r_2)$ is the absolute value of the Fourier transform of the source intensity. The Fourier of a square function - provided here by a slit of uniform intensity - is indeed a *sinc* function, and with the geometrical parameters involved

$$g(r_1, r_2) = \mathbb{F}[I(x)] = \left| \mathbf{p} \cdot \text{sinc} \left(\frac{\Theta \Delta r}{l} \right) \right|, \quad (21)$$

where $I(x)$ is a function equal to one between $-L/2$ and $+L/2$ and to zero elsewhere. Thus, Eq. (20) and Eq. (21) reveal the equivalence between the degree of spatial coherence and the interference fringe visibility for the simple case investigated

$$V = |g(r_1, r_2)| \quad (22)$$

The calculation performed also demonstrates that the degree of coherence is nothing else but a function describing the loss of visibility caused by a random phase fluctuation in a bounded interval, which directly depends on geometrical parameters.

The Van Cittert-Zernike theorem describes the loss of visibility for the more general case of a source with an arbitrary shape and intensity. Taking into account a general shape, weighted by the intensity distribution, would allow the derivation of the Van Cittert-Zernike theorem.

2.1.3 Coherence volume

An intuitive insight into the coherence properties of light can be gained by introducing the notion of coherence volume. The latter corresponds to the volume in which both spatial and temporal coherence is high, i.e. in which Young's experiment would provide a high visibility of the fringes.

As the modulus of coherence functions $g(r_1, r_2, \mathbf{t})$ decreases with time delay and/or spatial variations, criteria defining a zone of high coherence are generally used.

For temporal coherence, the modulus of $g(\mathbf{t})$ decreases with time delay (\mathbf{t}). A *coherence time* t_c is commonly defined as the power equivalent width of the complex degree of temporal coherence [3]:

$$t_c = \int_{-\infty}^{\infty} |g(\mathbf{t})|^2 dt \quad (23)$$

The *coherence length* is defined as:

$$l_c = ct_c \quad (24)$$

where c is the speed of light.

The coherence length corresponds to the distance along which the degree of coherence is high, i.e. a high fringe visibility would be measured in a Michelson interferometer.

Note that there are several other definitions of coherence time, usually based on the source spectral shape. In the frame of OCT, the definition based on the full width of the function $S(\mathbf{n})$ at half of its maximum value (FWHM) is commonly used. For a Gaussian spectrum, often met in OCT, this yields the coherence length [4]

$$l_c = \frac{4 \ln 2}{p} \frac{I_0^2}{\Delta I} \quad (25)$$

For spatial coherence, the modulus of $g(r_1, r_2)$ decreases with distance $\mathbf{Dr} = |r_2 - r_1|$. Analogous to the definition of coherence time t_c , a *coherence area* A_c is defined as the power equivalent surface of the normalized mutual intensity [2]

$$A_c = \int \int_{-\infty}^{\infty} |g(\Delta x, \Delta y)|^2 d\Delta x \cdot d\Delta y \quad (26)$$

Using the normalized form of the Van Cittert-Zernike theorem and the Parseval's theorem of Fourier analysis one can show that the coherence area at a distance z can be expressed as

$$A_c = (I z)^2 \frac{\int \int_{-\infty}^{\infty} I^2(\mathbf{x}, \mathbf{h}) d\mathbf{x} d\mathbf{h}}{\left[\int \int_{-\infty}^{\infty} I^2(\mathbf{x}, \mathbf{h}) d\mathbf{x} d\mathbf{h} \right]^2} \quad (27)$$

For a uniformly bright incoherent source of arbitrary area A_S one can show that

$$A_c = \frac{(I z)^2}{A_S} \Rightarrow A_c = \frac{I^2}{\Omega_S}, \quad (28)$$

where Ω_S is the solid angle under which the source is viewed.

The coherence volume V_c is naturally defined as the product of the coherence length with the coherence area [5].

$$V_c = l_c \cdot A_c \quad (29)$$

A coherence volume, or a mode, corresponds to the smallest coherent entity of an optical system. Since modes are uncorrelated entities, an optical system containing N modes can be considered as a discrete system with N multiplexed information channels. The concept of modes is a powerful understanding and design tool that will be widely used throughout this thesis, in particular in Chapter IV. Note that the term mode is often used for the spatial coherence only (Eq. (28)). A coherence volume could be called a spatio-temporal mode.

2.2 Speckles

2.2.1 Background

When illuminated with laser light, a rough surface acquires a chaotic granular appearance known as “speckle” pattern [6], a term introduced in the 1960’s when the first cw HeNe laser was operated. The speckle phenomenon is not inherent to electromagnetic optical waves only, but can occur whenever coherent waves interact with a random medium such as a rough surface or a scattering sample, a situation encountered for instance in ultrasound imaging.

Speckles originate from a random interference process. When coherently illuminated, a scattering sample generates a multitude of phasors whose electric fields U_n add coherently, and, since phase differences between phasors are random, a spatially random electric field of amplitude $U_T(x,y,z)$ is produced. If the phase differences spread over an interval equal or higher than 2π , the interference can take any state between fully constructive (bright speckle) and fully destructive (dark speckle), creating a high contrast speckle pattern. In the case of reflected optical waves, dark speckles can occur provided that the illuminated surface is rough on the scale of the wavelength. A contrasted speckle pattern makes the object boundaries more difficult to resolve and is thus responsible for the characteristic loss of resolution in coherent imaging systems.

The distribution of the speckle intensity, which results from a purely statistical process, can be calculated analytically for ideal cases. Although during previous decades, equivalent results have been derived in specific contexts, Goodman was the first to calculate the probability function describing the statistical distribution of speckle field and intensity. The main steps and results of his calculation are summarized hereafter.

Let us assume that light incident on a scattering sample is perfectly monochromatic and perfectly polarized. As illustrated in Fig. 4, the coherent sum of a multitude of random elementary phasors $U_n = a_n \exp(-j\mathbf{j}_n)$, gives a single phasor $U_T = A \exp(-j\mathbf{y})$, at a position $P(x,y,z)$:

$$U_T = A \exp(-j\mathbf{y}) = \sum_n a_n \exp(-j\mathbf{j}_n), \quad (30)$$

where $A(x,y,z)$ is the complex amplitude of the field.

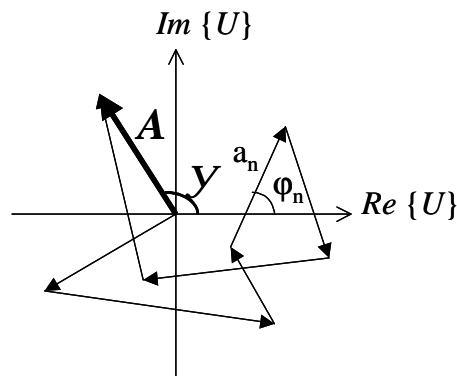


Fig. 4 Speckle formation as a sum of phasors with random amplitudes a_n and random phase \mathbf{j}_n shown in the real (Re) and imaginary (Im) dimension.

Results given below rest on the following important initial assumptions relative to statistical properties of elementary phasors [7]:

- (i) The phases \mathbf{j}_n are uniformly distributed over the interval $[0, 2\pi]$.
- (ii) The amplitude a_n and phase \mathbf{j}_n of the n th elementary phasor are statistically independent of each other, as well as of the amplitudes and phases of all elementary phasors.

From calculations involving statistical arguments, namely the central limit theorem, it follows that for a large number n of elementary phasors, the real and imaginary parts of the complex phasor U_T follow a Gaussian distribution if $U_n = a_n \exp(-j\mathbf{j}_n)$ are independent, zero mean, identically distributed Gaussian random variables.

Calculation of the probability density distribution for the phasor amplitude

$$A = \sqrt{(\operatorname{Re}\{U_T\})^2 + (\operatorname{Im}\{U_T\})^2}, \quad (31)$$

yields a Rayleigh density distribution

$$p(A) = \frac{A}{\mathbf{s}^2} \exp\left\{-\frac{A^2}{2\mathbf{s}^2}\right\}, \quad (32)$$

for $A > 0$, $p(A) = 0$ otherwise.

Calculation of the probability density distribution for the phasor intensity

$$I = (\operatorname{Re}\{U_T\})^2 + (\operatorname{Im}\{U_T\})^2, \quad (33)$$

yields a negative exponential density distribution

$$p(I) = \frac{1}{I_m} \exp\left\{-\frac{I}{I_m}\right\}, \quad (34)$$

for $I > 0$, $p(I) = 0$ otherwise, where I_m is the mean intensity.

This negative exponential probability density function, plotted in Fig. 5 ($N = 1$), reveals that the occurrence of a near zero intensity spot, i.e. a dark speckle, is more probable than that of a bright speckle. Moreover, a fundamental property of a negative exponential distribution is that its standard deviation (\mathbf{s}) equals its mean (I_m). The contrast C is usually defined as the ratio $C = \mathbf{s}/I_m$. Therefore, the contrast of a polarized monochromatic speckle pattern is characterized by a 100% contrast showing the considerable importance of the speckle phenomenon. Such a speckle pattern is referred to as a *fully developed speckle pattern*.

Lower contrast is obtained for a broadband illumination [8] or for a surface roughness inducing a phase excursion lower than 2π [9].

The speckle contrast can be reduced by averaging N uncorrelated speckle patterns. When these are mutually incoherent, the electric fields do not add and the summation is made on an irradiance basis. The average intensity is simply N times higher than the mean intensity I of each speckle pattern. However, as known from a fundamental result of probability theory, the sum of N identically distributed, real-valued, uncorrelated random variables has a standard deviation \mathbf{s}_N which is $N^{1/2}$ times the standard deviation \mathbf{s} of one component. The full theoretical proof also leads to the exact intensity probability density function $p_N(I)$ provided by the sum of N uncorrelated speckle patterns. The function $p_N(I)$ given below is illustrated in Fig. 5 for $N = 1$ (fully developed speckle pattern), $N = 5$ and $N = 50$:

$$p_N(I) = \left(\frac{N}{I_m}\right)^N \frac{I^{(N-1)}}{(N-1)!} \cdot e^{\left(\frac{-N \cdot I}{I_m}\right)} \quad (35)$$

Therefore, the addition of N statistically independent speckle patterns results in a new reduced contrast C_N given by

$$C_N = \frac{s_N}{NI} = \frac{s}{I} \frac{1}{\sqrt{N}} = \frac{1}{\sqrt{N}} \quad (36)$$

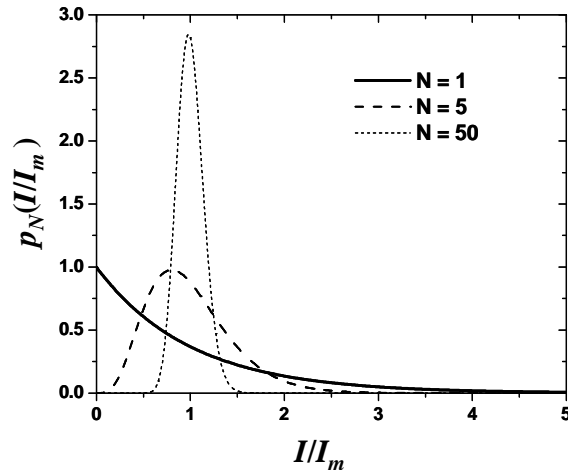


Fig. 5 Statistics of a fully developed speckle pattern ($N = 1$), and its modification obtained by averaging N mutually uncorrelated speckle patterns.

Mutually uncorrelated speckle patterns can be generated by several “physical” means classified by Goodman as “polarization, frequency, space and time diversity”. Either of these “diversity methods” is widely used in various areas for speckle reduction [7]. Post-processing method can also help reducing speckle contrast to a certain extent [10].

2.2.2 Speckle statistics in OCT

Given the major role played by the speckle phenomenon in OCT (see 1.2.3), it is useful to know some of its statistical properties. Presently, two different results for the amplitude distribution of speckles in an OCT signal were reported. Bashkansky and Reintjes [11] calculated a Gaussian distribution yielding a speckle contrast $C = 0.75$, while, more recently, Pircher et al. [12] reported a Rayleigh distribution for which $C = 0.52$, where C is the ratio of the standard deviation to the mean of the signal. The first and second calculations are based on the statistical distribution of the total field on the detector and on the statistical distribution of the field backscattered from the sample, respectively. Pircher et al. attributed the difference between these two results to a possible omission by Bashkansky and Reintjes of the envelope demodulation, which is part of the OCT signal processing. However, although the two results were obtained for different mathematical formulations, the demodulation process was explicitly taken into account in both approaches.

In this section, we show that a modification of an initial assumption in one of the formulation leads to equivalent results.

OCT signal

To analyse and compare the two above results we need to derive the basic relationship between the different electric fields involved in OCT. The detected interference is produced by the superposition of two electric fields corresponding to a large phasor $U_R = A_R e^{j(a \cdot W)}$ from the reference arm and a small random phasor $U_S = A_S e^{jb}$ from the sample. The photodetector is sensitive to the intensity $I_T = U_T U_T^*$, where $U_T = U_R + U_S = A_T e^{jq}$ and where $*$ denotes the complex conjugate.

The constant scan velocity of the reference mirror induces a rotation with a pulsation Ω of the phasor U_R that modulates the intensity of I_T . Since the phase difference \mathbf{j} between U_R and U_S is the relevant variable, either of the two phasors can be taken for the rotating one. For easier representation we choose $U_S = A_S e^{j(\mathbf{b} - \Omega t)} = A_S e^{j\mathbf{j}}$ as the rotating phasor. In addition, without introducing any restriction, we can consider that U_R is a purely real phasor ($\mathbf{a} = 0$). The relationship between the 3 phasors is illustrated in Fig. 6.

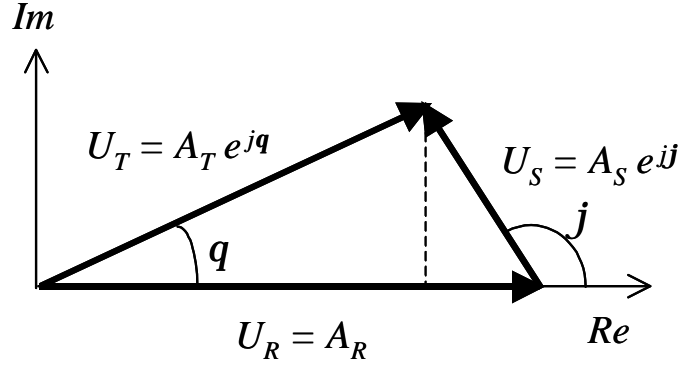


Fig. 6 Summation of phasors in OCT represented in the real (Re) and imaginary (Im) dimension. U_R is the reference field, U_S random sample field, and $U_T = U_R + U_S$.

Let us consider the interference with the highest correlation, i.e. for $g(\mathbf{t}) = 1$, and linearly polarized light. The phasor summation yields the intensity

$$I_t = (U_R + U_S)(U_R + U_S)^* = A_R^2 + A_S^2 - 2A_R A_S \cos(\mathbf{j}), \quad (37)$$

where the argument $\mathbf{j} = \mathbf{b} - \Omega t$.

The effective OCT signal, S_{OCT} , is obtained by bandpass filtering and subsequent envelope demodulation. The first operation removes the two constant intensity terms leaving a modulated signal

$$S_M = 2A_R A_S \cos(\mathbf{j}) \quad (38)$$

After rectification, the demodulation process provides the envelope of S_M . Demodulation has far reaching implications for the calculation of speckle statistics. Indeed, despite the random phase \mathbf{b} of U_S , the amplitude of the demodulated signal corresponds to the alignment of U_R and U_S in the same direction. Since the coherence length typically exceeds a few wavelengths, the phase \mathbf{b} remains constant during a few rotations of U_S . However, the rotation of U_S at a frequency $\Omega/2\pi$ permits the phasors' alignment during each measurement since U_S takes a positive and real value in each cycle at $\mathbf{j} = 0$. Therefore, the demodulated signal amplitude is

$$S_{OCT} = 2A_R A_S \quad (39)$$

Amplitude distribution of speckles in OCT

The two existing results for the amplitude distribution of speckles in an OCT signal were calculated in two different ways. Pircher et al. calculated the field statistical distribution backscattered from the sample (A_S) - which is given by the probability density function of a random phasor sum - and then derived the statistics of S_{OCT} . Bashkansky and Reintjes calculated the statistics of S_{OCT} directly from the statistical distribution of the total field on the detector (A_T) - which is given by the probability density function of a large deterministic phasor plus a random phasor sum. A fully developed speckle pattern in the sample was assumed in both cases.

Let us now examine in detail these two calculations.

In their calculation, Pircher et al. used the field backscattered from the illuminated sample (A_S), which corresponds to a sum of random phasors leading to speckle formation. Assuming a fully developed speckle pattern, the phasor amplitude A_S obeys a Rayleigh probability density function as seen in 2.2.1

$$p(A_S) = \frac{A_S}{\mathbf{s}^2} \exp\left\{-\frac{A_S^2}{2\mathbf{s}^2}\right\}, \quad (40)$$

for $A_S > 0$, while $p(A_S) = 0$, for $A_S < 0$.

The derivation of the OCT signal amplitude distribution can be obtained by a transformation of variable [2] from A_S to S_{OCT} according to Eq. (39), which yields the distribution

$$p(S_{OCT}) = \frac{S_{OCT}}{4A_R^2\mathbf{s}^2} \exp\left\{-\frac{S_{OCT}^2}{8A_R^2\mathbf{s}^2}\right\}, \quad (41)$$

which was obtained both theoretically and experimentally by Pircher et al.

This distribution, which was obtained both theoretically and experimentally by Pircher et al., is a Rayleigh distribution. The ratio of its standard deviation to its mean yields a speckle contrast [12]

$$C = \sqrt{\frac{4}{p}} - 1 \cong 0.52 \quad (42)$$

Note that a Rayleigh distribution is obtained both for A_S and S_{OCT} because A_R is a constant. Indeed, a constant does not modify the statistical distribution of A_S in the above transformation of variable.

We will now examine why a different distribution was obtained by directly using the total field on the detector (A_T). Bashkansky and Reintjes found a Gaussian probability density function leading to a contrast [11]

$$C = \sqrt{\frac{p}{2}} - 1 \cong 0.75, \quad (43)$$

As mentioned above, Pircher et al. attributed this difference to the omission of the envelope demodulation involved in the OCT signal processing. Nevertheless, it appears that the demodulation process was explicitly taken into account in the calculations of Bashkansky and Reintjes who also derived Eq. (39). It appears that instead of using the statistical distribution of A_S , Bashkansky and Reintjes used the probability density function of A_T , for the case $A_T \gg A_S$, which was also derived by Goodman [2]

$$p(A_T) \cong \frac{A_T}{2p\mathbf{s}^2} \exp\left\{-\frac{(A_T - A_R)^2}{2\mathbf{s}^2}\right\} \quad (44)$$

This expression provides the statistical distribution of the phasor length A_T for a phasor argument \mathbf{j} randomly distributed between $-\pi$ and π . Using $p(A_T)$ is in principle also possible. However, although the authors took into account the condition $\mathbf{j} = 0$ to derive a correct expression for S_{OCT} , they did not modify the probability density function $p(A_T)$ accordingly. Indeed, since A_T and S_{OCT} are linked by the angle \mathbf{q} , $p(A_T)$ should be modified to take into account the condition $\mathbf{j} = 0$, i.e. $\mathbf{q} = 0$.

This subtle difference in the mathematical formulation can explain the different result found by Bashkansky and Reintjes.

To verify the relevance of our explanations we will derive the speckle statistics of the OCT signals amplitude using $p(A_T)$ with the condition $\mathbf{j} = 0$. For this purpose, we will use the joint probability density function derived by Goodman [2] for the more general case where no assumption is made on A_T and A_S :

$$p(A_T, \mathbf{q}) = \frac{A_T}{2\mathbf{p}\mathbf{s}^2} \exp \left\{ -\frac{(A_T \cos \mathbf{q} - A_R)^2 + (A_T \sin \mathbf{q})^2}{2\mathbf{s}^2} \right\} \quad (45)$$

We have to calculate the following probability density function:

$$p(S_{OCT}) = p(S_M | \mathbf{j} = 0) = \frac{p(S_M, \mathbf{j} = 0)}{p(\mathbf{j} = 0)} \quad (46)$$

According to the initial assumptions on the random phasor sum, \mathbf{j} is randomly distributed between 0 and 2π , yielding $p(\mathbf{j}) = 1/(2\pi)$. Thus, our conditional probability becomes

$$p(S_M | \mathbf{j} = 0) = 2\mathbf{p} \cdot p(S_M, \mathbf{j} = 0) \quad (47)$$

Now, we need to derive the joint probability density function $p(S_M, \mathbf{j})$ from $p(A_T, \mathbf{q})$. Since there is a one to one mapping in this multivariate probability transformation one can write [2]

$$p(S_{OCT}) = p[A_T(S_M, \mathbf{j} = 0), \mathbf{q}(S_M, \mathbf{j} = 0)] \cdot |J(S_M, \mathbf{j} = 0)|, \quad (48)$$

where $|J|$ is the determinant of the Jacobian

$$|J| = \frac{\partial A_T(S_M, \mathbf{j})}{\partial S_M} \cdot \frac{\partial \mathbf{q}(S_M, \mathbf{j})}{\partial \mathbf{j}} - \frac{\partial A_T(S_M, \mathbf{j})}{\partial \mathbf{j}} \cdot \frac{\partial \mathbf{q}(S_M, \mathbf{j})}{\partial S_M} \quad (49)$$

Geometrical considerations of Fig. 6 with the condition $\mathbf{j} = 0$ yield:

$$A_T(S_M, \mathbf{j}) = \sqrt{A_R^2 + \left(\frac{S_M}{2A_R \cos \mathbf{j}} \right)^2} + S_M, \quad (50)$$

and,

$$\mathbf{q}(S_M, \mathbf{j}) = \arcsin \left\{ \frac{S_M}{2A_R A_T(S_M, \mathbf{j})} \cdot \tan \mathbf{j} \right\} \quad (51)$$

The first and second factors of the Jacobian first term are:

$$\left. \frac{\partial A_T}{\partial S_M} \right|_{\mathbf{j}=0} = \frac{1}{2A_R}, \quad (52)$$

and,

$$\left. \frac{\partial \mathbf{q}}{\partial \mathbf{j}} \right|_{\mathbf{j}=0} = \frac{S_{OCT}}{2A_R \left(A_R + \frac{S_{OCT}}{2A_R} \right)} \quad (53)$$

The second term of the Jacobian is null since the calculation of the first term yields:

$$\left. \frac{\partial A_T}{\partial \mathbf{j}} \right|_{\mathbf{j}=0} = 0 \quad (54)$$

Finally we obtain

$$|J|_{\mathbf{j}=0} = \frac{S_{OCT}}{4A_R^3 + 2A_R S_{OCT}}, \quad (55)$$

Calculation of the probability term multiplied by the Jacobian in Eq.(48) is straightforward. The condition $\mathbf{j} = 0$ in Eq. (50) yields

$$A_T(S_M \mathbf{j} = 0) = A_R + \frac{S_{OCT}}{2A_R}, \quad (56)$$

and, in turn

$$p[A_T(S_M \mathbf{j} = 0), \mathbf{q}(S_M \mathbf{j} = 0)] = \frac{1}{2\mathbf{p}\mathbf{s}^2} \left(A_R + \frac{S_{OCT}}{2A_R} \right) \exp \left\{ \frac{S_{OCT}^2}{8A_R^2 \mathbf{s}^2} \right\} \quad (57)$$

Eventually, we can calculate the conditional probability density function of interest:

$$p(S_{OCT}) = 2\mathbf{p} \cdot p[A_T(S_M \mathbf{j} = 0), \mathbf{q}(S_M \mathbf{j} = 0)] \cdot |J|_{\mathbf{j}=0} = \frac{S_{OCT}}{4A_R^2 \mathbf{s}^2} \exp \left\{ -\frac{S_{OCT}^2}{8A_R^2 \mathbf{s}^2} \right\}, \quad (58)$$

which is precisely the Rayleigh distribution of Eq. (41) obtained with the distribution of the random phasor A_S .

Thus, it follows that the correct theoretical amplitude distribution of speckles in an OCT signal does well obey a Rayleigh distribution, whose contrast C equals 0.52. We have shown that this conclusion can be reached in two different ways, namely with a calculation based either on the distribution of the field backscattered from the sample or on the distribution of the total field on the detector. The second calculation happened to be far more complicated and tricky. The origin of the difference between the two results reported in the literature is now fully accounted for.

References

- [1] M. Born, and E. Wolf, "Principle of Optics," 7th (expanded) edition, Chap X (Pergamon Press Oxford, 1999).
- [2] J.W. Goodman, "Statistical optics, Chap 2&5 (Wiley Classics Library, 1985).
- [3] B.E.A. Saleh, and M.C. Teich, "Fundamentals of Photonics," Chap 10 (Wiley et Sons, new York, 1991).
- [4] E.A. Swanson, D. Huang, M.R. Hee, J.G. Fujimoto and al., "High-speed optical coherence domain reflectometry", *Opt. Soc. Am.* **17**, 151-153 (1992).
- [5] L. Mandel et E. Wolf, "Optical coherence and quantum optics", Chap IV, (Cambridge University Press, 1995).
- [6] J.W. Goodman, "Some fundamental properties of speckle," *J. Opt. Soc. Am.* **66**, 1145-1150 (1976).
- [7] J.W. Goodman, "Statistical properties of laser speckle patterns", in *Laser speckle and related phenomena, Topics in applied physics: Vol. 9* ed: J.C. Dainty 9-75 (1975).
- [8] N. George and A. Jain, "Speckle Reduction Using Multiple Tones of Illumination," *Appl. Opt.* **12**, 1202-1211 (1973).
- [9] H. M. Pedersen, "On the contrast of polychromatic speckle patterns and its dependence on surface roughness," *Optica Acta* **22**, 15-24 (1975).
- [10] J.M. Schmitt, S.H. Xiang, K.M. Yung, "Speckle in Optical Coherence Tomography," *J. Biomed. Opt.* **4**, 95 (1999).
- [11] M. Bashkansky and J. Reintjes, "Statistics and reduction of speckle in optical coherence tomography," *Opt. Lett.* **25**, 545-547 (2000).
- [12] Pircher. M., E. Goetzinger, R. Leitgeb, A. F. Fercher, C. K. Hitzenberger, "Speckle reduction in optical coherence tomography by frequency compounding," *J. Biomed. Opt.* **8**, 565-569(2003).

CHAPTER III

Wide-field optical coherence tomography with spatially coherent illumination

Chapter III is mainly devoted to wide-field optical coherence tomography (OCT) with coherent illumination. It is divided into three main sections each of them corresponding to a publication of direct relevance to this topic [1-3]. However, the model developed in section 3.2, and applied to wide-field OCT in section 3.3, is far more comprehensive since applicable to OCT in general.

Section 3.1 provides the experimental proof of feasibility of wide-field OCT in scattering samples using a smart-pixel detector array. Demonstration is made with a resolution target covered by an intralipid solution with different scattering coefficients as well as onion cells. Analyses of the results raise fundamental questions, which are addressed in the rest of the chapter. Some elements of the discussion are sometimes incomplete or even inaccurate since reflecting the level of knowledge at the time of this preliminary study. The next two sections provide a deeper understanding of the phenomena involved.

In section 3.2, we present a new model of OCT taking into account multiple scattering. We explain first why multiple scattering does not induce a loss of spatial coherence of the sample field and show that the latter is stationary relative to measurement time. These facts, revealing that the reference and sample fields are fully correlated to the contrary of the widespread belief, allow us to model an OCT signal as a sum of stationary random phasors and treat it as a statistical signal. The mean of this signal can be calculated thanks to classical results of statistical optics and to a Monte Carlo simulation. Our model accounts for the source autocorrelation function as verified by depth scan measurements on a sample consisting of a mirror covered with a microbeads' solution. We discuss the applicability of

models based on the extended Huygens-Fresnel principle, which involve spatial coherence effects, and thus rest on different assumptions.

In section 3.3, we present a comprehensive study of multiple scattering effects in wide-field OCT realized with spatially coherent illumination. Imaging a sample made of a reflective edge break embedded in a microbeads' solution revealed that, despite temporal coherence gating, multiple scattering can induce significant coherent optical cross-talk. The latter is a serious limitation to the method since it prevents shot-noise limited detection and diffraction-limited imaging in scattering samples. We investigate the dependence of cross-talk on important system design parameters, as well as on some relevant sample properties. The agreement between theoretical and experimental results for the wide range of parameters investigated was very good, in both the lateral and the axial dimensions. This further confirms the validity of the model developed in section 3.2.

3.1 Wide-field OCT in scattering samples

3.1.1 Introduction

Optical coherence tomography (OCT) allows acquisition of spatially resolved maps of reflectivity in scattering samples. In most common OCT systems, depth scanning is achieved by the longitudinal translation of a reference mirror, and lateral scanning is obtained by lateral translation of focused probe beam using scanning mirrors [4-6]. To increase the acquisition speed and eliminate the need for lateral scanning, parallel detection schemes have been investigated [7-10]. Parallel OCT systems previously developed consist of a free-space Michelson interferometer illuminated by a short temporal coherence source. The sample under study is placed in one arm of the interferometer, illuminated with a uniform extended beam and imaged on an array of photodetectors. Charge coupled devices (CCD) cameras are the most commonly used imaging devices for parallel detection schemes. However, CCD cameras suffer from two drawbacks when used in parallel OCT systems:

- (i) the high optical DC intensity reflected by the reference mirror reduces the dynamic range available for AC interferometric signal detection,
- (ii) the CCD frame rate (typically ~ 100 Hz for 512×512 pixels) is much lower than the interferometric signal frequency (typically > 1 kHz).

In this case a lock-in detection or synchronous illumination scheme has to be employed [8], which limits the acquisition speed. A different photodetector array based on CMOS technology was developed for parallel OCT [11,12]. Besides transducing light signals into electrical signals, CMOS detectors offer the additional functionality of customized, integrated signal processing for each pixel. Such smart pixel detector arrays (SPDA) have been developed for OCT interferometric signal demodulation. The feasibility of using one- and two-dimensional SPDAs for OCT was demonstrated on reflective surfaces [10,11].

In the present work we demonstrate the feasibility of employing a SPDA to obtain parallel OCT images in scattering samples.

3.1.2 Method

Optical set-up

The optical set-up is illustrated in Fig. 1. The output of a femtosecond mode-locked Ti:Sapphire laser (MLTS) is coupled into 100 m of single-mode optical fiber in order to reduce peak pulse powers by pulse stretching. Dispersion in the fiber increases the temporal width of the laser pulses, which reduces dramatically the peak power. This precaution is taken to avoid damage to the sample and the optics. The fiber output is collimated by lens L_2 and linearly polarized by polarizer P. An average power of 100 mW is coupled into a free space Michelson interferometer. The light spectrum is nearly Gaussian and has a full-width at half-maximum (FWHM) of 70 nm centered at 800 nm. The resulting system axial resolution is 4 μm . A non-polarizing beamsplitter cube (BS) separates the light into the interferometer reference and sample arms. Two identical 20x achromatic microscope objectives (L_4 and L_5) are used to illuminate and collect reflected light from the sample (S) and the reference mirror (RM). Light reflected from S and RM interferes only if the optical path lengths match to within the source coherence length. RM is translated longitudinally using a voice coil scanning stage at a speed of 1.17 mm/s inducing a heterodyne interference signal at a frequency of 2.9 kHz. The sample is imaged onto the detector (SPDA) with a magnification of 25 by lens L_6 and microscope objective L_4 . The detector is composed of 58 by 58 smart pixels. One pixel consists of a $35 \times 35 \mu\text{m}^2$ silicon photodiode coupled to a CMOS electronic circuit that amplifies and demodulates AC signals, delivering an analog voltage proportional to the envelope of the optical interference signal [11,12].

The photodiode covers 10% of the total pixel area ($110 \times 110 \mu\text{m}^2$), the rest being occupied by the CMOS electronic circuit. Due to the detector photosensitive fill factor and to optical system losses, the DC optical power reflected from the reference mirror and incident onto each photodiode is 170 nW. The incident power on the sample is 340 nW. The pixels are read out sequentially and the output voltage is digitized by an external 12-bit A/D card at a sampling rate of 2.5 MHz and stored in the computer memory. Volumetric images consisting of $58 \times 58 \times 600$ voxels ($260 \times 260 \times 950 \mu\text{m}^3$) are acquired in 0.8 s. The user can display on the computer screen any two-dimensional cross sectional image from the 3-dimensional data set.

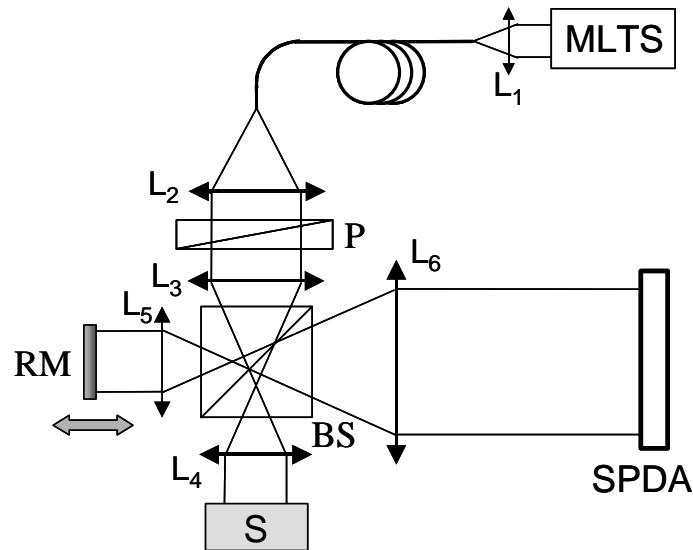


Fig. 1 Optical setup schematic. The different elements are: mode-locked Ti:Sapphire femtosecond laser (MLTS); achromatic lenses ($L_1=f8$, $L_2=f40$, $L_3=f140$, and $L_6=f200$); linear polarizer (P); non-polarizing achromatic beamsplitter cube (BS); achromatic microscope objectives 20x, 0.45 NA (L_4 and L_5); reference mirror (RM); 58 by 58 smart pixel detector array (SPDA) and sample (S).

Due to the small depth of field (Rayleigh range of $4.6 \mu\text{m}$) of the microscope objectives L_4 and L_5 , care has to be taken to place the region of interest in the sample at the focal plane of L_4 . Replacing temporarily the SPDA with a standard CCD camera we adjusted the longitudinal position of the sample with a micrometer translation stage to obtain a focused image on the CCD camera.

Samples

Two kinds of sample were used in the present work. Sample 1 is a cuvette constructed with four microscope cover slips glued on a USAF resolution target (Fig. 2). A drop of intralipid scattering solution is deposited in the cuvette and a top cover slip is pressed down to close the cuvette and remove the excess solution. We varied the intralipid solution scattering coefficient (μ_s) between 0 cm^{-1} and 100 cm^{-1} by dilution of 20% Lipovenös® intralipid solution (Fresenius AG, Switzerland). μ_s was measured using the collimated transmission method described by van Staveren et al. [13].

Note that the total thickness of the sample is larger than the depth of field of L_4 , which means that it is impossible to have a well-focused image for all depth positions in one scan. The transverse resolution is optimum at the focal plane and degrades below and above. However, scanning the whole volume of the sample provides an accurate measurement of the thickness of the intralipid solution that can vary slightly due to a liquid film between the cover slip. The USAF resolution target was placed at the focal plane of L_4 .

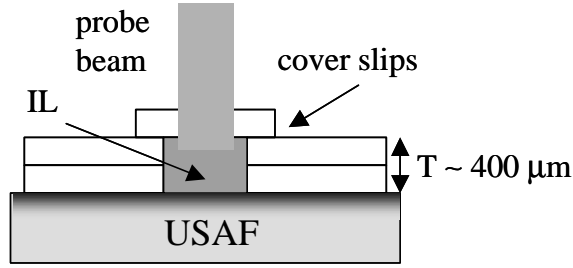


Fig. 2 Schematic of sample 1. The probe beam illuminates from top to bottom one microscope cover slip, a scattering intralipid solution (IL) approximately 400 μm thick, and the USAF resolution target.

Sample 2 is an onion. The probe beam penetrates from the outer surface of the onion. Images are acquired with the focal plane placed at the surface and approximately 100 μm below the surface.

3.1.3 Results and discussion

System performances

We measured the system axial resolution (FWHM) on a mirror in air to be 4 μm . The depth resolution measurement was repeated on the reflective bars of the USAF resolution target placed behind a layer of scattering intralipid solution (sample 1) and the same result was obtained. Thus, in first approximation (see 3.2.2), neither scattering nor dispersion degrades the system longitudinal resolution as measured in sample 1. Transverse resolution in air was determined using the USAF resolution target patterns. We could resolve reflective bars with a maximum spatial frequency of 114 lines/mm, which corresponds to a transverse resolution of 8.8 μm . We measured the system maximum signal-to-noise ratio (SNR_{max}) to be 50 dB. The SNR is defined as the ratio between the following two quantities: V_{signal} , the detector output voltage for a voxel that corresponds to the image of a reflective site and σ_{noise} , the standard deviation of the measured voltage on all voxels without a sample. SNR in decibel is:

$$\text{SNR}(dB) = 20 \log \left| \frac{V_{\text{signal}}}{\sigma_{\text{noise}}} \right| \quad (1)$$

When the reflective surface is a gold mirror with reflectivity 0.98 we measure $\text{SNR} = 50$ dB, which we consider to be the maximum SNR obtainable with our system.

Parallel OCT in scattering samples

For a rigorous performance analysis this value has to be compared to the maximum theoretical SNR ($\text{SNR}_{\text{th,max}}$) for a shot-noise limited system, which is given by the following formula [14,15]:

$$\text{SNR}_{\text{th,max}} = 10 \log \left(\frac{h}{2h\nu} \frac{P_{s,\text{max}}}{B} \right), \quad (2)$$

where $P_{s,\text{max}}$ is the maximum power coming from the sample arm (as seen by one photodiode of the detector), B the detection bandwidth, h the quantum efficiency, h Planck's constant and ν is the optical frequency of the light used. We have measured the bandwidth of the SPDA detector tuned for optimum performance in the experimental conditions to be 120 kHz and estimate the quantum efficiency to be 0.5, which gives a theoretical shot-noise limited SNR of 61.5 dB. The observed detection limit was thus 11.5 dB above the shot-noise limit. We attribute this difference to additional read-out noise generated by the electronic circuitry.

Note that the optimum filtering bandwidth B to filter out as much noise as possible without attenuating the OCT signal is given by [15]

$$B = 2 \frac{\Delta I}{I} f_{\text{Doppler}}, \quad (3)$$

ΔI being the source spectrum FWHM, I the source spectrum central wavelength and f_{Doppler} the interference fringes frequency. In the current experimental settings, B is 508 Hz, and the maximum obtainable shot noise limited SNR is 85 dB.

The large filtering bandwidth of 120 kHz used in our experiments is due to an intrinsic limitation of the electrical circuitry of the SPDA for the given experimental conditions. Indeed, being conceived for heterodyne frequencies of the order of 100-300 kHz, this detector has a rather poor filtering performance for low heterodyne frequencies. Furthermore, the achievable minimum filtering bandwidth also increases with the light power illuminating the detector, which was in the current study rather higher than in previously published experiments [11]. We have nevertheless employed a slow reference mirror scanning velocity (resulting in a low OCT signal frequency of 2.9 kHz) in order to sample the high axial resolution (4 μm) given by the short temporal coherence of the femtosecond laser source. The bottleneck is the pixel read-out rate of 2.5 MHz (5 MHz with some reduction in image contrast), which does not permit to sample a sufficient number of points per coherence envelope at high heterodyne frequencies.

Images of USAF resolution target

In Fig. 3 the presented longitudinal cross section (Fig. 3a) and *en face* images (Fig. 3b/c) of sample 1 are presented. The sample longitudinal position is adjusted to bring the surface of the resolution target into focus on the SPDA. The field of view is centered on elements 5 and 6, group 4, of the resolution target. In Figures 3a and 3b the target is covered by 400 μm water. The three lines in Fig. 3a at optical distances of 0, 270 and 800 μm correspond to the two interfaces of the glass slide and the resolution target, respectively. The optical thickness measured on the longitudinal cross-sections (Fig. 3a) are used to determine the physical thickness of intralipid solution, assuming an index of refraction of 1.33. In Fig. 3c the resolution target is covered by 385 μm intralipid solution with μ_s of 100 cm^{-1} , which corresponds to nearly 4 scattering mean free paths (single pass). For greater scattering samples the pattern was undistinguishable.

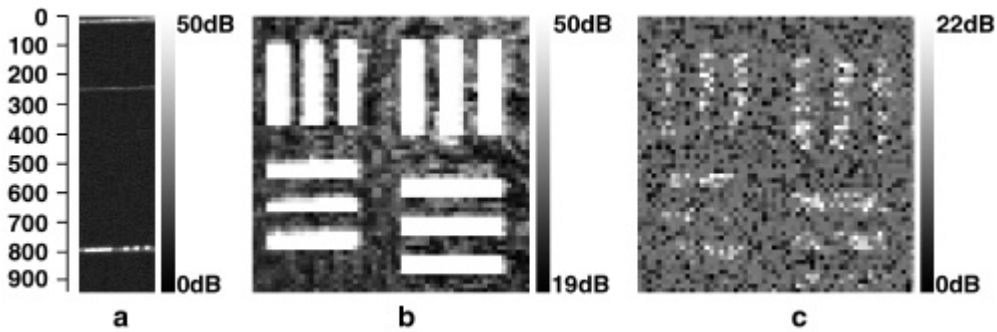


Fig. 3 Longitudinal cross-section ($260 \times 950 \mu\text{m}^2$) (a) and *en face* ($260 \times 260 \mu\text{m}^2$) images of the resolution target behind 400 μm water (a and b) and intralipid solution $\mu_s = 100 \text{ cm}^{-1}$ (c). The intensity scale corresponds to the SNR in dB. Depth scale on the left of (a) is in microns.

For a quantitative assessment of imaging performance, the signal from a reflective bar of the USAF resolution target was measured as a function of the number of scattering mean free path, also called optical depth (OD). The results are presented in term of SNR as a function of OD (Fig. 4), with

$$OD = \mathbf{m}_s \cdot t, \quad (4)$$

where μ_s and t are the measured intralipid solution scattering coefficient and thickness respectively. Note that for the intralipid solution concentration and the wavelength employed, $\mu_a \ll \mu_s$ [13,16]. Therefore, we neglected \mathbf{m}_t in the calculation of OD.

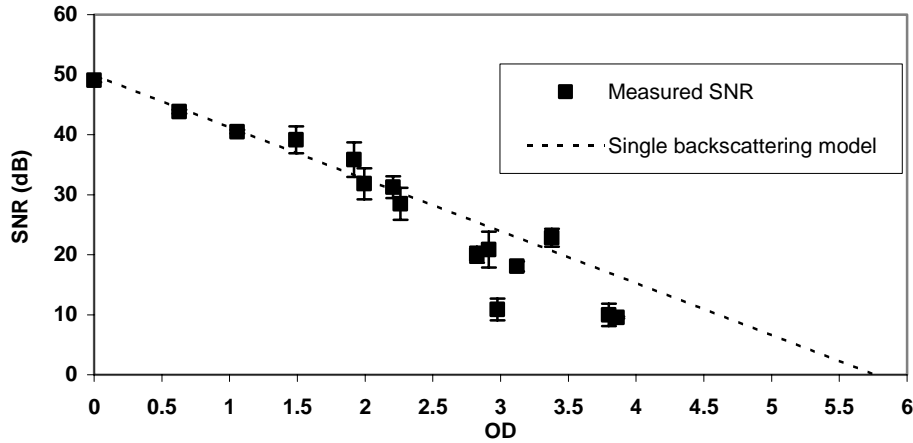


Fig. 4 SNR (square dots) measured from a reflective bar of the USAF resolution target behind $\sim 400 \mu\text{m}$ intralipid scattering solution as a function of the scattering solution optical depth (OD). The dashed line represents the OCT signal attenuation according to a single backscattering model.

According to an accepted model of OCT in scattering media [17-19], the greatest light contribution to OCT signals comes from single backscattered photons. Therefore, mainly photons that are not scattered in the round trip travel in the intralipid solution and are reflected by the USAF resolution target reflective elements contribute to the signal. To compare our measurements with this model we plotted (dashed line in Fig. 4) the OCT signal (SNR_{model}) according to Beer's law attenuation as a function of optical depth (OD):

$$SNR_{\text{model}} = 20 \log \left(\frac{2\sqrt{e^{-\mu_s 2t} I_R I_S}}{\sigma_{\text{noise}}} \right) = SNR_{\text{max}} + 10 \log \left(e^{-2OD} \right), \quad (5)$$

where I_R and I_S are the coherent light power incident on the detector that are reflected by perfect mirrors in the reference and sample arms respectively. SNR_{max} is the maximum SNR, i.e. 50 dB (measured) in our case.

The measured SNR values for ODs up to 2.5 correspond well to the exponential decay given by the single scattering model, but for $OD > 2.5$ significant differences are observed which could be explained by the following two sources of error. First, for samples with $OD > 2.5$, the use of a CCD camera for longitudinal positioning of the USAF resolution target becomes impractical because the pattern is not distinguishable anymore through the turbid media. In those conditions the uncertainty on sample longitudinal positioning increases and the measured signals are lower than they would be if the USAF target was placed exactly at the objective focal plane. Secondly, the scattering coefficient could be underestimated for samples with $OD > 2.5$. Indeed, when measuring μ_s with the collimated light transmission method described in [13], very weak signals have to be measured for highly scattering samples. In this case, the signals might be overestimated due to signal noise, which induces an underestimation of μ_s .

Furthermore, for scattering samples with $OD > 2$, Yadlowsky, et al. [18] demonstrated that the single backscattering model fails to describe accurately the attenuation of OCT signals. At depths greater than 2.5 OD, multiply scattered photons contribute significantly to OCT signals. In particular, when the scattering medium is composed of particles with diameters smaller compared to the wavelength, which is the case with the intralipid solution (intralipid particles average diameter measured by Van Staveren et al. [13] is 93 nm), multiply scattered photons induce a background haze and loss of contrast. This could explain why we were not able to discern the reflecting bars under USAF resolution target beyond 4 OD, even though the single backscattering model indicates that the limit is approximately 5.7 OD (intercept of the SNR_{model} dashed line with zero dB level in Fig. 4). Another effect that could be responsible for the lower than expected signals is speckle. The situation

can be compared to a random walk speckle model (the scattering medium) together with a constant phasor (the reference beam) [20]. The averaging of speckles might have reduced the measured signals.

Finally, the technique of parallel detection itself might be at the origin of the differences between observations and single backscattering model. By illuminating the whole sample field at once in contrast to point-by-point beam scanning, there is the possibility for an optical cross-talk between pixels that could reduce contrast. Although each SPDA photodiode ($35 \times 35 \mu\text{m}^2$) is equivalent to a sample conjugated pinhole, it cannot reject entirely out of focus light. The chance of detecting coherent photons backscattered from a site outside of the imaged voxel is increased by illuminating a large sample area instead of focusing the illumination beam on a single point, as in a confocal system. This issue makes the object of a thorough investigation in section 3.3.

Images of onion cells

In Fig. 5 are presented longitudinal cross-sectional (Fig. 5a) and *en face* images (Fig. 5b/c) of an onion. Figures 5b and 5c are the images of cell layers at the surface and $100 \mu\text{m}$ below the surface of the onion, respectively. The sample longitudinal position was adjusted to bring the images presented in Figures 5b and 5c into focus. Backscattered light is detected in the cross sectional image up to a depth of approximately $450 \mu\text{m}$. One clearly distinguishes cell boundaries in the *en face* images.

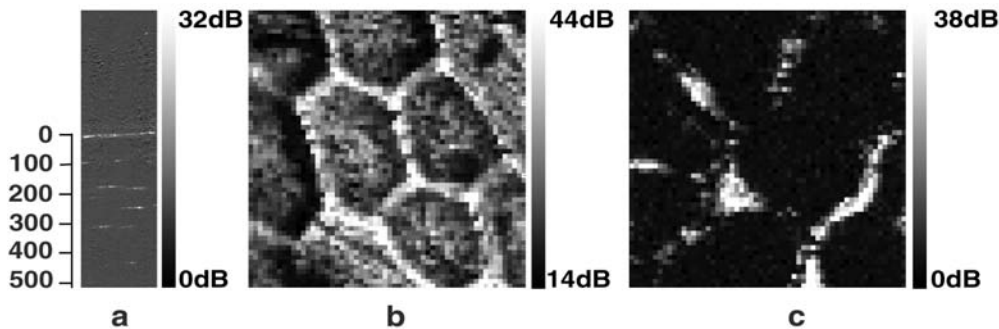


Fig. 5 Longitudinal cross-section ($260 \times 950 \mu\text{m}^2$) (a) and *en face* ($260 \times 260 \mu\text{m}^2$) images of onion at a depth of ~ 0 (b) and $100 \mu\text{m}$ (c). The intensity scale corresponds to the SNR in dB. Depth scale on the left of (a) is in microns.

3.1.4 Conclusions

These results show the performances of our parallel OCT system using a SPDA for imaging scattering samples. To our knowledge it is the first demonstration of the use of CMOS smart-pixel technology for parallel OCT in scattering phantoms and biological samples. Volumetric image acquisition is achieved at a relatively high speed (2.5×10^6 pixels/s) compared to OCT systems using transverse scanning mechanisms (up to 2×10^6 pixels/s [21]). However, imaging depth penetration is currently limited by the SNR of the system (50 dB compared to 90 dB in [21]).

Furthermore, using a femtosecond light source combined with a microscopic imaging scheme, we obtained high longitudinal and transverse resolutions. However, transverse resolution depends strongly on the distance to the object focal plane. Further improvements of imaging performances rely on future developments of SPDAs (greater dynamic range, pixel read-out rate and number of pixels) as well as a dynamic focusing mechanism to maintain transverse resolution throughout the entire depth scan.

Discrepancies between our results and the simple backscattering model raise fundamental questions. As shown in the rest of the chapter, the 3 physical phenomena potentially accounting for the former (see 3.1.3), namely the background haze induced by multiply scattered photons, speckles, and optical cross-talk, share a common origin i.e. multiple scattering.

3.2 Modeling multiple scattering in OCT

3.2.1 Introduction

The past decades witnessed the emergence of several valuable optical imaging methods allowing to visualize the inner structure of biological specimen. However, image quality is often limited by multiple scattering, which reduces contrast, resolution and maximum probing depth. The major challenge of imaging in turbid media with diffraction-limited performance is thus to efficiently reject multiply scattered light while detecting ballistic light. To realise this, physical principles such as spatial filtering, time resolved detection or coherent detection are exploited [22]. Excellent discrimination is achieved by combining confocal spatial filtering with temporal coherence gating as in optical coherence tomography (OCT) [14]. However, multiple scattering still remains an important limiting factor in highly scattering media e.g. [18,23]. A deeper understanding of the role played by multiple scattering in OCT should allow to better evaluate the system limitations and provide some guidance for improving instrument design and data processing algorithms.

A comprehensive model of OCT requires modeling both the light propagation in random media and the interference process, which depends on coherence properties of the sample field. Light propagation in random media, including temporal aspects, can be described quite successfully by the time-resolved diffusion theory [24,25]. However, this theory is based on the diffusion approximation, which becomes valid only after a few scattering events [26] yielding delays of a few picoseconds [25,27]. Such delays, which largely exceed typical source coherence times in OCT, correspond to considerable pathlengths, i.e. in the order of one millimetre. Therefore, models based on the diffusion approximation fail to properly describe multiply scattered light distribution in the range of interest met in OCT where pathlengths are one to three orders of magnitude lower. A numerical calculation performed by a Monte Carlo simulation can provide the spatio-temporal distribution of light within the entire range of interest [25,27]. Several existing models of OCT are based on Monte Carlo simulation e.g. [19,28,29]. However, the latter cannot, in principle, account for the coherence properties of multiply scattered light, whose knowledge is indispensable in the context of coherent detection techniques.

It is generally believed that multiple scattering causes a loss of spatial coherence of the sample field causing reduction of the interference contrast. A model of OCT, first introduced by Schmitt and Knuettel [30], and further improved by Thrane et al. [23], accounts for spatial coherence properties of the sample field. This model is based on the so-called extended Huygens-Fresnel principle [31], an analytical model based on the radiative transport theory, and the use of mutual coherence functions [31,32]. To date, it is the most comprehensive model of OCT.

In section 3.2.2, we investigate the coherence properties of the backscattered sample field in OCT and conclude that multiple scattering does actually not induce a loss of spatial coherence of the sample field and that the latter remains fully correlated with the reference field. This allows us to build a model based on fundamentally different assumptions. The OCT signal is modeled as a sum of stationary random phasors and treated as a statistical signal. The mean of this signal can be calculated thanks to classical results of statistical optics and to a Monte Carlo simulation. We present a preliminary experimental validation of our model, as well as details relevant to its practical implementation. In section 3.3, our model is shown to be in excellent agreement with a whole range of experimental data gathered in a comprehensive study of cross-talk in wide-field OCT. These observations, in addition, raise questions on the applicability of models based on the extended Huygens-Fresnel principle, which involve spatial coherence effects, and thus rest on different assumptions. This important point is discussed in detail with experimental support. We also briefly discuss other models based on Monte Carlo simulations.

3.2.2 Preliminary experiment

In this section, we investigate some effects and properties of multiple scattering in OCT. This requires an experiment where multiply scattered light plays a significant role. This is the case in wide-field OCT when the sample is illuminated with spatially coherent light as shown in a recent study [33]. Thus, we use here a typical wide-field OCT interferometer [1] and a scattering sample. Usually, the sample is imaged onto a detector array, where each detector is a sample-conjugated point matching the resolution of the imaging system. In this preliminary experiment we use only one detector positioned at the optical axis. The experimental set-up used for the measurements presented here below is fully described in section 3.3.2. The wide-field diameter is 420 μm diameter at full width at half maximum (FWHM) and the numerical objective of the sample objective is 0.25. A mode-locked femtosecond Ti:Sapphire laser, with a spectral bandwidth of 70 nm (FWHM) centered at 800 nm, is used as a light source.

The measured signal envelope of the source autocorrelation function is shown in Fig. 6. The corresponding axial resolution in air is approximately 7.5 μm . A very different signal is obtained when the sample arm mirror is covered with scattering solution. The latter consists of a microbeads solution yielding an optical density (OD) of 8 and an anisotropy (g) of 0.85. Despite temporal coherence gating, signals caused by the unrejected multiply scattered light are measured far beyond the mirror interface. For a single scan, a speckled signal much longer than the autocorrelation function envelope at FWHM - and different for each measurement - is obtained. When averaging 25 of these random envelopes, we obtain a correlogram forming a tail nearly an order of magnitude larger than the autocorrelation signal at FWHM. Thus, in our case, the axial resolution is on the average one order of magnitude lower.

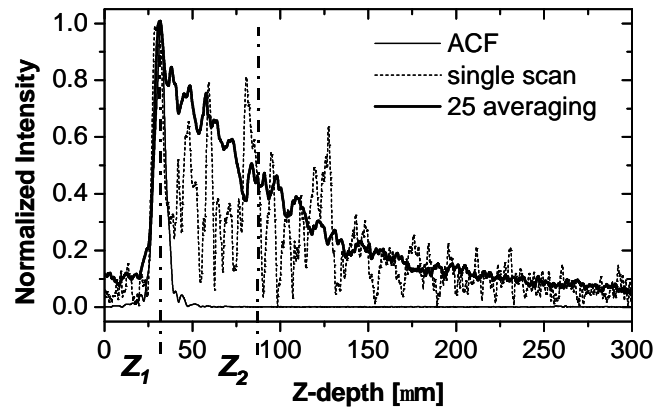


Fig. 6. Correlogram envelopes obtained in wide-field OCT with a sample consisting of a mirror covered with scattering solution (8 OD, $g = 0.85$) for a single scan (dashed curve) and for the average of 25 envelopes (thick solid curve). The thin solid curve represents the envelope of the source autocorrelation function (ACF) measured in water. Z_1 is the sample mirror position and Z_2 is 60 μm away from Z_1 . Speckle statistics is measured at $Z_{1/2}$. All correlograms are normalized and plotted against the reference mirror position.

The random nature of a signal as obtained for a single scan is due to multiply scattered light, which gives rise to speckle formation. Speckle intensity depends on the measurement position along the optical axis. Moreover, since the scatterers change randomly their positions due to Brownian motion, which induces a time-varying signal, a different random signal is obtained for each measurement. Since the detector size matches the lateral resolution of the imaging system, a single time-varying speckle is detected.

For further argumentation it is important to determine the statistical properties of these speckles at a fixed axial position. The time between successive scans, here around 0.5 s, is long enough to obtain speckles with different phases and intensities at each measurement. To estimate the intensity speckle

statistics at the two axial positions Z_1 and Z_2 , we took 1000 measurements of demodulated signal intensity at each of these positions. At position Z_1 , both ballistic and multiply scattered light contributions are present, whereas, at position $Z_2 = Z_1 + 60 \mu\text{m}$, signals are essentially due to multiply scattered light. From the intensity distribution at these two points we derived the contrast defined as $C = \sigma/\mu$, where μ is the average and σ the standard deviation of the signal intensity distribution. Contrast obtained was $C_1 = 0.25$ and $C_2 = 0.5$ at Z_1 and Z_2 , respectively. This last value is very close to the theoretical contrast of a Rayleigh distribution where $C = 0.52$. The histogram of the 1000 intensity measurements (distributed into $k = 125$ bins) follows well a Rayleigh distribution (Theory) as shown in Fig. 7. This distribution is expected for a fully developed speckle pattern in OCT as shown by Pircher et al. for point scanning OCT [34].

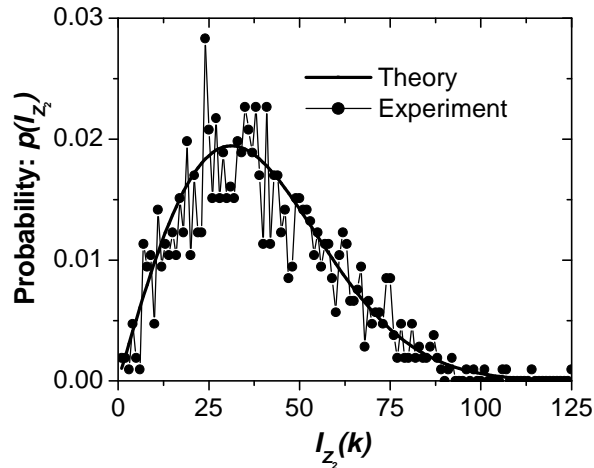


Fig. 7. Histogram of the signal intensity distribution measured at position Z_2 (Experiment), indicated in Fig. 6, against the Rayleigh probability density function (Theory).

Note that averaging signal envelopes reduces the speckle contrast. Indeed, averaging N speckle envelopes is equivalent to averaging N uncorrelated speckles since the phase information is washed out in the envelope demodulation. The speckle contrast is known to diminish with the square root of N [20]. Thus, the average of 25 signals, as shown in Fig. 6, reduces the contrast in principle by a factor of five i.e. to $C = 0.1$ at Z_2 .

3.2.3. Multiple scattering and interference

Our preliminary experiment revealed that multiply scattered light could interfere with the reference field. It is crucial to determine whether the interference is complete or only partial, i.e. whether the interference contrast is maximum or not.

Let us examine under what conditions multiple scattering can cause a reduction of the interference contrast. The maximum contrast is obtained with both spatially and temporally coherent interfering fields. A partially spatially coherent sample field generally yields a loss of correlation with the reference field and in turn a reduction of interference contrast. However, in both wide-field and point scanning OCT, light collected from the sample by a single detector can be but spatially coherent. Indeed, since the detector size matches the lateral resolution of the optical system, the speckles created by the coherent illumination are in the size order of a single detector. Light confined within one speckle is by nature spatially coherent. Performing the Young's experiment within one speckle would indeed yield an intensity fringe pattern with maximum contrast [35]. Thus, in principle, despite multiple scattering, spatial coherence effects do not induce a reduction of interference contrast.

Let us now determine whether temporal coherence effects can yield a reduction of interference contrast. In OCT, which relies on low coherence interferometry, the reference mirror is scanned so as to measure fully correlated fields when optical pathlengths are equivalent in both arms. Thus, only

time-varying random phenomena in one arm of the interferometer could induce a loss of correlation. This can happen for a random time-varying sample field due to sample motion. The interference contrast can be reduced as explained with help of Fig. 8. The reference and sample fields, respectively U_R and U_S , are shown separately while propagating along the same optical axis (OA) in the detector arm. U_R is deterministic while U_S is random due to multiple scattering contribution.

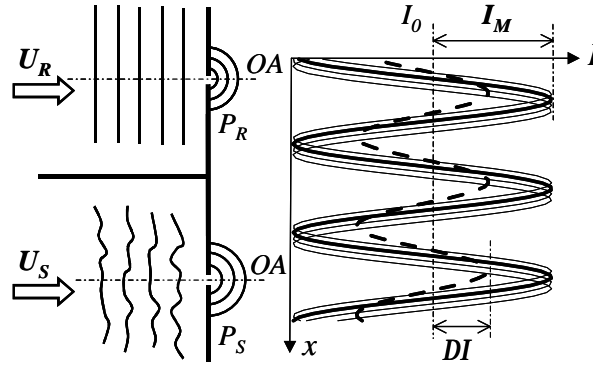


Fig. 8 Scheme illustrating the loss of correlation between a deterministic reference field (U_R) and a random sample field (U_S), by means of Young's experiment where each field is sampled independently with one of the two pinholes. The plot illustrates the loss of contrast for fast variation of U_S relative to measurement time.

Let us envisage that U_R and U_S are sampled independently at the same position along OA. With the corresponding pinholes P_R and P_S we perform Young's experiment. Each field can be described by a phasor at the pinhole position. When the two phasors are correlated (i.e. phase difference constant), light from the two pinholes interferes and creates a stationary sinusoidal intensity fringe pattern with maximum contrast ($I_0/I_M=1$). The phase difference between the two phasors determines the lateral phase shift of the fringe intensity pattern along the x-axis. When the two phasors are no more correlated, i.e. when the sample field phasor varies randomly with time, many laterally shifted intensity sinusoidal patterns are created. This can lead to a reduced contrast ($DI/I < 1$) provided the measurement time is long enough to allow the integration of many laterally shifted fringe patterns (see Fig. 8).

Therefore, as shown in very close context [35], the interference contrast depends on the time scale of the sample field fluctuations relative to measurement time. For slow fluctuations relative to measurement time, the sample field is nearly stationary (frozen) and the interference contrast maximum. Our sample consists of a microbeads' solution subject to Brownian motion. We will show experimentally that the time fluctuations induced by the Brownian motion to the sample field are negligible during the characteristic measurement time scale T_D . The latter is in the order of the time necessary for building one fringe of the interferogram when moving the reference mirror. Thus, T_D corresponds to the inverse Doppler frequency induced by the reference mirror displacement. With a Doppler frequency equal to 6.7 kHz in our case (see 3.3.2), $T_D = 150 \mu\text{s}$.

To experimentally verify the sample field stationarity we slightly modified our preliminary experiment. The same experimental conditions and sample (8 OD, $g = 0.85$) were used but the reference mirror was immobilized so as to measure the time-varying interference signal induced by Brownian motion. Measurement was taken at position Z_2 where the multiply scattered light contribution dominates. To be able to measure fluctuations over a wide frequency range, a large bandpass filter ranging from 0.5 Hz to 150 kHz was used.

The measured signal, i.e. the fluctuation of the speckle phasor, is shown for two different time scales in Fig. 9. In Fig. 9a, where the time scale is of 1 second, fluctuations are in the order of one hundred milliseconds. The time between successive scans, $T_C = 0.5 \text{ s}$, is large enough to allow the speckle phasor to undergo a few 2π cycles, allowing fully constructive (maxima) and fully destructive interference (minima) with the reference field. Fig. 9b shows the same signal for a much smaller time

scale, one order of magnitude larger than $T_D \cong 150 \mu\text{s}$. In this case the average signal is nearly flat (dashed line in Fig 4b) showing that the signal remains constant during T_D . Signal fluctuations around the average correspond to the significant amount of noise detected by the broad electronic filter used.

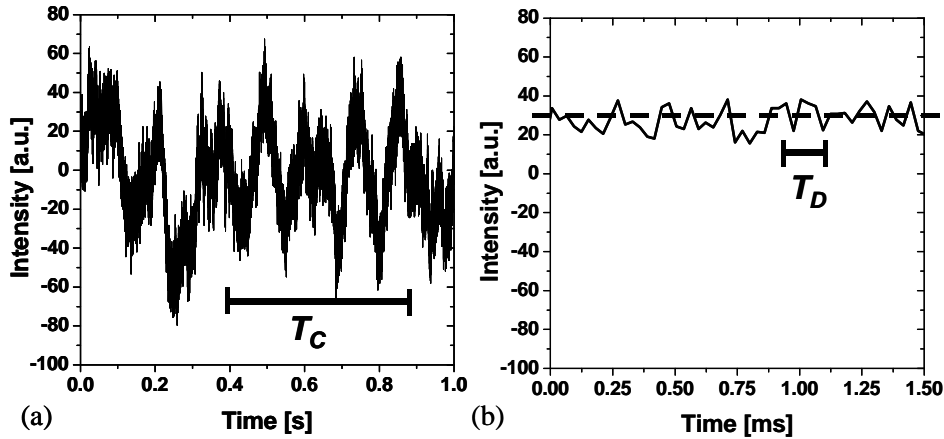


Fig. 9 Time scale of fluctuations caused by Brownian motion for an OCT signal containing mainly multiply scattered light: (a) large time scale, $T_C = 500 \text{ ms}$ is the interval between two scans; (b) $T_D \cong 150 \mu\text{s}$ is the inverse of the Doppler modulation frequency.

Thus, the random sample field corresponding to light undergoing multiple scattering can be considered as stationary (frozen) during measurement time. This means that the average magnitude of the random contribution of OCT signals only depends on the amount of multiply scattered light whose optical path matches the optical pathlength set by the reference mirror. It follows that multiple scattering is responsible for speckle formation but not for a loss of interference contrast. Good agreement between the theoretical and experimental speckle statistics (see Fig. 7) strongly supports that multiply scattered light interferes coherently.

Let us stress that we investigated a relatively unfavorable case regarding sample field stationarity. Indeed, due to the structure of most biological samples, Brownian motion would be lower than in our microbeads' solution. Moreover, our characteristic measurement time was much longer than in point scanning OCT. Thus, the stationarity of the sample field is true in most typical OCT applications.

Assessing of the stationarity of the sample field is of paramount importance for building a relevant model accounting for multiple scattering in OCT.

3.2.4 Model

Mathematical description

A comprehensive model for OCT requires a mathematical description of interfering fields in an amplitude-splitting interferometer where both ballistic and multiply scattered light are collected in the sample arm (see Fig. 10). For spatially coherent illumination, multiply scattered light creates a speckle pattern in the detection plane. In the previous section we showed that the backscattered sample field remains spatially coherent and stationary relative to measurement time. This allows a description of the interference process by a sum of stationary fields without further statistical averaging over measurement time. Thus, no quantitative measure of the average temporal behaviour by means, e.g., of an autocorrelation function, needs to be included in the model.

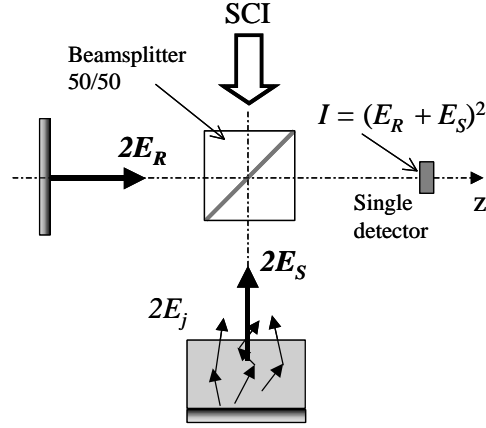


Fig. 10 Scheme of an amplitude splitting interferometer with broadband spatially coherent illumination (SCI). E_R and E_S are the reference and sample fields, respectively. E_j are the random components of E_S due to multiple scattering. Interference between E_R and E_S is considered on a single detector whose size matches a speckle.

Let us first calculate the intensity when the sample consists of a simple plane mirror. Consider a broadband source power spectrum $I(k)$ where $k = 2\pi/\lambda$ is the wavenumber. Assuming 100% reflectivity of the reference mirror and a reflectivity $r(k)$ for the sample mirror, the electrical fields E_R and E_S , reflected from the reference and from the sample arm, respectively, can be expressed for a given wavenumber as:

$$E_R = \text{Re}\left\{\sqrt{I(k)} \exp(j(kz - \omega t))\right\}, \quad (6)$$

$$E_S = \text{Re}\left\{r(k)\sqrt{I(k)} \exp(j(\mathbf{j}(k) - \omega t))\right\}, \quad (7)$$

where z is the reference mirror position and $\mathbf{j}(k)$ a phase argument depending on the position of the sample mirror.

When the waves recombine in the interferometer, the resulting intensity as a function of the wavenumber is:

$$I(k) = |E_R(k) + E_S(k)|^2 = I(k) \left[1 + r^2(k) + 2r(k) \text{Re}\left\{\exp(j(\mathbf{j}(k) - kz))\right\}\right] \quad (8)$$

The total intensity is obtained by integrating over the whole spectrum:

$$I = \int_0^\infty I(k) dk = \int_0^\infty I(k)(1 + r^2(k)) dk + 2\text{Re}\left\{\int_0^\infty I(k)r(k) \exp(j\mathbf{j}(k)) \exp(-jkz) dk\right\} \quad (9)$$

The first term, independent of z , is a constant intensity I_0 , while the second one corresponds to the Fourier transform of the power spectrum weighted by the sample spectral reflectivity. Therefore, Eq. 9 is equivalent to:

$$I = I_0 + 2\text{Re}\left\{\mathbb{F}\left[I(k)r(k) \exp(j\mathbf{j}(k))\right]\right\} \quad (10)$$

Let us now consider the more general case met in OCT where both ballistic and multiply scattered light contributions are present. Here, the sample field E_S is the sum of many contributions $E_j = \text{Re}\{u_j(k) \exp(jkL_j)\}$, corresponding each to a light ray having undergone a random path due to interactions with the scattering medium. The length L_j is the additional pathlength accumulated by a

multiply scattered photon (double path), relative to ballistic photons, and $u_j(k)$ is a field weighting coefficient proportional to the field magnitude. The total sample field is:

$$E_S(k) = \text{Re} \left\{ \sum_{j=1}^N E_j(k) \right\} = \text{Re} \left\{ \sqrt{I(k)} \sum_{j=1}^N u_j \exp(jkL_j) \right\} \quad (11)$$

Repeating for a scattering sample the calculation's steps that led to Eq. 10, and assuming the coefficients $u_j(k)$ to be independent of the wavelength (i.e. either no, or constant absorption over the spectrum), we obtain:

$$I = I_0 + 2\text{Re} \left\{ \mathbb{F} \left[I(k) \sum_{j=1}^N u_j \exp(jkL_j) \right] \right\}, \quad (12)$$

and, by virtue of the convolution theorem:

$$I = I_0 + 2\text{Re} \left\{ \mathbb{F}[I(k)] \otimes \sum_{j=1}^N u_j \mathbb{F}[\exp(jkL_j)] \right\} \quad (13)$$

According to the Wiener-Khinchine theorem $\mathbb{F}[I(k)]$ is the source autocorrelation function $g(z)$. Defining $I'(\Delta k) = I(k)$, where $\Delta k = k - k_0$, and $\lambda_0 = 2\pi/k_0$ is the central wavelength of the light source, $g(z)$ can be expressed as follows:

$$g(z) = \mathbb{F}[I(k)] = \mathbb{F}[I'(\Delta k)] = \exp(jk_0 z) \mathbb{F}[I'(k)] = \exp(jk_0 z) g_0(z) \quad (14)$$

where $g_0(z)$ is a slow varying function whose module is the envelope of $g(z)$. The second Fourier transform in Eq. 13 corresponds to a Delta function:

$$\mathbb{F}[\exp(jkL_j)] = \mathbf{d}(z - L_j) \quad (15)$$

After substitution of Eq. 14 and Eq. 15 into Eq. 13, one obtains:

$$I = I_0 + 2\text{Re} \left\{ \sum_{j=1}^N g_0(z) \exp(jk_0 z) \otimes u_j \mathbf{d}(z - L_j) \right\} \quad (16)$$

This expression reveals that the nature of the signal consists of a convolution of the autocorrelation function with randomly distributed Delta functions, located at random L_j positions. Exploiting the shift properties of a Delta function, Eq. 16 can be simplified by:

$$I = I_0 + 2\text{Re} \left\{ \exp(jk_0 z) \sum_{j=1}^N u_j g_0(z - L_j) \exp(-jk_0 L_j) \right\} \quad (17)$$

This equation provides the intensity detected as a function of the reference mirror position z . In OCT that relies on heterodyne detection, the reference mirror is scanned at constant velocity inducing a modulation of the signal at Doppler frequency. The effective OCT signal is the electrical current i obtained after bandpass filtering at the Doppler frequency and subsequent envelope demodulation. The first signal processing operation suppresses the constant term I_0 , while the second one removes the signal carrier $\exp(jk_0 z)$ and leaves a signal proportional to the module of the filtered signal. Such signal processing yields the following detected current:

$$i(z) \propto \left| \sum_{j=1}^N u_j g_0(z - L_j) \exp(-jk_0 L_j) \right| \quad (18)$$

This equation reveals that, despite multiple scattering, all the light detected in OCT interferes coherently within the coherence length around a position z imposed by the reference mirror. Moreover, the random sum leads to speckle formation and accounts for the signal randomness.

Statistical properties

Since we are interested to determine the mean contribution due to multiple scattering in OCT we will calculate the first order statistical properties (mean and variance) of the random signal detected. The summation in Eq. 18 corresponds to a sum of random phasors, which results in a single random phasor with complex amplitude $Q(z)$ and phase $\Phi(z)$. Thus, one can write:

$$\sum_{j=1}^N u_j g_0(z - L_j) \exp(-jk_0 L_j) = \sum_{j=1}^N \mathbf{a}_j(z) \exp(-j\mathbf{q}_j) = Q(z) \exp(j\Phi(z)) \quad (19)$$

Classical results from statistical optics derived by Goodman can be exploited. Goodman's calculations of the statistical distribution of a sum of random phasors for various cases rest on two important initial assumptions [20]:

- (i) The phases \mathbf{q}_j are uniformly distributed over $[0 - 2\pi]$.
- (ii) The amplitude \mathbf{a}_j and phase \mathbf{q}_j of the j th elementary phasor are statistically independent of each other, as well as of the amplitudes and phases of all elementary phasors.

These assumptions equally stand for our case. Indeed, assuming the paths L_j to be randomly distributed and the longest path $L_{jmax} \geq 2\pi/k_0$, the phase argument $\mathbf{q}_j = k_0 L_j$ is uniformly distributed between 0 and at least 2π , which fulfils the assumption (i). Note that, in all further considered practical cases, $L_{jmax} \gg 2\pi/k_0$.

The second assumption is also valid provided $\Delta\lambda \ll k_0$, which is usually the case in OCT. This implies that the module of $g_0(z)$ varies slowly with L_j relative to the function $\exp(-jk_0 L_j)$. Thus, $\mathbf{a}_j(z)$ is nearly insensitive to the argument \mathbf{q}_j , which means that these two variables are independent. In addition, the coefficients u_j bear no direct relationship to L_j .

Therefore, the results derived by Goodman can be directly applied to our case. The latter consists of the sum of a constant (deterministic) phasor with amplitude S and a random phasor, corresponding to the ballistic and multiply scattered photons contribution, respectively. The ballistic contribution corresponds to photons directly reflected from the sample mirror. Expressing S in the random sum of Eq. 19 yields:

$$\begin{aligned} S(z) + Q(z) \exp(-j\Phi(z)) &= \\ &= u_0 g_0(z - L_0) \exp(-jk_0 L_0) + \sum_{j=1}^N u_j g_0(z - L_j) \exp(-jk_0 L_j) \end{aligned} \quad (20)$$

where L_0 is the sample mirror position. Adopting the convention $L_0 = 0$, the additional pathlengths are defined relative to the sample mirror interface leading to: $S(z) = u_0 g_0(z)$.

The phasor amplitude described by Eq. 20 obeys a Rician probability density function, whose mean is given by [20]

$$\overline{A(z)} = \sqrt{\frac{\mathbf{p}}{2}} \mathbf{s}(z) \exp\left(-\frac{\mathbf{b}^2(z)}{4}\right) \left[\left(1 + \frac{\mathbf{b}^2(z)}{2}\right) I_0\left(\frac{\mathbf{b}^2(z)}{4}\right) + \frac{\mathbf{b}^2(z)}{2} I_1\left(\frac{\mathbf{b}^2(z)}{4}\right) \right], \quad (21)$$

where,

$$\mathbf{b}(z) = \frac{S(z)}{\mathbf{s}(z)} = \frac{u_0 g_0(z)}{\mathbf{s}(z)} \quad (22)$$

and where, $\mathbf{s}(z)$ is the distribution's standard deviation. I_0 and I_1 are modified Bessel functions of the first kind, order zero and one, respectively.

$A(z)$ is directly proportional to the mean value of $i(z)$ in Eq. 18, i.e to the mean amplitude of the random OCT signal. Such mean signal could be roughly measured in our preliminary experiment by averaging 25 demodulated signals (see Fig. 6).

Calculation of $A(z)$ requires knowing the variance $\mathbf{s}^2(z)$ of our distribution, which is [20]:

$$\mathbf{s}^2(z) = \frac{\overline{\mathbf{a}_j^2(z)}}{2} \quad (23)$$

Applying this result to our specific case yields:

$$\mathbf{s}^2(z) = \frac{\overline{u_j^2 (g_0(z-L_j))^2}}{2} = \frac{1}{2N} \sum_{j=1}^N U_j (g_0(z-L_j))^2 \quad (24)$$

leading to,

$$\mathbf{s}(z) = \sqrt{\frac{1}{2N} U_j \otimes g_0^2(z)}, \quad (25)$$

where $U_j = (u_j)^2$ is the intensity coefficient corresponding to light travelling a pathlength L_j .

Thus, the mean signal detected in OCT can be calculated by combining Eq. 21/22 and 25. However, to perform this calculation, one still needs to know the coefficients U_j . The latter are proportional to the intensity $I(L_j)$ measured in the sample at depth $L_j/2$ from the sample mirror. $I(L_j)$ corresponds to the spatio-temporal distribution of the intensity i.e. of photons. Calculation of such a distribution lends itself very well to a Monte Carlo simulation [25,27]. Therefore, our model combined with a Monte Carlo simulation, allows one to calculate OCT signals in accounting both for ballistic and multiply scattered light.

Monte Carlo simulation

Practical integration of Monte Carlo simulation's results into our model requires the following analysis. A Monte Carlo simulation provides a photon distribution whose density is proportional to the mean intensity I_v in a v th sampling volume determined by the detector size and temporal distribution ($\Delta t \propto \Delta L$ range). The resolution determines an average path of length L_v of all pathlengths L_j falling into the v th sampling volume. To express Eq. 25 as a function of I_v , the sum operation is distributed into V sampling volumes, each containing $m_{v+1} - m_v$ of the N elements. This yields:

$$\mathbf{s}^2(z) = \frac{1}{2N} \sum_{j=1}^N U_j (g_0(z-L_j))^2 = \frac{1}{2} \sum_{v=1}^V \frac{1}{m_{v+1} - m_v} \sum_{j=m_v+1}^{m_{v+1}} U_j (g_0(z-L_j))^2 = \frac{1}{2} \sum_{v=1}^V I_v (g_0(z-L_v))^2 \quad (26)$$

leading to,

$$\mathbf{s}(z) = \sqrt{\frac{1}{2} I_v \otimes g_0^2(z)} \quad (27)$$

Similarly, expressing the coefficient u_0 in $\mathbf{b}(z)$ (Eq. 22) as a function of I_v , yields:

$$u_0 = \sqrt{U_0} = \sqrt{I_B}, \quad (28)$$

where I_B is the intensity of the ballistic light, determined either theoretically (Lambert-Beer's law) or by the Monte Carlo simulation.

The important features of the Monte Carlo simulation used further in our study on multiple scattering are briefly described in section 3.2.5.

Modifications for a biological sample

So far, due to the structure of our sample, we were concerned with the distribution resulting from a deterministic plus a random phasor sum. However, in most practical cases of interest we are concerned with a purely random phasor sum. Indeed, due to the sub micrometric complex structure of biological interfaces made of densely packed scatterers [36], even single scattered light (i.e. ballistic light) gives rise to speckle formation. According to the terminology introduced by Schmitt, ballistic light is responsible for "signal carrying speckles" whereas cross-talk light is responsible for "signal degrading speckles" [37]. This means that all photons, including ballistic ones (single scattering), reach the detector with random phase delays.

The application of our model becomes very straightforward in this case. Indeed, Eq. 21 simplifies greatly since the mean $A'(z)$ of a purely random distribution is directly proportional to the standard deviation $\sigma(z)$ [20]

$$\overline{A'(z)} = \sqrt{\frac{\mathbf{p}}{2}} \mathbf{s}(z) = \sqrt{\frac{\mathbf{p}}{4} I_v \otimes g_0^2(z)} \quad (29)$$

Therefore, without constant deterministic phasor, Eq. 29 can be directly applied to Monte Carlo results. Even in presence of a strong deterministic phasor, Eq. 29 may lead to an excellent approximation. Indeed, with the examples presented in section 3.3, very similar results could be obtained in nearly all cases, when using either Eq. 29 or the full treatment to account for the deterministic phasor.

Thus, our model greatly simplifies for the practical case of a biological sample.

3.2.5 Preliminary results and analyses

To illustrate its practical relevance, our model is applied to the experiment reported in section 3.2.2.

First we will describe the important features of our Monte Carlo simulation. The algorithm used in the latter is described elsewhere e.g. by Jacques [38]. We used a Mie scattering distribution at each particle interaction. The sampling area (conjugated to a detector) from which photons virtually originate is determined, according to the rules of geometrical optics, by the positions and the angles of the photons falling within the objective NA, while the accumulated photon pathlength delays define their positions along the depth axis. The dimension of the sampling area is delimited by the imaging lateral resolution and the v th sampling volume is then determined by the axial sampling resolution, which amounts to $1\mu\text{m}$ in our simulations.

Introducing the parameters corresponding to the experiment described in section 3.2.2, into our Monte Carlo simulation yields the result shown in Fig. 11a.

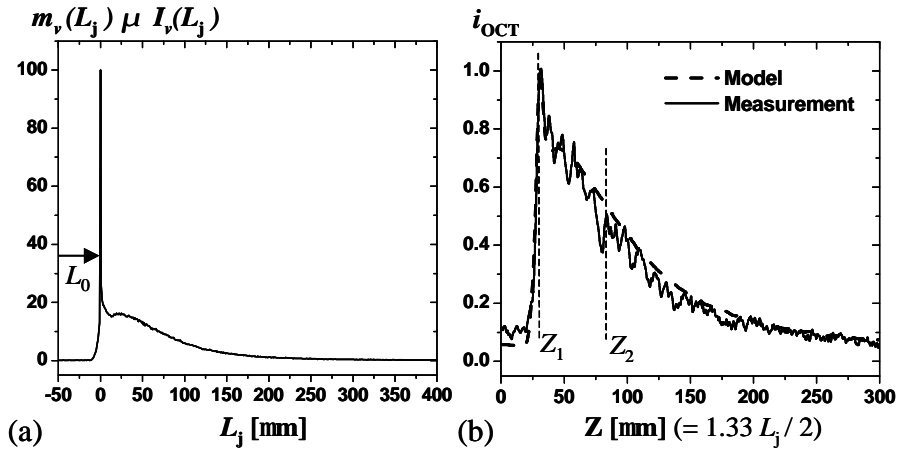


Fig. 11 (a) Photon distribution as a function of the additional pathlength L_j of multiply scattered relative to ballistic photons (L_0), obtained with Monte Carlo simulation, and (b) the corresponding normalized OCT signal obtained with our model (dashed curve) compared to experimental results (solid curve). The plots are shown against the actual reference mirror position. Z_1 is the sample mirror position and Z_2 is $60 \mu\text{m}$ away from Z_1 . Speckle statistics is calculated at $Z_{1/2}$.

The intensity distribution $I_v(L_j)$, proportional to the number of photons m in a sampling v , volume must be treated as follows. First, the ballistic component, responsible in our case for the major part of the high peak located at L_0 (sample mirror position), is removed from the distribution so that $\mathcal{S}(z)$ can be calculated from Eq. 25. The mean OCT signal can then be derived from Eq. 21.

Since L_j represents the geometrical pathlength, the corresponding length scale was multiplied by water refractive index (1.33) and divided by 2, so as to account for the optical pathlength and reference mirror displacement, respectively. To account for scaling factors the width of g_0 was divided by 1.33.

Our result, shown in Fig. 11b against the reference mirror position z , is in good agreement with the corresponding experimental curve of Fig. 6 obtained by averaging 25 demodulated signals.

Comparison of the statistical distributions measured in section 3.2.2 (see Fig. 7) to the corresponding theoretical predictions further confirms the validity of our model. The speckle contrast was measured at Z_1 (mirror position), where the mirror creates a large constant phasor S , and at Z_2 , separated from Z_1 by about 10 times the width of g_0 , a distance at which multiply scattered light is largely dominant ($S \cong 0$). When $S \cong 0$, the Rician probability density function becomes a Rayleigh probability density function, for which the ratio $\sigma/A \cong 0.52$.

This is in perfect agreement with the measurements performed in section 3.2.2, which lead to a distribution close to a Rayleigh distribution and to a contrast $C_2 \cong 0.5$. For large values of S , the Rician probability density function becomes a Gaussian probability density function with a mean approximately equal to S . The ballistic light contribution provided by our model was two times larger than the mean multiply scattered light contribution. The standard deviation of the latter being 0.52 times the mean, the theoretical contrast ratio ranges around 0.25, close to the experimental value $C_1 \cong 0.22$ obtained in section 3.2.2.

These preliminary results reveal the relevance of our model, that will be further confirmed by a wider study presented in section 3.3.

3.2.6 Discussion

We will essentially discuss models based on the extended Huygens-Fresnel principle while other models of OCT based on Monte Carlo simulation will be briefly commented at the end of this section.

As presented in the introduction, our model differs from other models based on the extended Huygens-Fresnel principle because they rest on two fundamentally different hypotheses. The latter

models are based on the assumption that the sample field is generally partially coherent due to multiple scattering. They make use of the mutual coherence function, which characterizes the degree of spatial coherence [23,31,32]. However, the definition of the degree of spatial coherence makes sense only if the integration time is long enough, i.e. if statistical averaging over a sufficiently large ensemble of all possible different phasors takes place [35,39]. Therefore, models based on the extended Huygens-Fresnel principle implicitly rely on statistical averaging, i.e. it is implicitly assumed that the sample's microscopic structure changes sufficiently fast during the measurement time (see section 3.2.3). We believe that the extended Huygens-Fresnel principle should be applied only when this condition is met.

To show the importance of this initial assumption of stationarity we will compare equivalent measurements with and without statistical averaging. To obtain statistical averaging in our experiment, the ergodicity of the Brownian motion (the same statistics prevails at any time) can be exploited by averaging over an ensemble of events separated in time. Thus, measurements corresponding to a non-stationary sample field can be obtained by averaging a series of measurements, provided that the phase information is preserved. This amounts to perform a slightly different signal processing, which consists in averaging M measurements prior to envelope reconstruction. From the mathematical point of view this means that, when moving from Eq. 17 to Eq. 18, the signal carrier term $\exp(jk_0z)$ is not suppressed and the real part of the filtered signal instead of its module is detected. Thus the detected current becomes:

$$i(z) \propto \frac{1}{M} \sum_1^M \left[\operatorname{Re} \left\{ \exp(jk_0z) \sum_{j=1}^N u_{jM} g_0(z - L_{jM}) \exp(-jk_0L_{jM}) \right\} \right] \quad (30)$$

This signal processing has a totally different physical meaning than the one described by Eq. 18. Averaging M measurements, containing a cosine signal carrier with random phase, corresponds to averaging many cosines with random arguments. This results in a null signal when the phase fluctuation is uniformly distributed over 2π and the statistical averaging complete. Only the ballistic component is not cancelled since all corresponding phases are deterministic and equal.

We repeated the preliminary experiment of section 3.2.2 and used the two different signal processings. Here the source was replaced by a superluminescent diode with coherence length of 34 μm and a piezoelectric translator was used instead of our voice-coil scanner (see 3.3.2) so as to guarantee an accurate enough phase relationship between different measurements.

The measurements obtained with the two different signal processings are shown in Fig. 12.

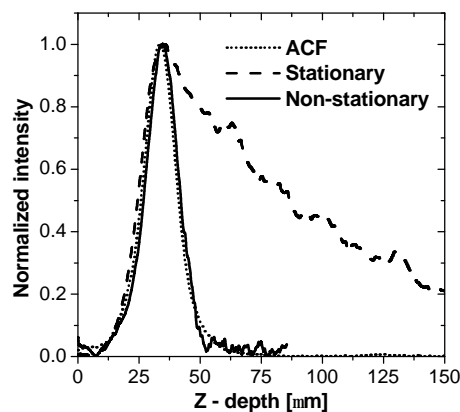


Fig. 12 Correlogram envelopes obtained in wide-field OCT for a mirror covered with scattering solution (8 OD, $g = 0.85$) for different signal processing: (i) average of 50 demodulated signals with uncorrelated phase corresponding to a stationary sample field (ii) demodulated signal obtained by averaging 500 phase uncorrelated signals corresponding to a non-stationary sample field. The envelope of the source autocorrelation function (ACF) is provided as reference. All correlograms are normalized and plotted against the reference mirror position.

When applying the signal processing corresponding to a stationary sample field (Eq. 18), a significant amount of multiply scattered light is measured, as shown for the average of $N = 50$ demodulated signals with uncorrelated phase (dashed curve). On the contrary, when using the signal processing corresponding to a non-stationary sample field (Eq. 30), multiply scattered light is totally washed out, provided enough time is allowed for statistical averaging as shown for the average of $M = 500$ phase correlated signals (solid curve).

This result strikingly illustrates the considerable importance of statistical averaging, i.e. the choice of different initial assumptions on which the models are based. Our model, which assumes sample field stationarity, is in very good agreement with a wide range of experimental data obtained in a study of wide-field OCT (see 3.3). We would like to emphasize that our initial assumptions, shown here for the specific case of wide-field OCT, would be even more valid in point-scanning OCT where the acquisition time per probe volume is generally much shorter. Moreover, for most biological samples the effect of Brownian motion, due to their structure, would be lesser than for our liquid scattering solution.

In addition to putting into question the applicability to OCT of models based on the extended Huygens-Fresnel principle, the results presented here above add more weight to other models based on Monte Carlo simulations. Indeed, these models, believed to describe a “worst case scenario” since they implicitly assume that all multiply scattered light within the coherence length interferes [28-30], might provide a more accurate description than expected.

Finally, we would like to point out a major difference between our model and a recently published one based on a Monte Carlo simulation which takes into account the effect of multiple scattering [40]. In the latter model the phase information is recorded for each photon - represented by plane wavelet - depending on interaction within the scattering medium. Simulation of a practical case yields a sum of randomly delayed wavelets and in turn speckle formation. In our model, random events in the scattering medium are modeled as an *a priori* known phenomenon from which the mean and variance can be obtained. This avoids complicated and lengthy Monte Carlo simulations recording the phase for each photon. Such complex model would bring useful information for a random wavelets phase shift in a range below 2π , while a random phase excursion of at least 2π is a key assumption of our model (see 4.2).

Note also that, although in principle only the mean signal is of interest, the speckled nature of signals obtained for one scan could be easily accounted for with our model by weighting the mean intensity with random numbers provided by the known speckle statistics. According to our calculations (e.g. Eq.11), the average length - equivalent to the mean speckle axial length - that would have to be weighted by statistical factors, approximately corresponds to the width of g_0 , i.e. to the source coherence length.

3.2.7 Conclusions

To the contrary of the widespread belief that a relevant OCT model should account for partially correlated interfering fields, we have explained why multiple scattering does actually not induce a loss of spatial coherence of the sample field and shown that the latter is stationary relative to measurement time. This means that the reference and sample fields are fully correlated i.e. interfere with the maximum contrast. Multiple scattering is responsible for speckle formation but not for a loss of interference contrast.

Based on this important result, we have developed a new comprehensive model of OCT where the signal is modeled as a sum of stationary random phasors and treated as a statistical signal. The mean of this signal can be calculated thanks to classical results of statistical optics and to a Monte Carlo simulation. The latter, that is necessary to calculate the raw spatio-temporal distribution of light, makes our model semi-analytical. It is the prize one has to pay for accessing ranges where the diffusion approximation is not verified. Though this removes the elegance of a fully analytical model, it offers the advantage of a high versatility. Indeed, unlike fully analytical models, it is neither restricted to strongly simplified media nor limited by initial assumptions, such as for instance by the diffusion approximation or by the small angle approximation. Moreover, the application of our model is simplified for samples with complex sub-micrometric structures such as most biological samples

(see section 3.2.4). Unlike other models, ours accounts for the source autocorrelation function. Theoretical predictions were in good agreement for a depth scan measurement on a sample consisting of a mirror covered with a microbeads' solution.

Our results put in question the applicability of OCT models based on the extended Huygens-Fresnel principle, which involve spatial coherence effects. These models rest on the assumption of partially coherent interfering fields, a hypothesis not met in most practical cases in OCT as shown here above (see section 3.2.3 and 3.2.6). Thus, we believe that care should be taken when applying models based on the extended Huygens-Fresnel principle to OCT. In addition, our investigation adds more weight to OCT models based on Monte Carlo simulations. Indeed, the latter models, believed to describe a "worst case scenario" since they implicitly assume that all multiply scattered light within the coherence length interferes, may well provide a more accurate description than expected.

We do hope that our study and the model will help to fully appreciate the role of multiple scattering in OCT and stimulate the research in this field.

In section 3.3, our model is tested against a whole range of experimental data in a comprehensive study of optical cross-talk in wide-field OCT.

3.3 Experimental and theoretical investigation of cross-talk in wide-field OCT

3.3.1 Introduction

Multiple scattering affects the performance of most optical imaging modalities devoted to measurements in turbid samples. In section 3.2, we developed a model which accounts for multiple scattering in optical coherence tomography (OCT) [41]. For the specific case investigated we obtained a very good agreement between theoretical and experimental results. For further validation, our model should be tested on a wider range of different experimental cases. Wide-field OCT offers an ideal case to study since a considerable amount of multiply scattered light is generated. The latter is responsible for optical cross-talk, whose effects have not been investigated yet.

Compared to conventional OCT, which relies on point-by-point scanning, wide-field OCT has the advantage of fast three-dimensional image acquisition and reduced system complexity [42,43]. However, with wide-field illumination and parallel detection, the amount of multiply scattered light collected by each detector is considerably higher than that collected with focused illumination and single channel detection like in point scanning OCT. Depending on the nature of the illumination, multiply scattered light can result in a strong cross-talk generated noise between parallel detection channels. Wide-field OCT can be realized either with spatially coherent illumination [44,45] or spatially incoherent illumination [33,43]. When spatially incoherent illumination is used, for instance with a thermal light source, coherent cross-talk can be completely suppressed as shown in section 4.2. On the contrary, spatially coherent illumination can generate a large amount of coherent cross-talk degrading the image quality [33]. The major interest of spatially coherent illumination in wide-field OCT resides in the possibility to use powerful pulsed lasers [45] allowing a higher sensitivity or acquisition speed than with thermal light sources, which are limited by their low brightness [46]. However, since the brightness per pixel, as provided by a spatially coherent source, decreases with the number of pixels, whereas the brightness of a thermal light source depends only on the source temperature, this advantage prevails if the number of detectors is not too large. A pulsed laser source in the Watt range should yield a substantial gain in brightness for an array of 250 by 250 pixels.

The potential advantage of higher sensitivity offered by a powerful spatially coherent illumination can be easily lost if cross-talk generated noise dominates. Presently, little is known on the importance of cross-talk effects in wide-field OCT with spatially coherent illumination, i.e. on the rejection capabilities of multiply scattered light when relying on temporal coherence gating alone.

In section 3.3, we investigate the dependence of cross-talk generated noise on important system design parameters, as well as on sample properties. In a comprehensive study, we will compare theoretical results obtained with our model and measurements on samples consisting of a reflective edge break embedded in microbeads' solutions. The interest of this study is twofold. It allows first to test the validity of our theoretical model, and second to determine the importance of cross-talk effects in wide-field OCT. More generally, it provides a deeper understanding of the role played by multiple scattering in coherence gating detection methods.

3.3.2 Method

Set-up

The experimental set-up used for wide-field OCT is illustrated in Fig. 13. A broadband spatially coherent source is coupled to a single mode fiber launching light into a free space Michelson interferometer. Light is equally divided by a non-polarising beamsplitter into a reference and a sample arm containing identical microscope objectives with magnification $\times 10$ (L_3 and L_3') and with a numerical aperture (NA) of 0.25. Lenses $L_1/L_2/L_3$ are positioned so as to obtain a collimated beam illuminating the sample with a $420 \mu\text{m}$ Gaussian intensity profile measured at full width at half

maximum (FWHM). The sample is imaged with a magnification $\times 30$ by lenses L_3/L_4 , which form a microscope as illustrated in the sample arm in Fig. 13.

Unless otherwise specified, the source is a superluminescent diode (SLD) whose spectrum is centered around 810 nm with 17 nm bandwidth at FWHM corresponding to a coherence length (l_c) of 34 μm at FWHM. The SLD (Superlum 381-HP2) delivers a power of around 1 mW onto the sample. In some specific cases, the SLD is replaced by a mode-locked femtosecond Ti:Sapphire laser whose spectrum is centered around 800 nm with 70 nm bandwidth at FWHM corresponding to a coherence length (l_c) of 15 μm at FWHM.

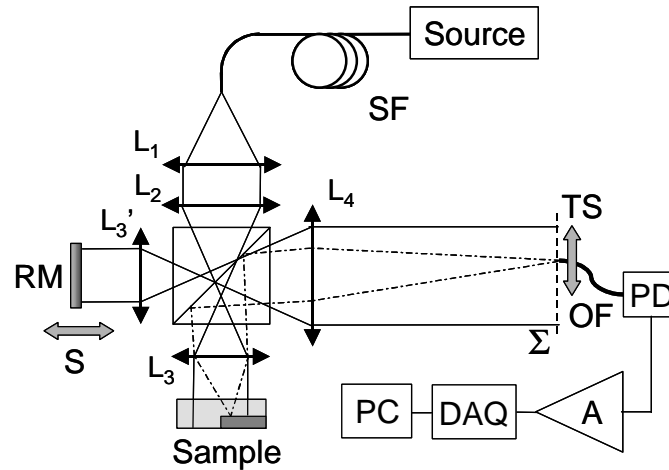


Fig. 13 Scheme of a wide-field OCT set-up: Source is either a SLD or a pulsed Ti:Sapphire laser; single mode fiber (SF); reference mirror (RM); voice coil scanner (S); achromatic lenses ($L_1/L_2/L_4$); microscope objective $\times 10$, N.A. = 0.25 (L_3/L_3'); translating stage (TS); 50 μm core optical fiber (OF) photodiode (PD). Details of the signal processing are given in the text.

Interference between light backscattered from the sample and the reference mirror (RM) can occur only when the optical path length difference lies within the source coherence length. RM is mounted on a voice coil scanner (S) and scanned axially at constant velocity over a depth of 750 μm at a frequency of 2 Hz with a 90% duty cycle. The resulting 6.7 kHz Doppler frequency modulation permits heterodyne detection. Without dynamic focusing [47], the useful scan range is in principle restricted to the Rayleigh range $l_R \cong 13 \mu\text{m}$ in water, as defined by the objective lens L_3 .

To gain flexibility and avoid potential electronic cross-talk, detection is not made in parallel with a detector array. In this study, the detection is made with a 50 μm core optical fiber (OF) delivering light to a silicon photodiode (PD) moved in 120 μm steps across the image plane Σ with a motorized translation stage (TS). Each step corresponds to 4 μm large pixels on the sample side. The resolution on the sample side, which is around 2 μm , is slightly larger than the fiber optic core size after magnification with L_4 .

The photocurrent produced by the photodiode is amplified and high-pass filtered by a low noise pre-amplifier (A). The signal is then digitized with a 12 bit A/D converter on a data acquisition card (DAQ) and processed in a PC. With the SLD, the signal processing consists of 0.6 kHz bandpass filtering around the 6.7 kHz Doppler frequency with a second order Chebyshev filter, followed by envelope reconstruction with the Hilbert transform. With the pulsed laser source the bandwidth of the bandpass filter is increased to 1.4 kHz. The DAQ is triggered by the voice coil scanner at each new depth scan. An experimental sensitivity of -75 dB is obtained with the SLD when averaging 25 demodulated signals.

A confocal configuration with properties equivalent to point scanning OCT can be obtained by simply removing lens L_2 . The monomode fiber is then imaged onto the sample providing a confocal spot illumination. The confocal configuration leads to an experimental sensitivity of -96 dB with the SLD when averaging 25 demodulated signals.

Sample

The sample consists of a cleaved GaAs edge coated with gold and embedded in a scattering solution maintained in a cell. The latter is limited by a 150 μm thick cover glass on the objective side. The distance Δz between the reflecting edge and the cover glass can be accurately varied. The solution is made of single size polystyrene microspheres homogeneously distributed in de-ionized water. The absorption being negligible at the wavelengths used, the solution can be considered as purely scattering. Independent of the type of solution used (microbeads' size), the concentration is adjusted separately to a scattering coefficient $\mu_s = 6.2 \text{ mm}^{-1}$ using the collimated transmission method given in [13]. The cell inner thickness Δz determines the number of scattering mean free paths (mfp) i.e. the sample optical density (OD) defined as $2 \Delta z \mu_s$ when accounting for double optical path. The source wavelength ($\lambda \cong 800 \text{ nm}$ in air), as well as the size and refractive index ($n=1.59$) of the microbeads suspended in water, yield an anisotropy parameter g defined as the average cosine of the scattering angles, that can be calculated with the Mie theory.

In our “standard conditions” the sample thickness is $\Delta z = 650 \mu\text{m}$ yielding 8 mfp (OD = 8), with $g \cong 0.85$. Tests revealed that, despite sedimentation, the sample optical properties remain stable during at least 10 minutes after ultrasound shaking.

The sample axial position is adjusted to bring the reflecting edge into focus in the detection plane Σ with the cell containing water. Depending on the experiment, the sample is moved laterally so as to present either a full mirror interface or half a mirror with the edge break positioned on the optical axis. For the rest of section 3.3, these positions are designated “full mirror sample” and “half mirror sample”, respectively.

3.3.3 Cross-talk measurements

Origin

The purpose of this section is to more precisely define optical cross-talk in wide-field OCT. Fig. 14 schematically represents the effect of multiple scattering within the sample, here a backscattering object (BO) embedded in a homogeneous scattering medium, and helps to discuss the origin of optical cross-talk.

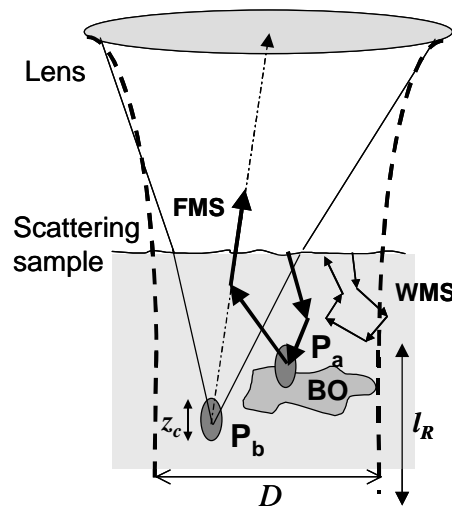


Fig. 14 Scheme of the interferometer sample arm showing optical cross-talk in wide-field OCT: wide-field diameter (D), ideal probe volume (P_b), virtual probe volume (P_a), backscattering object (BO), Rayleigh range (l_R), axial resolution (z_c), forward multiple scattering (FMS), wide-angle multiple scattering (WMS).

The overall scattering volume is determined by the wide-field illumination diameter D and by the sample thickness. The lateral and depth resolution (Rayleigh range l_R) of the optical system define sampling volumes within the scattering volume. Each sampling volume is conjugated to one detector of the array. The axial resolution set by the source coherence length l_c allows dividing each sampling volume into probe volumes with axial dimension $z_c = l_c / 2n$, where n is the sample refractive index. With dynamical focusing [47], probe volumes can be defined within the whole scattering volume.

Ideally, only light originating from a given probe volume P_x should be detected by its conjugated detector C_x at a depth Z defined by the reference mirror position. Propagation of multiply scattered light across the whole scattering volume prevents this ideal one to one correspondence. Optical cross-talk on a detector can be defined as all light contributions originating from all other probe volumes than the one conjugated to the detector. Fig. 14 illustrates how forward multiply scattered light (FMS) originating from the probe volume P_a can be detected by the detector C_b conjugated to probe volume P_b despite short temporal coherence gating.

Our experiment is slightly different from the general case investigated above. Indeed, there is no dynamic focusing and the Rayleigh range is close to the axial resolution. Thus, we investigate the spatio-temporal distribution of multiply scattered light for sampling volumes in the image focal plane. Moreover, since the potential cross-talk due to wide-angle multiple scattering (WMS in Fig. 14) represents a negligible contribution in our experiment, we deal with the cross-talk essentially due to forward multiple scattering (FMS) for a reflecting interface (full mirror or edge) in the image focal plane.

We show experimentally hereafter that, in our experimental set-up and conditions, multiply scattered light causing cross-talk is mainly due to the wide-field configuration. Plots in Fig. 15 are the correlogram envelopes measured with the full mirror sample covered with either water or standard scattering solution, as obtained in confocal configuration (corresponding to point-scanning) with the pulsed laser source.

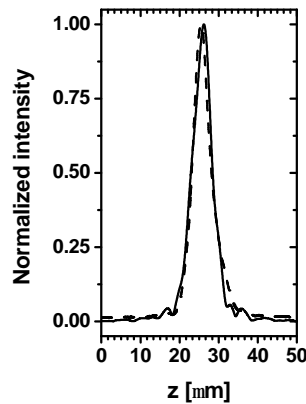


Fig. 15 Envelope of the source autocorrelation function measured with the mode-locked femtosecond Ti:Sapphire laser: (a) in water with the wide-field configuration (solid curve) and; (b) in scattering solution (8 OD, $g = 0.85$) with the confocal configuration (dashed curve).

The two normalized plots being nearly identical reveal that cross-talk contribution is negligible. This would be the case in all experiments presented here below had the confocal instead of the wide-field configuration been used. This means that multiply scattered light contributions measured in our study are almost entirely due to the wide-field configuration, and that we are directly measuring cross-talk inherent to wide-field OCT.

Experimental conditions

In this section, we describe the experimental conditions and provide explanations relative to the presentation of results.

Consider first the following measurement performed with our wide-field OCT system using the mode-locked femtosecond Ti:Sapphire laser. The 3D plots shown in Fig. 16 are the cross-section

images of the half mirror sample - with the normalized intensity represented along the vertical axis - obtained in water and in the scattering solution (8 OD, $g = 0.93$), respectively. The plots correspond to the average cross-talk signal obtained with 25 demodulated signals.

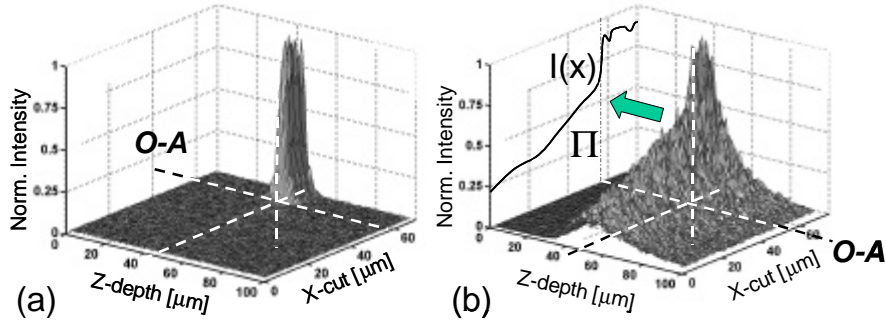


Fig. 16 Cross-section wide-field OCT image of a reflecting edge with break on the optical axis (O-A): (a) in water; (b) in scattering solution (8 OD, $g = 0.93$), $I(x)$: projection of the maximum intensity profile.

In water, the half mirror interface is clearly resolved in both dimensions, while with the scattering solution cross-talk spreads into the whole sample degrading both axial and lateral resolutions.

Practically, a quantitative comparison between theory and experiment in a 3D representation is difficult. Therefore, cross-talk effects are investigated independently for the lateral and the axial dimensions, with the half and full mirror samples, respectively.

The lateral cross-talk extent is represented by the maximum intensity profile $I(x)$ corresponding to a projection of the 3D intensity plot along the optical axis (O-A) onto plane Π , as shown in Fig. 16b. The edge break is always located on the optical axis. To reduce image acquisition time, measurements cover $325 \mu\text{m}$, from which $75 \mu\text{m}$ are on the edge side and $250 \mu\text{m}$ on the other side. $I(x)$ plots are obtained by averaging 25 demodulated signals. To allow comparison with the ideal case of full cross-talk rejection, the edge intensity profile measured in water is illustrated in all graphs.

The axial cross-talk extent is measured along the optical axis with the full mirror sample. The plots are normalized and shown as a function of the reference mirror displacement. Unless otherwise specified, the axial plots correspond to the average of 50 demodulated signals. To allow comparison with the ideal case of full cross-talk rejection, the envelope of the autocorrelation function is illustrated in all graphs.

Measurements are represented with corresponding theoretical results obtained with the model developed in section 3.2. Comparison of theoretical and experimental results for the lateral dimension is less straightforward than for the axial dimension where all curves are normalized. Normalizing to the maximum intensity would not be reliable since the signals measured on the edge side are very noisy (see results in section 3.2.4) due to rippled illumination profile, coating damage, and possibly microbead aggregates sticking to the edge surface. Therefore, experimental data are adjusted with a multiplicative factor K_f so as to obtain a least square fit difference with the theoretical curves. The adjustment is performed on data measured on the opposite side of the edge.

When the model is applied to the lateral dimension, care must be taken to include the Gaussian intensity illumination profile $I_G(x)$ in the model. The Monte Carlo simulation used in the model is briefly described in section 3.2.5.

3.3.4 Results and discussion

Here we investigate the dependence of cross-talk signals (i) on important design parameters of the optical system, and (ii) on the main properties of the sample. Optical system parameters include: the wide-field diameter, the objective NA and the source coherence length. Sample properties include: the optical density (OD) and the anisotropy (g) of the scattering solution.

Experimental conditions are varied around the “standard case” corresponding to the set-up described in the method ($D = 420 \mu\text{m}$, $\text{NA} = 0.25$) with the SLD source ($l_c = 34 \mu\text{m}$) and the sample with the standard scattering solution ($\text{OD} = 8$, $g = 0.85$). In each case, theoretical and experimental results are plotted on the same graph. Theoretical results are discussed at the end of section 3.3.4.

Dependence on system design parameters

Cross-talk dependence on wide-field diameter D is investigated with the standard scattering solution. Experimental and theoretical results, corresponding to 3 different wide-field diameters, are shown in Fig 17a and 17b for the full and the half mirror sample, respectively. Experimentally, the different wide-field diameters were obtained by changing the focal length and position of lenses L_1 and L_2 . The diameter D of the Gaussian illumination beam is defined at FWHM. In our standard conditions $D = 420 \mu\text{m}$ with focal lengths $f_{L1} = 25 \text{ mm}$ and $f_{L2} = 100 \text{ mm}$, $D = 210 \mu\text{m}$ is obtained with focal lengths $f_{L1} = 25 \text{ mm}$ and $f_{L2} = 200 \text{ mm}$, and $D = 85 \mu\text{m}$ is obtained with focal lengths $f_{L1} = 10 \text{ mm}$ and $f_{L2} = 200 \text{ mm}$.

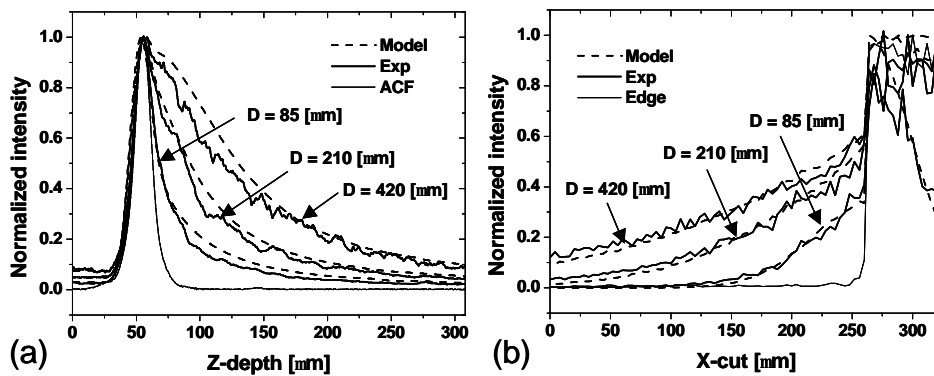


Fig. 17 Experimental (Exp) and theoretical (Model) results obtained in wide-field OCT for various wide-field diameters (D) with $\text{OD} = 8$, $g = 0.85$, $\text{NA} = 0.25$: (a) Correlogram envelopes for the full mirror sample and envelope of the source autocorrelation function (ACF) for reference; (b) Projection of the maximum intensity profile obtained with the half mirror sample and edge intensity profile in water for reference (Edge).

The results reveal that cross-talk generated noise directly depends on the wide-field diameter. The larger the wide-field, the higher the cross-talk generated noise and the lower the axial and lateral resolution. However, cross-talk affects the lateral resolution in lowering the contrast rather than blurring the edge break. Note that the smallest possible illumination diameter corresponds to point scanning OCT which, in our case, is devoid of cross-talk (Fig. 17).

Cross-talk dependence on the objective numerical aperture (NA) is investigated with the standard scattering solution. Experimental and theoretical results obtained with 3 different numerical apertures are shown in Fig. 18 for the full mirror sample only. The experiments with the half mirror sample were not carried out due to the vignetting aberrations. Since modifying the aperture of the objective lens L_3 is impractical, a diaphragm was placed at lens L_4 so as to set the effective collection aperture of L_3 . The position of the diaphragm was causing significant vignetting. The objective lens has a NA of 0.25. The diaphragm aperture was adjusted to additionally obtain $\text{NA} = 0.15$ and $\text{NA} = 0.05$. The results clearly show that cross-talk effects diminish with the NA. Such dependence was expected since a lower NA limits the collection of multiply scattered light.

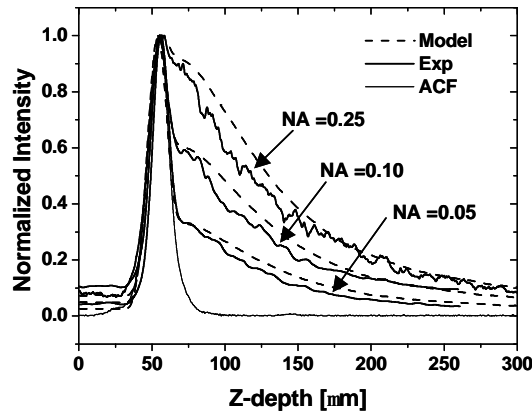


Fig. 18 Experimental (Exp) and theoretical (Model) results obtained in wide-field OCT with the full mirror sample for various numerical apertures (NA) with $OD = 8$, $g = 0.85$, $D = 420 \mu\text{m}$. Envelope of the source autocorrelation function (ACF) for reference.

Cross-talk dependence on the source coherence length is investigated with the standard scattering solution. With the SLD ($l_c = 34 \mu\text{m}$) and the mode-locked femtosecond Ti:Sapphire laser ($l_c = 15 \mu\text{m}$), the source coherence length (l_c) could be varied by a factor of approximately two. Experimental and theoretical results are shown in Fig 19a and 19b for the full and the half mirror sample, respectively. The slightly lower cross-talk signals measured with the pulsed laser source reflect well the superior rejection capabilities of multiply scattered light achieved with a shorter coherence length.

The correlogram envelope is noisier for the pulsed laser source than for the SLD. The reason for that is the lower number of signals used for averaging (25 with the pulsed laser instead of 50 for the SLD), as well as the smaller correlation length (speckles' axial size) leading to more noise in the signal processing.

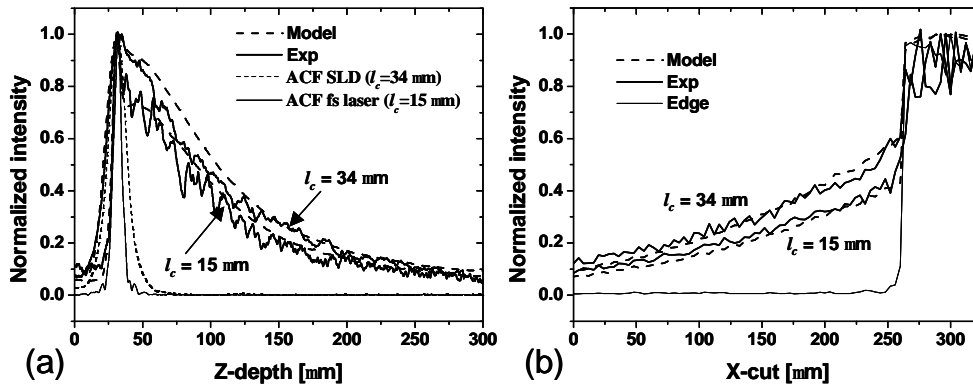


Fig. 19 Experimental (Exp) and theoretical (Model) results obtained in wide-field OCT for an SLD (coherence length $l_c = 34 \mu\text{m}$) and for a mode-locked femtosecond Ti:Sapphire laser ($l_c = 15 \mu\text{m}$) with $OD = 8$, $g = 0.85$, $D = 420 \mu\text{m}$, $NA = 0.25$: (a) Correlogram envelopes for the full mirror sample and envelopes of the two source autocorrelation functions (ACF) for reference; (b) Projection of the maximum intensity profile obtained with the half mirror sample and edge intensity profile in water for reference (Edge).

Dependence on sample properties

Cross-talk dependence on the anisotropy of the scattering solution is investigated first. The cross-talk signals measured with 3 different anisotropy parameters are shown in Fig 20a and 20b for the full mirror sample and for the half mirror sample, respectively. Microsphere diameters smaller ($d = 350$

nm), roughly equal ($d = 750$ nm) and larger ($d = 2050$ nm) than the illumination wavelength ($\lambda = 810$ nm in air i.e. $\lambda = 610$ nm in water) were used, yielding the anisotropy parameters $g = 0.57$, $g = 0.85$, and $g = 0.93$, respectively. For the 3 solutions, the scattering coefficients were adjusted to $\mu_s = 6.2$ mm^{-1} as explained in the method, leading to $\text{OD} = 8$ for $\Delta z = 650$ μm . Note that the chosen anisotropy coefficients are representative of biological tissues, typically lying between 0.7 and 0.99 [48].

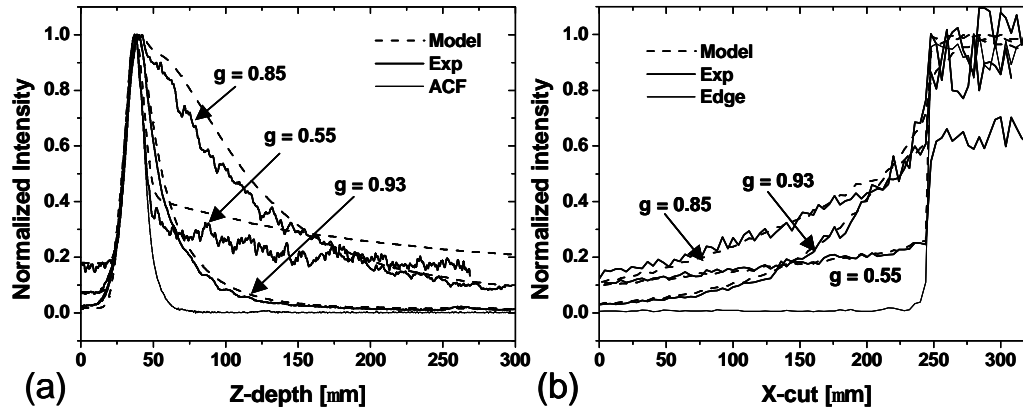


Fig. 20 Experimental (Exp) and theoretical (Model) results obtained in wide-field OCT for various anisotropies (g) with $\text{OD} = 8$, $D = 420$ μm , $\text{NA} = 0.25$: (a) Correlogram envelopes for the full mirror sample and envelope of the source autocorrelation function (ACF) for reference; (b) Maximum intensity profile obtained with the half mirror sample and edge intensity profile in water for reference (Edge).

Let us first comment on the results obtained with the full mirror sample. A wide-angle scattering solution is obtained with $g = 0.55$ resulting in a nearly flat cross-talk signal extending over a long distance, while a large peak emerges at the mirror interface. This peak, whose width corresponds to the ACF envelope, is caused by the ballistic light reflected by the mirror. The contrast, rather than the axial resolution, is reduced. With anisotropy $g = 0.85$ moderate forward scattering is obtained giving rise to a long tail dramatically reducing the axial resolution. With anisotropy $g = 0.93$ relatively high forward scattering is obtained resulting in limited multiply scattered light delays and in a signal width around 50% broader than the ACF envelope at FWHM.

With the half mirror sample, cross-talk effects are more pronounced with $g = 0.93$ showing that the moderately delayed multiply scattered light spreads quite significantly into the lateral dimension. The low signal measured on the edge with $g = 0.55$ is discussed at the end of section 3.3.4.

This study tends to show that, in our experimental conditions, the most deleterious cross-talk effects, in terms of large intensity signals spreading far from the ideal probe volume, are obtained for microsphere diameters approaching the wavelength.

Cross-talk dependence on the sample optical density (OD) is investigated with the standard scattering solution. Cross-talk signals measured for 3 different ODs with $g = 0.85$ are shown in Fig 21a and 21b for the full and the half mirror sample, respectively. The different OD values are obtained by varying the cell thickness Δz while maintaining the mirror edge in focus. The thickness $\Delta z = 320$ μm , $\Delta z = 650$ μm , and $\Delta z = 1000$ μm correspond to $\text{OD} = 4$, $\text{OD} = 8$, and $\text{OD} = 12.4$, respectively.

As expected, the measurements clearly show that the smaller the optical density of the sample, the less cross-talk is generated, and the better is the resolution. With the thickest sample, the peak signal is well behind the mirror interface showing the dominant role played by delayed multiply scattered light relative to ballistic light.

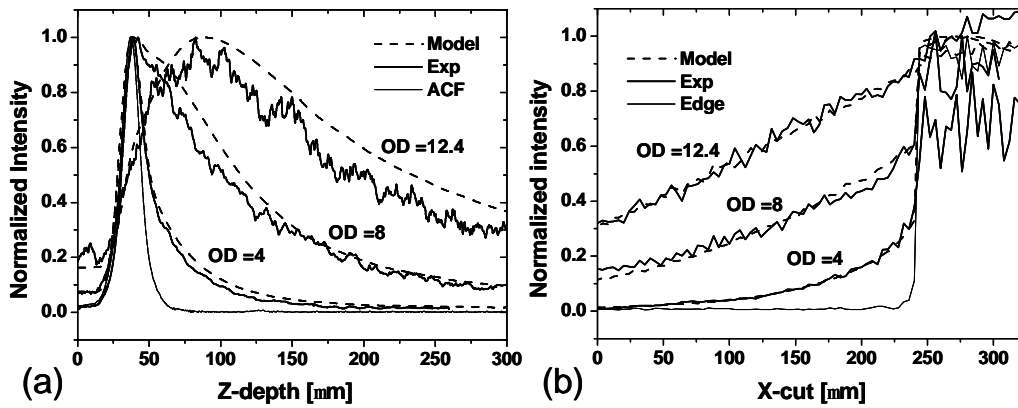


Fig. 21 Experimental (Exp) and theoretical (Model) results obtained in wide-field OCT for various optical densities (OD) with $\mu_s = 6.2 \text{ mm}^{-1}$, $g = 0.85$, $D = 420 \mu\text{m}$, and $\text{NA} = 0.25$ (a) Correlogram envelopes for the full mirror sample and envelope of the source autocorrelation function (ACF) for reference; (b) Maximum intensity profile obtained with the half mirror sample and edge intensity profile in water for reference (Edge).

The normalization procedure used for presenting results is hiding an important consequence of cross-talk. The significant multiply scattered light contribution in wide-field OCT causes a signal enhancement that is highly dependent on the sample properties. The amplitude of signals measured in wide-field OCT can thus be much higher than predicted by the ideal single-backscattering model used in point-scanning OCT [17]. In this model, which accounts for ballistic light only, the amplitude follows a negative exponential decrease according to the Lambert-Beer's law. The deviation from this law for wide-field OCT signals is investigated in the experiment described here below.

The full mirror sample was used with a scattering solution adjusted to $\mu_s = 6.2 \text{ mm}^{-1}$, first for a relative forward scattering solution ($g = 0.93$). The OD was varied by increasing the sample thickness in regular steps (Δz) while maintaining the reflecting interface in focus. The signal was measured for each thickness in both wide-field and confocal configurations. The exponential intensity decrease proportional to $e^{-(\alpha\Delta z)}$ predicted by Lambert-Beer's law ($\alpha = \mu_s = 6.2 \text{ mm}^{-1}$) is plotted in Fig. 22 (Beer's law). Also illustrated in this figure are the noise floors attained with the interferometer in wide-field configuration (sensitivity of -75 dB) and in confocal configuration (sensitivity of -96 dB).

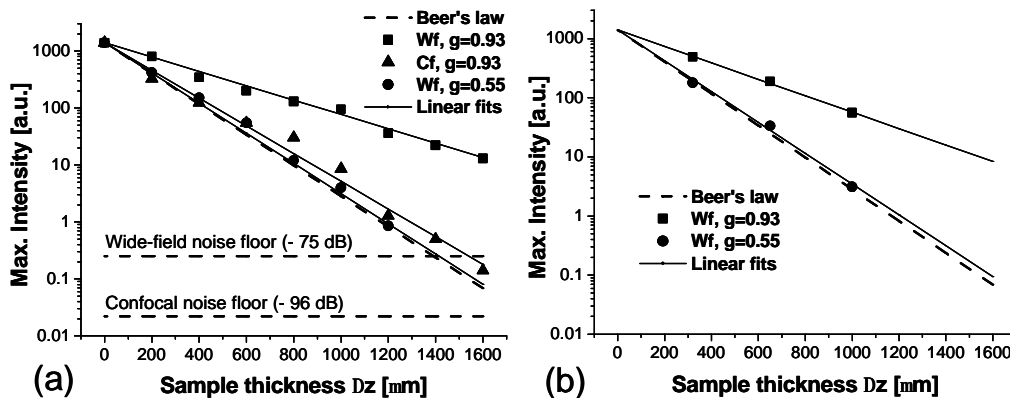


Fig. 22 Maximum intensities of OCT signals obtained with the full mirror sample for $\mu_s = 6.2 \text{ mm}^{-1}$ versus sample thickness for different anisotropies (g) and configurations. The decrease in intensity, for wide-field configuration (Wf) with $D = 420 \mu\text{m}$, $\text{NA} = 0.25$ and confocal configuration (Cf) with $\text{NA} = 0.25$, are compared to the exponential decrease predicted by Lambert-Beer's law (Theory). Linear fits are illustrated for all cases. (a) Experimental results. (b) Theoretical results obtained with our model.

With the wide-field configuration (Wf), the signal attenuation is considerably lower than predicted by the Lambert-Beer's law. Even at an OD = 20 ($\Delta z \approx 1600 \mu\text{m}$) the amplitude of the signal backscattered by the reflecting interface remains high. A linear fit through the experimental data leads to the attenuation constant $\alpha = 2.9 \text{ mm}^{-1}$. Our model is in excellent agreement with this value since it predicts an attenuation constant $\alpha = 3.0 \text{ mm}^{-1}$. This theoretical value was obtained by a linear fit between 3 points as shown in Fig. 22b.

With the confocal configuration (Cf), the linear fit through the experimental data leads to $\alpha = 5.7 \text{ mm}^{-1}$ corresponding to a only slightly lower attenuation than given by the Lambert-Beer's law ($\alpha = 6.2 \text{ mm}^{-1}$). This slight discrepancy, which might result from residual multiply scattered light [18], demonstrates well the significant rejection of the latter obtained in point scanning OCT.

To further test our model and investigate the dependence with the sample properties, the same experiment was repeated with a widely scattering solution ($g = 0.55$). In wide-field configuration we obtained $\alpha = 6.1 \text{ mm}^{-1}$, i.e. measurements nearly in total agreement with the Lambert-Beer's law and no signal enhancement takes place. Again, our model proves to be in excellent agreement with this value since predicting an attenuation constant $\alpha = 6.0 \text{ mm}^{-1}$. This theoretical value was obtained by a linear fit between 3 points as shown in Fig. 22b. Since a wide-angle scattering solution was used, one concludes that forward multiply scattered light accounts for signal enhancement in our case.

The significant deviation from Lambert-Beer's law in some cases reveals that, in wide-field OCT, the contribution of multiply scattered over ballistic light can occur already for less than one scattering mean free path. In point scanning OCT this transition from single scattering to diffuse light regime typically takes place after several mean free paths [49].

Discussion of theoretical results

Theoretical results are in very good agreement with experimental data for nearly all cases investigated. However, as can be observed with the full mirror sample, the model systematically leads to slightly higher amplitudes for cross-talk signals relative to the intensity peak. This means that the multiply scattered light contribution is slightly over-estimated. One possible explanation for this systematic difference could be the omission of polarization effects in our theoretical model that could lead to over-estimation of the multiple scattered component relative to the ballistic component. Indeed, according to Mie theory, polarization effects increase inversely with the microbeads' diameter. This hypothesis is supported by the results obtained when varying the anisotropy of the scattering solution (see Fig 20a) where the systematic difference is the highest for the lowest microbeads' diameter (i.e. highest at anisotropy) and vice and versa.

With the half mirror sample, this systematic difference cannot be directly observed since the experimental data are not normalized but adjusted with a multiplicative factor K_f (see 3.2). The latter were ranging between 0.9 and 1.2. Except for two cases, this led to signals with an average amplitude near one at the edge surface showing good agreement between experiment and theory where theoretical curves are normalized. The remaining two cases, corresponding to $g = 0.55$ (Fig 21b) and OD = 4 (Fig 21b), lead to average amplitudes at the edge of around 0.6 and 0.7, respectively. This means that a signal lower than expected was measured at the edge. The latter was deteriorated at some places (rounded break and missing reflective coating) due to the necessary cleaning procedure. The fact that in these two cases the ballistic contribution is dominant could explain why a lower signal was measured here rather than in the other cases.

3.3.5 Conclusions

We conducted a comprehensive study on multiple scattering effects in wide-field OCT realized with spatially coherent illumination. The good agreement between theoretical and experimental results for a wide range of different parameters confirms the validity of the model developed in section 3.2.

In addition, our study revealed the crucial importance of optical cross-talk in wide-field OCT when spatially coherent illumination is used. Cross-talk-generated noise spreads into the whole volume degrading both the lateral and the axial resolution. Despite temporal coherence gating, the contribution of multiply scattered light dominates at much lower probing depth than in point scanning OCT where additional confocal spatial filtering is used. This means that imaging in diffuse samples, with

diffraction limited performance, cannot be achieved in wide-field OCT realised with spatially coherent illumination except for a very moderate probing depth or turbidity. Moreover, the sensitivity of the method is likely to be limited by cross-talk rather than shot noise. Thus, increasing the source brightness with a pulsed laser does not necessarily lead to a better signal to noise ratio suggesting that spatially incoherent light sources might be the best option for wide-field OCT [33,43]. However, the possibility to use spatially coherent illumination in wide-field OCT very much depends on the sample properties as well as on the image quality required. For instance, cross-section imaging of an ex-vivo mouse ear was achieved with a quality allowing observation of the constitutive tissues [44]. The moderate scattering of the eye fundus might allow for spatially coherent wide-field OCT imaging with a sensitivity higher than with a thermal light source.

Our study also revealed the dependence of cross-talk generated noise on important system design parameters, as well as on some relevant sample properties. Cross-talk increases with the wide-field diameter, numerical aperture, source coherence length and sample optical density. Therefore, to minimize cross-talk effects, the wide-field diameter, the numerical aperture and the source coherence length should be reduced to a minimum. The smallest possible wide-field depends on the number of lateral pixels needed, which in turn depends on the application. For example, in our experiment, a lower cross-talk could be obtained for a reduction of the wide-field diameter from $D = 420 \mu\text{m}$ to $D = 85 \mu\text{m}$, corresponding to a reduction in number of lateral pixels from around 250 to 24, respectively. When striving to reduce the numerical aperture, a trade-off between the highest lateral resolution and the lowest cross-talk must be found. A broader source spectrum also favours cross-talk rejection. Finally, observations of significant deviations with Lambert-Beers' law revealed that the transition from single scattering to diffuse light regime happens for much lower optical depths in wide-field OCT than in point scanning OCT.

Future work of interest with our model could be a study of multiple scattering effects in point scanning OCT as well as in the Fourier domain OCT for parallel acquisition of cross-sectional images [50]. The stripe illumination necessary for the latter case should generate cross-talk. Conclusions of our study may well concern a wider class of imaging methods limited by cross-talk, such as for instance parallel time-resolved detection [51] or laser Doppler imaging [52].

References

- [1] M.G. Ducros, M. Laubscher, B. Karamata, S. Bourquin, T. Lasser, and R.P. Salathé, "Parallel optical coherence tomography in scattering samples using a two-dimensional smart-pixel detector array," *Opt. Com.* **202**, 29-35 (2002).
- [2] B. Karamata, P. Lambelet, M. Laubscher, M. Leutenegger, S. Bourquin, and T. Lasser, "Multiple scattering in optical coherence tomography. Part I: Investigation and Modeling," *J. Opt. Soc. Am. A* submitted.
- [3] B. Karamata, M. Leutenegger, P. Lambelet, M. Laubscher, S. Bourquin, and T. Lasser, "Multiple scattering in optical coherence tomography. Part II: Experimental and theoretical investigation of cross-talk in wide-field optical coherence tomography," *J. Opt. Soc. Am. A* submitted.
- [4] D. Huang, E.A. Swanson, C.P. Lin, J.S. Schuman, W.G. Stinson, W. Chang, M.R. Hee, T. Flotte, K. Gregory, C.A. Pufialito, and J.G. Fujimoto, "Optical Coherence Tomography," *Science* **254**, 1178-1181 (1991).
- [5] A.F. Fercher, "Optical coherence tomography," *J. Biomed. Opt.* **1**(2), 157-173 (1996).
- [6] J.M. Schmitt, "Optical Coherence Tomography (OCT): A Review," *IEEE J. selected topics in quantum electronics* **5**(4), 1205-1215 (1999).
- [7] A. Knüttel, J.M. Schmitt, and J.R. Knutson, "Low-coherence reflectometry for stationary lateral and depth profiling with acousto-optic deflectors and a CCD camera," *Opt. Lett.* **19**, 302-304 (1994).
- [8] E. Beaurepaire, A.C. Boccara, M. Lebec, L. Blanchot, and H. Saint-Jalmes, "Full-field optical coherence microscopy," *Opt. Lett.* **23**, 244-246 (1998).
- [9] G. Häusler and M.W. Lindner, "Coherence radar and spectral radar-New tools for dermatological diagnosis", *J. Bio. Opt.* **3**, 21-31 (1998).
- [10] S. Bourquin, V. Monterosso, P. Seitz, and R.P. Salathé, "Video rate optical low-coherence reflectometry based on a linear smart detector array," *Opt. Lett.* **25**, 102-104 (2000).
- [11] S. Bourquin, P. Seitz and R.P. Salathé, "Optical coherence tomography based on two-dimensional smart detector array," *Opt. Lett.* **26**, 512-514 (2001).
- [12] S. Bourquin, P. Seitz and R.P. Salathé, "Two-dimensional smart detector array for interferometric applications," *Elec. Lett.* **37**: 975-976 (2001).
- [13] H.J. van Staveren, C.J. Moes, M.J. van Marle, S.A. Prahl, and M. J. C. van Gemert, "Light scattering in Intralipid-10% in the wavelength range of 400-1100nm," *Appl. Opt.* **30**, 4507-4514 (1991).
- [14] J.A. Izatt, M.R. Hee, G.M. Owen, E.A. Swanson, J.G. Fujimoto, "Optical coherence microscopy in scattering media," *Opt. Lett.* **19**, 590-592 (1994).
- [15] E.A. Swanson, D. Huang, M.R. Hee, J.G. Fujimoto, C.P. Lin, C.A. Puliafito, "High-speed optical coherence domain reflectometry," *Opt. Lett.* **17**, 151-153 (1992)
- [16] S.T. Flock, S.L. Jacques, B.C. Wilson, W.M. Star, and M.J.C van Gemert, "The Optical Properties of Intralipid: A phantom Medium for Light Propagation Studies," *Lasers in Surgery and Medicine* **12**, 510-519 (1992).
- [17] J.M. Schmitt, A. Knuettel, and R.F. Bonner, "Measurement of optical properties of biological samples in low-coherence reflectometry," *Appl. Opt.* **32**, 6032-6042 (1994).

- [18] M.J. Yadlowsky, J.M. Schmitt, R.F. Bonner, "Multiple scattering in optical coherence microscopy," *Appl. Opt.* **34**, 5699-5707 (1995).
- [19] D.J. Smithies, T. Lindmo, Z. Chen, J.S. Nelson, and T.E. Milner, "Signal attenuation and localization in optical coherence tomography studied by Monte Carlo simulation," *Phys. Med. Biol.* **43**, 3025-3044 (1998).
- [20] J.W. Goodman, "Statistical properties of laser speckle patterns," in *Laser speckle and related phenomena*, Topics in applied physics: Vol. 9, ed. J.C. Dainty, pp. 9-75 (1975).
- [21] A.M. Rollins, M.D. Kulkarni, S. Yazdanfar, R. Uung-arunyawe, and J.A. Izatt, "In vivo video rate optical coherence tomography," *Opt. Exp.* **3**(6), 219-229, (1998).
- [22] W. Rudolph, M. Kempe, "Topical review: Trends in optical biomedical imaging," *J. Mod Opt.* **44**, 1617-1642 (1997).
- [23] L. Thrane, H.T. Yura, and P.E. Andersen, "Analysis of optical coherence tomography systems based on the extended Huygens-Fresnel principle," *J. Opt.Soc.Am. A* **17**, 484-490 (2000).
- [24] A. Ishimaru, Y. Kuga, R. Cheung, K. Shimizu, "Diffusion of a pulse in densely distributed scatterers," *J. Opt.Soc.Am. A* **68**, 1045-1050 (1978).
- [25] M.S. Patterson, B. Chance and B. C. Wilson, "Time resolved reflectance and transmittance for the non-invasive measurement of tissue optical properties," *Appl. Opt.* **28**, 2331-2336 (1989).
- [26] A. Ishimaru, Y. Kuga, R. Cheung, K. Shimizu, "Scattering and diffusion of a beam wave in randomly distributed scatterers," *J. Opt. Soc. Am. A* **73**, 131-136 (1983).
- [27] S.L. Jacques, "Time resolved propagation of ultrashort laser pulses within turbid tissues," *Appl. Opt.* **28**, 2223-2229 (1989).
- [28] G. Yao, L.V. Wang, "Monte Carlo simulation of an optical coherence tomography signal in homogeneous turbid media," *Phys. Med. Biol.* **44**, 2307-2320 (1999).
- [29] Y. Pan, R. Birngruber, J. Rosperich, R. Engelhardt, "Low-coherence optical tomography in turbid tissue: theoretical analysis," *Appl. Opt.* **34**, 6564-6574 (1995).
- [30] J.M. Schmitt and A. Knuettel, "Model of optical coherence tomography of heterogeneous tissue," *J. Opt. Soc. Am. A* **14**, 1231-1242 (1997).
- [31] H.T. Yura, "Signal-to-noise ratio of heterodyne lidar signal systems in the presence of atmospheric turbulence," *Opt. Acta* **26**, 627-644 (1979).
- [32] R.F. Lutomirski, "Atmospheric degradation of electrooptical system performance," *Appl. Opt.* **17**, 3915-3921 (1978).
- [33] B. Karamata, M. Laubscher, P. Lambelet, R.P. Salathé, and T. Lasser, "Spatially incoherent illumination as a mechanism for cross-talk suppression in wide-field optical coherence tomography," *Opt. Lett.* **29**, 736-738 (2004).
- [34] M. Pircher, E. Goetzinger, R. Leitgeb, A.F. Fercher, C.K. Hitzenberger, "Speckle reduction in optical coherence tomography by frequency compounding," *J. Biomed. Opt.* **8**, 565-569 (2003).
- [35] J.B. Kinsinger and S. Mallick, "Spatial coherence in Rayleigh-scattered light," *J. Opt. Soc. Am.* **64**, 1274-1275 (1974).
- [36] J.M. Schmitt and G. Kumar, "Turbulent nature of refractive index variations in biological tissues," *Opt. Lett.* **16**, 1310-1312 (1996).
- [37] J.M. Schmitt, S.H. Xiang, K.M. Yung, "Speckle in Optical Coherence Tomography", *J. Biomed. Opt.* **4**, 95-105(1999).
- [38] L.H. Wang, S.L. Jacques, and L.-Q. Zheng, "MCML - Monte Carlo modeling of photon transport in multi-layered tissues," *Comput. Meth. Prog. Biomed.* **47**, 131-146 (1995).
- [39] J.W. Goodman, "Statistical optics", pp. 60-109 (Wiley Classics Library, 1985).

- [40] Q. Lu, X. Gan, M. Gu, and Q. Luo, "Monte Carlo modeling of optical tomography imaging through turbid media," *Appl. Opt.* **43**, 1628-1636 (2004).
- [41] A.F. Fercher, W. Drexler, C.K. Hitzenberger, and T. Lasser, "Optical coherence tomography - principles and applications," *Rep. Prog. Phys.* **66**, 239-303, (2003).
- [42] M. Laubscher, M. Ducros, B. Karamata, T. Lasser, and R.P. Salathé, "Video-rate three-dimensional optical coherence tomography," *Opt. Exp.* **9**, 429-435 (2002).
- [43] L. Vabre, A. Dubois, and A.C. Boccara, "Thermal full-field optical coherence tomography," *Opt. Lett.* **27**, 530-532 (2002).
- [44] E. Abraham, E. Bordenave, N. Tsurumachi, G. Jonusauskas, J. Oberlé, and C. Ruillère, "Real-time two-dimensional imaging in scattering media by use of a femtosecond Cr⁴⁺: forsterite laser," *Opt. Lett.* **25**, 929-931 (2000).
- [45] B. Bouma, G. J. Tearney, S. A. Boppart, M. R. Hee, M. E. Brezinski, J. G. Fujimoto, "High-resolution optical coherence tomographic imaging using a mode-locked Ti:Al₂O₃ laser source," *Opt. Lett.* **20**, 1486-1488 (1995).
- [46] A.F. Fercher, C.K. Hitzenberger, M. Sticker, E. Moreno-Barriuso, R. Leitgeb, W. Drexler and H. Sattmann, "A thermal light source technique for optical coherence tomography," *Opt. Com.* **185**, 57-65 (2000).
- [47] F. Lexer, C.K. Hitzenberger, W. Drexler, S. Molebny, H. Sattmann, M. Sticker and A.F. Fercher, "Dynamic coherent focus OCT with dept-independent transversal resolution," *J. Mod. Opt.* **46**, 541-553 (1999).
- [48] W-F. Cheong, S. A Prahl and A.J. Welsh, "A review of the optical properties of biological tissues," *J. Quantum. El.* **26**, 2166-2185 (1990).
- [49] K.K. Bizheva, A.M. Siegel, and D.A. Boas, "Path-length-resolved dynamic light scattering in highly scattering random media: The transition to diffusing wave spectroscopy," *Phys. Rev. E PRE* **58**, 7664-7667 (1998).
- [50] R. Leitgeb, C.K. Hitzenberger, and A.F. Fercher, "Performance of Fourier domain vs. time domain optical coherence tomography", *Opt. Exp* **11**, 889-894 (2003).
- [51] J.C. Hebden, R.A. Kruger, and K.S. Song, "Time resolved imaging through a highly scattering medium," *Appl. Opt.* **30**, 788-794 (1991).
- [52] Serov, W. Steenbergen, and F de Mul, "Laser Doppler perfusion imaging with a complementary metal oxide semiconductor image sensor," *Opt. Lett.* **27**, 300-302 (2002).

CHAPTER IV

Wide-field optical coherence tomography with spatially incoherent illumination

4.1 Cross-talk suppression

In the preceding chapter, investigation of wide-field optical coherence tomography (OCT) with spatially coherent illumination revealed that optical cross-talk can be a serious limitation. This raises an important question: can wide-field OCT be realized without cross-talk generated noise?

With wide-field illumination, large amounts of multiply scattered light are unavoidably collected. Therefore, cross-talk can be suppressed only by preventing interference between multiply scattered light and the reference field. As explained hereafter, this can be achieved by controlling the degree of spatial coherence of the wide-field. The idea is to create, for each parallel detection channel, an effect equivalent to confocal spatial filtering by exploiting spatial coherence effects. This provides a “spatial coherence gating” which can be appreciated in a relatively straightforward and intuitive manner thanks to the concept of spatial modes introduced in Chapter II.

The principle of spatial coherence gating relies on the creation of mutually incoherent probe volumes within the sample. In the interferometer, such probe volumes are duplicated in the reference arm. When reference field (U_R) and sample field (U_S) recombine on the detector plane, interference can occur only if corresponding probe volumes, for instance A_R and A_S , are superimposed as illustrated in Fig. 1. The reference field, which is not perturbed by scattering, acts as a spatial coherence gate allowing interference only with light originating from the sample probe volume. This selective interference produces a detectable field $U_T = U_R + U_S$ allowing cross-talk suppression in wide-field illumination.

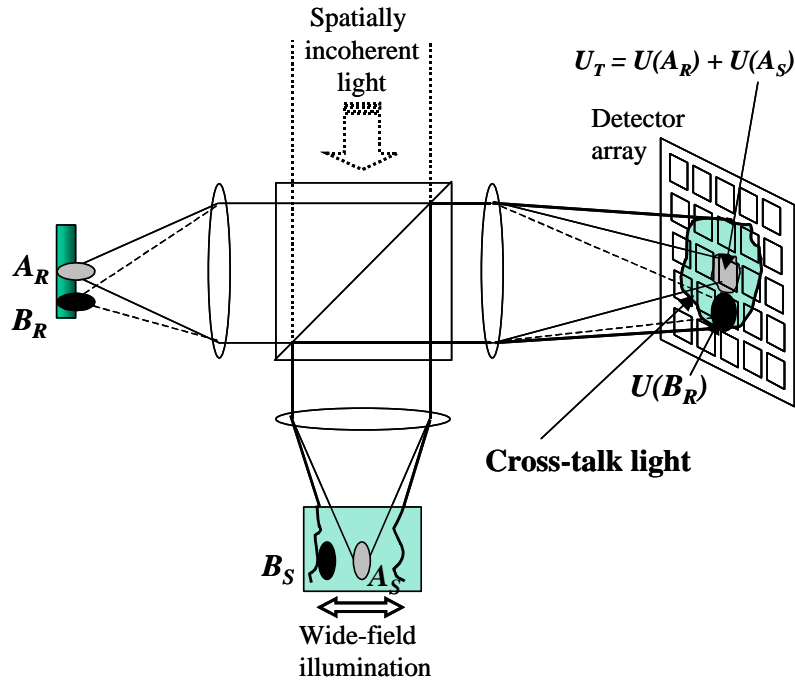


Fig. 1 Concept of spatial coherence gating. Light from the probe volume A_S can interfere only with light from its replica A_R . Cross-talk light generated by wide-field illumination is removed by selective interference producing a field U_T .

Optimal cross-talk rejection, i.e. a rejection equivalent to that of multiply scattered light in point scanning OCT systems, is obtained when there is perfect overlap between probe and coherence volumes as defined in 2.1.3. Therefore, one must create coherence volumes matching the probe volumes. Generally, in OCT, the axial dimension of both coherence and probe volumes is the same since determined by the source coherence length. Thus, the only condition to be met is that the cross-section area of a probe volume matches the coherence area A_c of the coherence volume.

According to the Van Cittert-Zernike theorem, the spatial extent of a spatial mode obeys the fundamental relationship (see 2.1.3):

$$A_c \Omega = I^2, \quad (1)$$

where I is the central wavelength, Ω the solid angle in which light is confined, and A_c the coherence area, as defined in section 2.1.3.

This universal relationship imposes a limit to the maximum extent a coherent flux of light, that is a single spatial mode, can fill. Assuming cylindrical symmetry, the 2-dimensional counterpart of Eq. (1) becomes:

$$d_c = \frac{4 I}{p q} \cong 1.27 \frac{I}{q}, \quad (2)$$

where q is the divergence angle of a mode, and d_c the diameter of the coherence area. The diameter of a probe volume is determined by the limit of resolution, which, for a diffraction-limited optical system, yields an airy disc diameter:

$$d_A = 2.44 \frac{I}{NA} \quad (3)$$

To have a probe volume matching a coherence volume, the condition $d_c = d_A$ must be fulfilled. This implies that $NA \cong q/2$, where q is the full angle under which the source is viewed. According to the Van Cittert-Zernike theorem, this condition is directly met when the objective aperture is filled with spatially incoherent light, since both the NA and the angle q are set by the objective aperture.

The ability to fill the entrance pupil with spatially incoherent light depends on the size of the incoherent, i.e. extended, light source, which necessarily has a limit. The minimum size of the source is actually related to the wide-field dimension on the sample side. The concept of spatial modes imposes a restriction on the experimental design. Indeed, the number of spatial modes N_S generated by the source must be at least equal to the number of spatial modes N_{wf} contained in the wide-field. Generally, the number of modes N depends on the spatial extent of a light beam, which is defined as the product of the beam cross-sectional area A and the beam solid divergence angle Φ . Therefore:

$$N = \frac{A\Phi}{A_c\Omega} = \frac{A\Phi}{I^2} \quad (4)$$

Thus, to meet the requirement $N_S \geq N_{wf}$, the spatial extent of the source must be equal or superior to the spatial extent defined by the wide-field and the illumination angle. The optimal power throughput is obtained when $N_S = N_{wf}$.

The requirements for an optimal spatial coherence gating are the following:

- (i) the objective aperture must define the entrance pupil of the illumination system.
- (ii) the corresponding acceptance angle \mathbf{Y} is filled with spatially incoherent light.
- (iii) the spatial extent of the source, delimited by \mathbf{Y} , is equal or superior to the product of the solid angle, defined by the NA and the field of view.

Compliance with these requirements provides spatial coherence gating with an effect equivalent to confocal spatial filtering in a parallel detection scheme. Actually, this equivalence goes beyond rejection capabilities of multiply scattered light. Indeed, spatial coherence gating yields an enhanced axial and lateral resolution identical to that of confocal imaging systems. This extremely interesting property, obtained whenever an extended source is combined with an interferometric detection process, was described by several authors in various contexts (Davidson et al. [1], Lee et al. [2], and more recently by Somekh et al. [3]). In a closely related context, Sun and Leith showed the equivalence of extended-source image plane holography and the confocal imaging process [4].

In summary, the concept of spatial modes was used to explain how the source coherence properties can yield an effect equivalent to confocal gating in a wide-field OCT scheme. Such spatial coherence gating leads to cross-talk suppression, i.e to rejection of multiply scattered light to a level comparable to point scanning OCT, as shown in the next section.

4.2 Spatial coherence gating with a thermal light source

Cross-talk rejection capability with spatial coherence gating (see 4.1) is investigated by comparing (i) spatially coherent to spatially incoherent illumination, realized with a thermal light source, and (ii) point scanning OCT to wide-field OCT with spatially coherent illumination.

4.2.1 Method

The optical set-up (Fig. 2) consists of a Linnik interferometer with a flip mirror (FM) allowing to select either spatially coherent or spatially incoherent illumination. The configuration corresponding to spatially coherent illumination is described in section 3.3.2. In both configurations, the image of the sample is obtained by lenses $L_{4/5}$ forming a microscope (x30 magnification) as sketched for the reference arm (in Fig. 2). The detection scheme and signal processing, shared by both configurations, are also described in section 3.3.2.

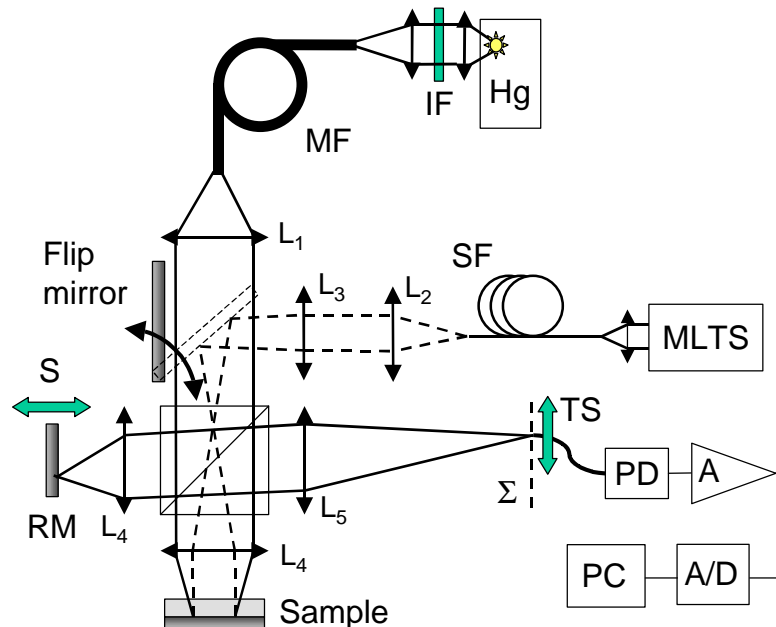


Fig. 2 Scheme of a wide-field OCT set-up with spatially coherent (FM at 45°) and spatially incoherent (FM vertical) illumination: mercury arc lamp (Hg); mode-locked fs Ti:Sapphire laser (MLTS); single mode fiber (SF); multimode fiber (MF); interference filters (IF); reference mirror (RM); scanner (S); translating stage (TS); achromatic lenses ($L_{1/2/3/5}$); microscope objectives x10, $NA = 0.25$ (L_4); photodiode (PD); amplifier (A).

Spatially incoherent illumination is obtained by injecting a 100 W Hg arc lamp into a multimode fiber (MF) which delivers highly spatially incoherent light into the interferometer. The use of a multimode fiber provides a uniformly bright (equivalent to Koehler illumination) and easy to handle light source. In addition, the well defined source size facilitates system design. In our case, the 550 μm fiber core, positioned at the focal plane of L_1 , is directly imaged on the focal plane of objective L_4 , leading to a 400 μm diameter wide-field.

Optimal spatial coherence gating is obtained since the illumination system complies with the three design requirements formulated in the preceding section. The objective aperture, which is the entrance pupil of the illumination system, is filled with spatially incoherent light, fulfilling requirements (i) and (ii). With a fiber NA of 0.21 and an objective NA of 0.25, requirement (iii) relative to the spatial extent

is fulfilled too. Indeed, $N_S \cong N_{wf}$ since the spatial extent on the source side nearly corresponds to that on the sample side ($0.21^2 \times 550 \cong 0.25^2 \times 400$). Since nearly all spatial modes are conserved in the illumination process, our design is optimal regarding power throughput.

For a relevant comparison between spatially coherent and spatially incoherent illumination, wide-field diameter, temporal coherence gating, and power must be the same in both configurations.

The wide-field intensity profile depends on the illumination. In spatially coherent illumination, a Gaussian beam is collimated onto the sample while, in spatially incoherent illumination, a top hat intensity profile is obtained by imaging the multimode fiber core. The waist (at $1/e$) of the Gaussian illumination profile matches the $400 \mu\text{m}$ large incoherent wide-field illumination (Fig. 3). We attribute the relatively noisy top hat profile to insufficient polishing of our multimode fiber.

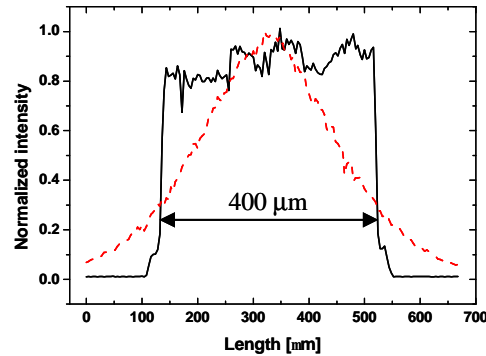


Fig. 3 Wide-field illumination profiles obtained with spatially coherent (dashed curve) and spatially incoherent illumination (solid curve).

The mode-locked Ti:Sapphire laser spectrum is centered around 800 nm , with a 70 nm bandwidth (FWHM). To obtain a similar spectrum with the Hg light source, a smooth portion of the spectrum - between 750 nm and 850 nm - is filtered through a combination of high- and low-pass interference filter (IF). Both filtered and non-filtered spectrums are shown in section 4.3 (Fig. 8). As illustrated in Fig. 4, very similar autocorrelation function envelopes are obtained for both sources. The corresponding measured axial resolutions at FWHM in air are 4 and $4.5 \mu\text{m}$, with the Hg and pulsed laser sources, respectively.

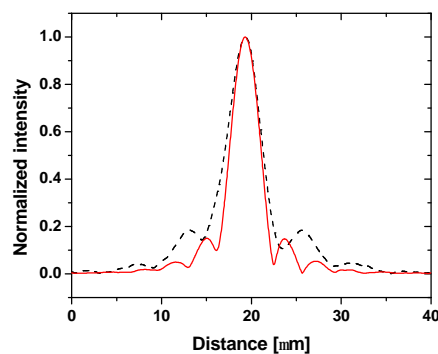


Fig. 4 Autocorrelation function envelopes for the Hg (solid line) and MLTS (dashed line) source. Distance corresponds to scan mirror displacement.

The side-lobes present in the filtered Hg source and in the mode-locked fs Ti:Sapphire laser autocorrelation functions, are due to a nearly squared spectrum and to polarization effects in the 100 meter long single mode fiber, respectively.

To illuminate the sample with the same power as with the Hg source the MTLs power was attenuated to 1 mW with a neutral density filter placed between L_2 and L_3 .

4.2.2 Results

To compare spatially coherent illumination and spatially incoherent illumination in terms of coherent cross-talk, we used a US air force reflecting resolution target covered with a scattering solution. The latter, consisting of 2 μm polystyrene microspheres diluted in de-ionized water, yields an anisotropy parameter $g = 0.93$. A cell, with inner thickness of 650 μm , delimited by the resolution target and a 150 μm thick cover glass, was filled either with water or with the scattering solution. Wide-field illumination was centered on element 2, group 6, of the resolution target (71.8 lines/mm) whose axial position was adjusted, with the cell filled with water, to form an image in the focal plane of L_5 . Water was then replaced by the scattering solution whose scattering coefficient, measured independently, corresponds to 8 optical depths in the cell (two-ways).

Fig. 5a and 5b show OCT cross-section images of the pattern's stripes - with the normalized intensity on the vertical axis - obtained with spatially coherent and spatially incoherent illumination, respectively. Despite short temporal coherence gating, spatially coherent illumination generates a considerable amount of cross-talk, degrading both axial and lateral resolutions (Fig. 5a). Due to scatterers' random positions inherent to Brownian motion, cross-talk is a speckled signal, different at each measurement. The plots correspond to the average cross-talk signal of 25 demodulated OCT signals. With wide-field spatially incoherent illumination, the spatial coherence gating provided by our optimal design strongly reduces cross-talk allowing a good resolution of the 3 stripes (Fig. 5b).

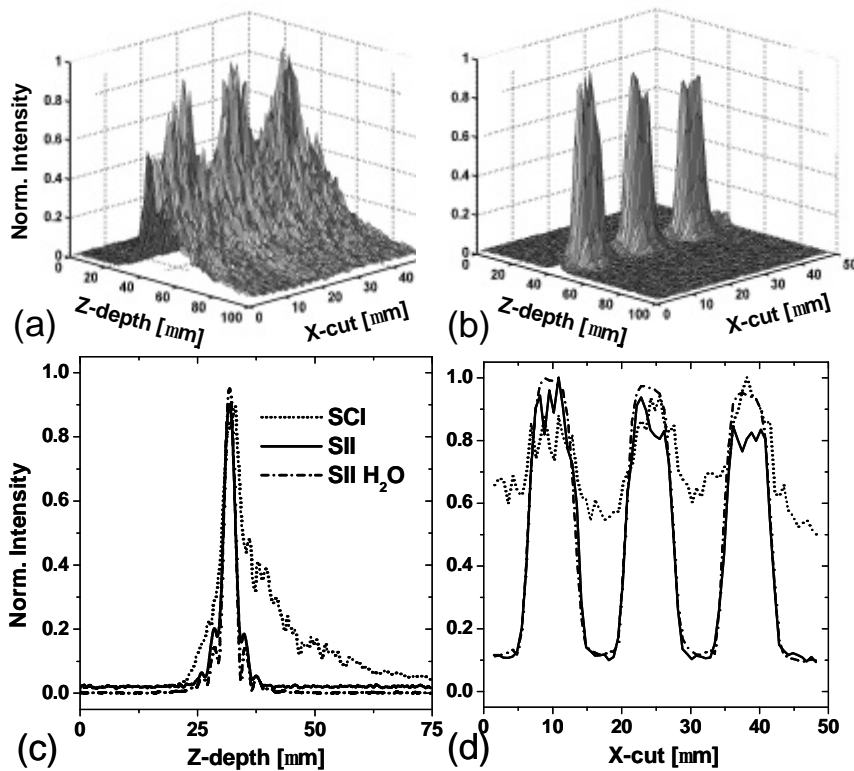


Fig. 5 Cross-section wide-field OCT image of a US air force resolution target covered with a 8 optical depths scattering solution ($g = 0.93$): (a) spatially coherent illumination (SCI); (b) spatially incoherent illumination (SII); (c) cuts along the z-axis of Fig. 2a (across the middle stripe), (d) cuts along the x-axis of Fig. 2b (across the reflecting target interface). Curves labelled “SII H_2O ” correspond to the same cuts of the same image acquired in water with SII. All curves are normalized and correspond to an average of 25 demodulated signals.

For a better quantitative estimate of spatial coherence gating efficiency, longitudinal cuts of the two 3D plots are compared. Cuts along the z-axis (across the middle stripe), and those along the x-axis

(across the sample interface), are shown in Fig. 5c and d, respectively. It appears that cross-talk, a strong coherent noise contribution, is responsible for a loss of contrast. The latter can, nevertheless, be restored with spatially incoherent illumination.

To better illustrate the spatial coherence gating efficiency, the same cross-section image was acquired in water with spatially incoherent illumination. The two normalized longitudinal cuts displayed in Fig. 5c/d correspond to plots obtained with spatially incoherent illumination in water (dash-dot curves) and in the scattering solution (solid curves). Except slightly higher amplitude side-lobes and a more rippled profile in the scattering solution, their near identity reveals that in our case, axial and lateral resolutions are fully restored. There are only two minor differences between the plots, i.e. in the scattering solution, the side-lobes have a slightly higher amplitude and the profile is more rippled, possibly due to the noisy illumination profile.

To show that spatial coherence gating achieves cross-talk suppression to the same extent as point-scanning OCT, we compared confocal illumination with spatially incoherent illumination. A confocal configuration with properties equivalent to point-scanning OCT can be obtained by simply removing lens L_3 . The monomode fibre is then imaged onto the sample providing a confocal spot illumination. The latter is attenuated with neutral density filters so as to obtain a sensitivity of 75 dB in both configurations. We use the full mirror sample (see 3.3.2), with scattering solution ($OD = 8$, $g = 0.85$). The correlograms obtained reveal that cross-talk rejection is equally efficient in both configurations (Fig. 6). Differences near the side-lobes are due to scanner instabilities as well as to residual multiply scattered light. For comparison, the correlogram obtained with spatially coherent illumination is also shown.

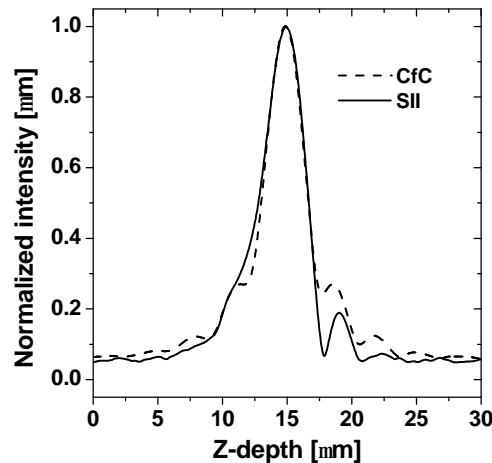


Fig. 6 Comparison of wide-field OCT with spatially incoherent illumination (SII) to point scanning OCT with confocal configuration (CfC) for a mirror covered with the scattering solution ($OD = 8$, $g = 0.85$).

Fig. 7 shows the qualitative improvement obtained with spatially incoherent relative to spatially coherent illumination in the case of an enamel-dentin junction of an ex-vivo tooth. Due to aging, the enamel (E) is separated from the dentine (D) leaving a gap in between. The latter, visible with spatially incoherent illumination, is totally blurred with spatially coherent illumination. Both images were acquired with 50 lateral steps, corresponding to $3.33 \mu\text{m}$ pixels on the sample. The low contrast at the E-D junction is due to low sensitivity (75 dB).

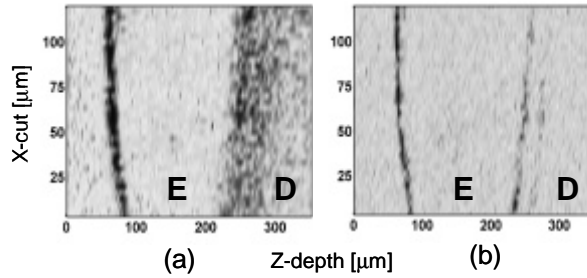


Fig. 7 Longitudinal cross-section wide-field OCT images of a gap between enamel (E) and dentine (D) of an ex-vivo tooth, acquired with (a) spatially coherent, and (b) spatially incoherent illumination. Signal reflectance is represented in logarithmic grey scale.

4.2.3 Conclusions

We have demonstrated that the coherent cross-talk generated in wide-field OCT by spatially coherent illumination can be suppressed with spatially incoherent illumination provided by thermal light sources. With spatially incoherent illumination, performance of wide-field OCT is comparable to that of point-scanning OCT. However, despite the fact that wide-field OCT requires less brightness than point-scanning OCT, the power per spatial mode radiated by thermal light sources is too low to permit a high SNR while maintaining a fast acquisition speed (see section 4.4.).

Although our initial aim was also to investigate the transition from spatially coherent to spatially incoherent illumination, we could not examine the intermediate cases for the following practical reason. Let us consider a diaphragm at the aperture of lens L_1 limiting Ω by approximately a factor of 20 and generating coherence zones 20 times larger than the resolution Δx ($d_c \cong 40$ microns). The power would then be about 400 (20 x 20) times lower leading to poor sensitivity. In addition, as revealed by our study, cross-talk falls dramatically with the illumination diameter (see section 3.3). Therefore, under these conditions, no cross-talk could be measured. To perform such a study, a powerful pseudo-thermal light source would be required (see 4.5).

Besides allowing for spatial coherence gating, a thermal light source has a naturally broad spectrum, potentially leading to a very high axial resolution. This important advantage is briefly investigated in the following section.

4.3 Ultrahigh axial resolution

In OCT, the axial resolution is determined by the source spectrum. According to the Wiener-Khinchine theorem, the source bandwidth and the coherence time are a Fourier transform pair (see 2.2.1). Thus, the broader the spectrum, the higher the axial resolution. In the past decade, intensive development of customized ultra-short pulsed laser sources led to a spectacular improvement of axial resolution [5][6]. Such sources allow to combine broad spectrum and high brightness. In point-scanning OCT, where extreme scan speeds are achieved, high brightness is an absolute necessity.

Wide-field OCT can exploit sources with a much lower brightness, such as thermal light sources, which have the advantage of a naturally very broad spectrum [7][8]. The low brightness of these sources is an issue which will be investigated in the next section. Therefore, one should choose the brightest thermal light sources for OCT applications, with a smooth, ideally Gaussian, spectrum. Although arc lamps are the hottest (6000 K), i.e. brightest commonly available sources, they are handicapped by spectral lines superimposed to their blackbody radiation spectrum. Halogen lamps are not as hot (3300 K) but have the advantage of a smooth blackbody radiator spectrum.

Here, we will investigate the potential in terms of resolution of a 100 W mercury arc lamp like that described in 4.2. Its spectrum, shown in Fig. 8, reveals that Hg lines are mostly present in the UV and IR domains.

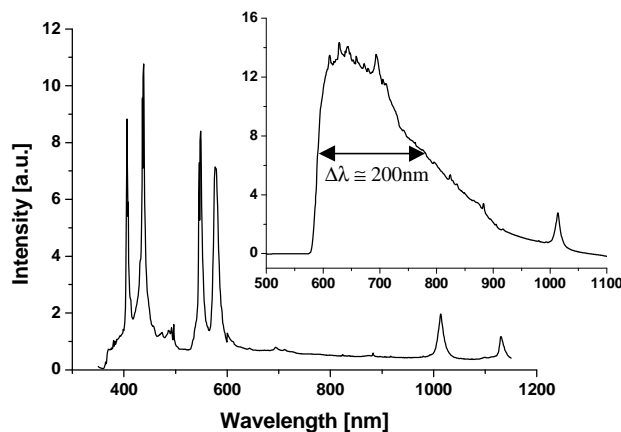


Fig. 8 The Hg spectrum recorded by a spectrometer with flat spectral response. The inset corresponds to the spectrum filtered with a high-pass optical wavelength filter at 590 nm, and multiplied by the silicon photodetector spectral sensitivity.

To exploit a portion of the Hg spectrum devoid of spectral lines, while maximising power and resolution, the spectral range from 600 to approximately 1000 nm is used. This is achieved by using a combination of a high-pass wavelength filter at 590 nm (OG 590 from Schott) and a low-pass filter consisting of a silicon photodetector, whose spectral response falls down to zero above 1100 nm. The filtered spectrum multiplied by the silicon detector spectral response is shown in the inset of Fig. 8. Thus, a relatively smooth triangle-like spectrum with a 200 nm bandwidth (FWHM) is obtained.

The experimental and the theoretical autocorrelation functions corresponding to this spectrum are shown as a function of the scan mirror displacement in Fig. 9a and 9b, respectively. The former was measured with the set-up described in section 4.2, while the latter was obtained by the Fourier transform of the spectrum. Theoretical and experimental results are in good agreement. Their central wavelength is at around 660 nm.

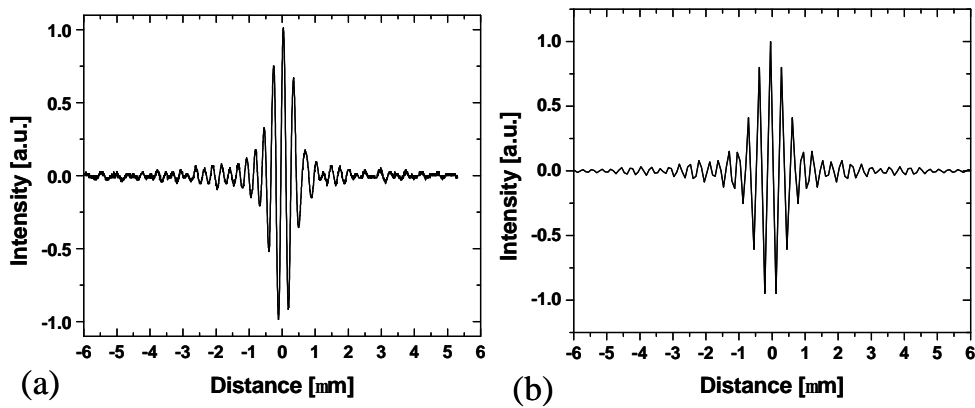


Fig. 9 Autocorrelation function of a filtered Hg arc lamp as a function of the scan mirror displacement: (a) experimental (b) theoretical.

Experimental and theoretical axial resolutions, defined at FWHM in air, are around $0.9 \mu\text{m}$ and $1.1 \mu\text{m}$, respectively. The slightly larger theoretical value is likely to be due to an approximate knowledge of the silicon photodetector spectral response. The latter was obtained by fitting values performed with intensity measurements using 5 nm bandwidth calibrated filters to cover the spectrum of interest in 50 nm steps.

The axial resolution obtained in our system is in the order of the resolutions attained with state of the art ultrashort pulsed lasers [6]. In addition, the autocorrelation function exhibits a Gaussian-like shape with moderate side-lobes. The narrowest autocorrelation functions obtained with state of the art pulsed lasers often deviate quite significantly from an ideal Gaussian spectrum and are endowed with side-lobes sometimes reaching up to 30 % of the maximum.

It is interesting to note that other groups obtained slightly lower axial resolutions than ours, while using broader spectra. Fercher et al reported an axial resolution of $1.1 \mu\text{m}$ using either halogen lamp with 320 nm (FWHM), or an unfiltered Xenon arc lamp between 300 and 1100 nm [7]. However, in the latter case, the obtained correlogram exhibited important side lobes. Vabre et al. reported an axial resolution of $1.3 \mu\text{m}$ with a halogen lamp without limiting the spectrum with optical filters [8]. Thus, to our knowledge, our system provides the highest presently achieved axial resolution in OCT with a thermal light source.

We illustrate the potential of this high axial resolution by unambiguously resolving the interfaces of a $\Delta z \cong 3 \mu\text{m}$ thick nitrocellulose pellicle beam splitter (Fig. 10). The higher signal corresponds to the second interface, which is endowed with a reflective coating. Distance in the plot corresponds to the scan mirror displacement. Taking into account the nitrocellulose refractive index ($n = 1.5$), the pellicle thickness is around $2 \mu\text{m}$.

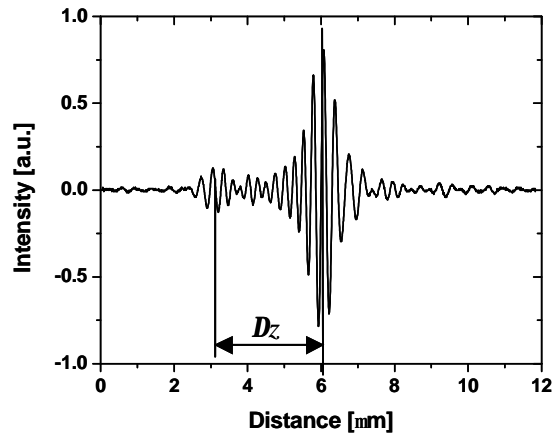


Fig. 10 Interferometric signal obtained with a filtered Hg arc lamp and an approximately $2 \mu\text{m}$ thick pellicle beamsplitter as sample. Distance in the plot corresponds to the scan mirror displacement.

The very high resolutions obtained with a broad spectrum can be easily lost in situations involving dispersion effects. To illustrate this important problem we measured the signals generated by the two interfaces of a $140 \mu\text{m}$ thick microscope cover glass placed in the sample arm (Fig. 11). Due to dispersion, the correlogram corresponding to the second interface is much broader than the autocorrelation function. The axial resolution is reduced by a factor of five.

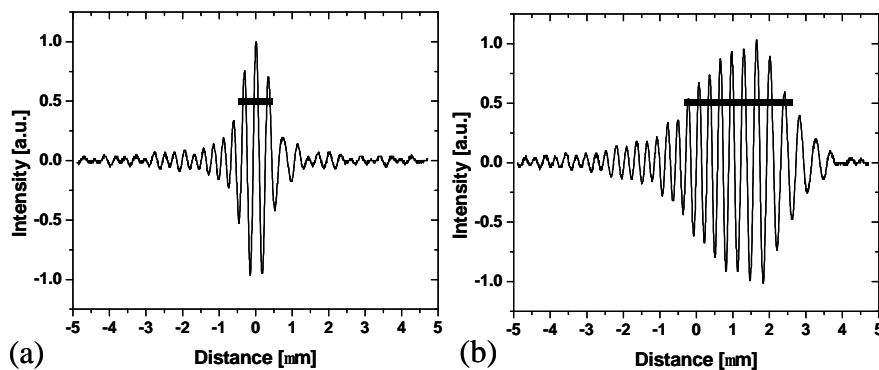


Fig. 11 Normalized correlogram obtained with a filtered Hg arc lamp (a) without dispersion effects and (b) with dispersion effects caused by a $140 \mu\text{m}$ thick microscope cover glass. Distance in the plots corresponds to the scan mirror displacement. The thick stripes approximately show the axial resolution at FWHM.

Dispersion effects can be eliminated by appropriately balancing the interferometer, i.e. by a set-up with identical dispersion in both arms. Since the refractive index of biological samples is close to that of water, fitting the two interferometer arms with identical water-immersion microscope objectives would suppress most dispersion effects. This solution, successfully implemented by Vabre et al., led to a $1 \mu\text{m}$ axial resolution in biological tissues [8].

Alternatively, dispersion can be compensated with appropriate signal processing [9]. Fercher et al. developed a numerical algorithm which was applied to our data and restored the resolution characteristics of dispersion free samples [10].

In conclusion, we obtained amongst the highest axial resolution in OCT so far reported by using an Hg arc lamp with a common high pass filter. Although the natural Planck spectrum was modified with a steep filter, a relatively Gaussian-like autocorrelation function with moderate side-lobes could be

obtained. This demonstrates the possibility to use thermal light sources at 6000 K, generally endowed with spectral lines, in wide-field OCT. The possibility to use such hot sources instead of sources at around 3000 K, is very important since it provides a substantial increase of SNR as will be shown in the following section.

4.4 Power considerations for thermal light sources

In this section, we will calculate the theoretical brightness of a thermal light source, and, in turn, the power radiated per spatial mode. This figure will enable us to estimate the ultimate theoretical signal to noise ratio in wide-field OCT with a thermal light source. Theoretical and experimental results are compared in a few cases of practical interest. Analysis of theoretical results will lead us to far reaching conclusions.

4.4.1 Theory

An ideal thermal source emits blackbody radiations with a spectral energy distribution given by Planck's law [11]. A change of variable provides the energy distribution $u(\lambda)$ as a function of the wavelength:

$$u(\lambda)d\lambda = \frac{8\pi hc}{\lambda^5} \frac{1}{e^{\left(\frac{hc}{k_B T \lambda}\right)} - 1} d\lambda \quad (5)$$

where T [K] is the absolute temperature of the blackbody radiator, h [J s] the Planck's constant, c [m/s] the speed of light, k_B [J/K] the Boltzmann's constant, and λ [m] the wavelength. Integration over the whole spectrum yields the total energy per unit volume [J/m³]:

$$u_{tot} = \int_0^{\infty} u(\lambda)d\lambda \quad (6)$$

Knowing that $P = (c/4) u_{tot}$ [11], the power radiated per unit area P [W/m²] can be obtained by combining this equation with Eq. (5) and (6):

$$P(\lambda, T) = 2\pi hc^2 \int_{\lambda_1}^{\lambda_2} \frac{1}{\lambda^5 (e^{\left(\frac{hc}{k_B T \lambda}\right)} - 1)} d\lambda \quad (7)$$

The total power radiated per unit area can be calculated by integrating over the whole spectrum, i.e. between $\lambda_1 = 0$ and $\lambda_2 = \infty$, which leads to a classical analytical expression. Indeed, replacing λ by $\frac{hc}{k_B T \cdot x}$ the integration term becomes $\int_0^{\infty} \frac{x^3}{e^x - 1} dx$ which is a 3rd order Riemann-Zeta function

whose exact value is $\frac{\pi^4}{15}$.

The final result is the well known Stephan-Boltzmann's law which provides the overall power radiated per unit surface under 2π steradians

$$P_{tot}(T) = \frac{2\pi^5 k_B^4}{15h^3 c^2} T^4 = \mathbf{s} \cdot T^4 \quad (8)$$

where the constant $\mathbf{s} = 5.67 \cdot 10^{-8}$ [Wm⁻²K⁻⁴]. Remarkably, the radiated power depends only on the temperature of the source.

Assuming a homogeneous source, we will now calculate the amount of coherently radiated power, that is the power radiated in a single spatial mode. Dividing Eq. (8) by 2π yields the brightness, i.e. the power per unit surface and steradian [$\text{W m}^{-2} \text{sr}^{-1}$]. The universal relationship: $I^2 = A_c \Omega$ (see 2.1.3) sets a fundamental upper limit to the geometrical extent a single mode can occupy (solid angle Ω [sr] and surface A_c [m^2]). The power per spatial mode P_M radiated by a thermal source is then equal to the product of the brightness by the mode spatial extent:

$$P_M(I, T) = \frac{1}{2\mathbf{p}} \cdot P(I, T) \cdot A_c \Omega = hc^2 \int_{I_1}^{I_2} \frac{1}{I^3 \left(e^{\left(\frac{hc}{k_B T I} \right)} - 1 \right)} dI \quad (9)$$

The integration of the power per mode radiated by the whole spectrum can again be reduced to an analytical expression. Indeed, replacing λ by $\frac{hc}{k_B T \cdot x}$, the integration becomes $\int_0^{\infty} \frac{x}{e^x - 1} dx$ which is a 1st order Rieman-Zeta function whose exact value is $\frac{\mathbf{p}^2}{6}$

The final result is the counterpart of the Stephan-Boltzmann's law for one spatial mode:

$$P_{Mtot}(T) = \frac{\mathbf{p}^2 K^2}{6h} T^2 = \mathbf{x} \cdot T^2 \quad (10)$$

where the constant $\mathbf{x} = 4.73 \cdot 10^{-13}$ [W/K^2].

Interestingly, this equation reveals that the overall power per spatial mode is proportional to the square of the absolute temperature and not to the fourth power for the brightness like in Stephan Boltzmann's law. This means that the increase of power per mode with temperature is considerably slower than the corresponding increase in brightness. Moreover, at a given temperature, the maximum power per mode as a function of the wavelength is at higher wavelength than the spectral peak of a blackbody radiator. Fig. 12 shows both the power per mode $P_M(I, T)$ and the brightness $P(I, T)$ for a 6000 K blackbody radiator as a function of the wavelength. The important peak shift between these two curves has far reaching consequences for OCT.

The peak of a blackbody radiator spectrum is predicted by Wien's displacement law:

$$I_{\max} = \frac{C}{T} \quad (11)$$

where $C = 2.9 \cdot 10^{-3}$ [m K].

We derived an expression providing the maximum power per mode as a function of the wavelength, that we shall call here the "modal peak displacement law" by analogy to Wien's displacement law. These two laws differ only in their constants. The "modal peak displacement law" yields:

$$I_{M\max} = \frac{\mathbf{c}}{T} \quad (12)$$

where $\mathbf{c} = 5.1 \cdot 10^{-3}$ [m K].

At 6000 K Eq. (11) and (12) yield $I_{\max} = 483$ nm and $I_{M\max} = 850$ nm, respectively.

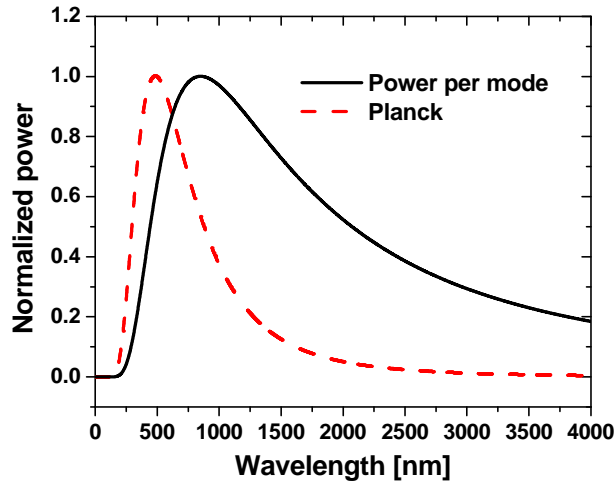


Fig. 12 Blackbody radiation spectrum at 6000 K (Planck) and the corresponding power per mode (Power per mode).

4.4.2 Results and analyses

The power per mode calculated with Eq. (10) for the whole spectrum of a 3300 K and 6000 K blackbody radiator is given in Table 1. However, in practice, the power radiated by the whole spectrum cannot be collected due to the limited bandwidth of relevant optical components. Eq. (9) allows one to numerically calculate the power per spatial mode between λ_1 and λ_2 corresponding to a relevant spectral region.

We consider a few cases of practical relevance for OCT and compare the performance of a 3300 K against a 6000 K blackbody radiator. It is recognised that OCT detection should be performed within a so called “therapeutic window” extending between 600 and 1300 nm, where biological samples exhibit lower scattering and absorption [12].

Let us consider the three following cases:

- (i) a 300 nm broad spectrum extending between 650 and 950 nm
- (ii) a 300 nm broad spectrum extending between 1000 and 1300 nm
- (iii) the two practical cases described below

The first two cases are purely theoretical while the third case (iii) corresponds to the two following experimental cases. The first one consists of our 6000 K Hg arc lamp with the broadest possible spectral range devoid of insidious spectral lines. In section 4.3, it has been shown that the useful spectrum extends from 600 to 1000 nm leading to an effective spectral bandwidth $\Delta\lambda = 200$ nm (FWHM) and a central wavelength $\lambda_c = 660$ nm, when accounting for the spectral response of our silicon photodetector. Second, we consider the 3300 K halogen lamp used by Fercher et al. for a broad spectral range extending from 300 till 1100 nm. Taking into account the spectral responsivity led to a spectral bandwidth $\Delta\lambda = 320$ nm (FWHM) and a central wavelength $\lambda_c = 890$ nm.

The power per mode has been calculated for all the above described cases with Eq. (9). Results are given in Table 1.

	Spectral range $\Delta\lambda$ [nm]	Power per mode [mW]	SNR [dB]
3300K	[0 - ∞]	5.1	71
	[650 - 950] (i)	0.15	57
	[1000 - 1300] (ii)	0.27	60
	[730 - 1050] (iii)	0.2	59
6000K	[0 - ∞]	17	71
	[650 - 950] (i)	1.8	68
	[1000 - 1300] (ii)	1.7	67
	[590 - 790] (iii)	1.15	66

Table 1. Maximum power per mode and signal to noise ratio (SNR) for various spectral ranges, for a halogen source at 3300 K, and a Hg arc source at 6000 K.

The power per mode for the relevant spectral portion (iii) of the Hg and Halogen lamps is approximately 15 and 25 times lower than with the full spectrum, respectively. This underlines the necessity to take into account only the actual spectral range if realistic estimates are to be obtained.

The values calculated for the 650 - 950 nm bandwidth reveal a very important phenomenon. The power per mode at 6000 K is more than an order of magnitude higher than at 3300 K. From Eq. (10), where the whole spectrum is considered, one would expect a factor difference of around 3.3 ($6000^2/3300^2$), given the power per mode dependence with the square of the temperature. The shift of the maximum power per mode as a function of the wavelength, given the ‘‘peak modal power displacement law’’ derived in Eq. (12), is responsible for this important difference. To appreciate this effect, the power per mode is plotted as a function of the temperature for 3300 K and 6000 K blackbody radiators, in Fig. 13a and 13b respectively. The position of the curves’ peak relative to the effective spectral bandwidth for the 650 - 950 nm illustrates well the low collection efficiency with the 3300 K source ($\lambda_{Mmax} = 1545$) relative to the 6000 source ($\lambda_{Mmax} = 850$). This result explains how less than a factor of two increase of temperature allows gaining a factor 12 in power, corresponding to more than 10 dB sensitivity in OCT (see 4.4.3 for SNR calculations).

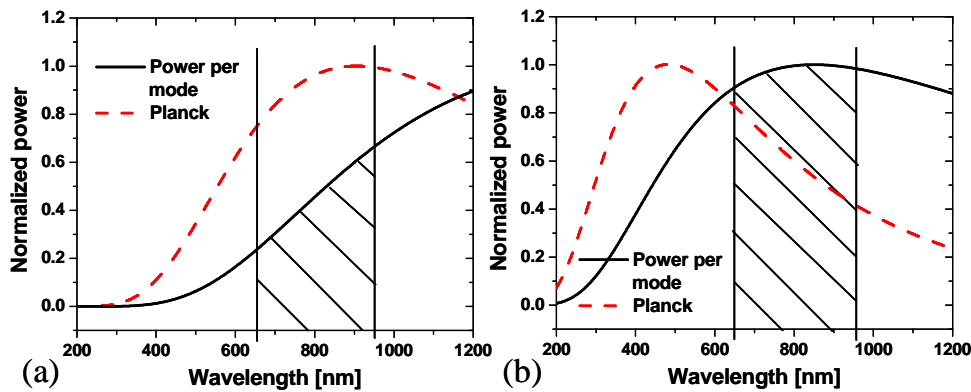


Fig. 13 Power per mode against brightness of a blackbody radiator (Planck) at (a) 3300 K and (b) 6000 K. The hatched area represents the effective spectral bandwidth (650 - 950 nm).

This effect is less pronounced (gain of a factor 6) for the 1000 - 1300 nm bandwidth as expected from the power per mode spectral distribution shown in Fig. 13. For the practical cases considered (iii), a factor difference of 6 is also obtained despite a larger bandwidth at 3300 K than at 6000 K.

This clearly shows that a 6000 K source instead of a 3300 K source can lead to a substantial increase of power, especially when using the spectral region around 800 nm, as is the case in most OCT applications.

This result contrasts with another result found in the literature where the gain of power with the source temperature was under-estimated by calculating the power per mode without accounting for the dependence of the modal spatial extent [7]. The power per mode was approximated by the product of the source brightness with the spatial mode extent corresponding to the peak wavelength of the blackbody spectrum (I_{max}). Thus, the following expression was used:

$$P_{Tot}(T) \cong \frac{1}{2p} P_{tot}(T) (I_{max})^2 \quad (13)$$

With this expression, which does not account for the ‘‘peak modal power displacement law’’, a more modest 3.3 factor of improvement was estimated with a source at 6000 K relative to a source at 3300 K [7]. Note that, in addition, this expression yields values around 6.24 times lower than obtained with Eq. (10), independently of the temperature. The proximity of this value with 2π is a pure coincidence since the constant C of the Wien’s displacement law (present in I_{max}), does not result from products or ratios of physical constants.

We measured the power per mode radiated by our 6000 K arc lamp (200 nm bandwidth) and extrapolated a power of 0.48 μ W i.e. around 2.4 times lower than the corresponding theoretical value (1.15 μ W). This power was measured at the exit of the multimode fiber (see Fig. 2) with the same detector used to measure the autocorrelation function. The power per mode could be obtained by dividing the whole power by the number of modes of the fiber, while knowing the responsivity [A/W] of the detector. The factor 2.4 difference between the experimental and theoretical value can be mainly attributed to coupling losses between the arc and the fiber. However, other factors should also be considered. First, the spectral portion used for calculations, corresponding to the FWHM source spectral bandwidth, provides only an approximation of the radiated power. Second, in our calculations, we assumed that the blackbody emissivity was maximum, i.e. equal to one, whereas a typical emissivity can be easily as low as 0.5. Third, the arc temperature may be an overestimate since the power contained in the intense spectral lines has not been taken into account (see Fig. 8).

Unfortunately, experimental data at 3300 K are missing to provide a relevant experimental confirmation of our calculations.

4.4.3 Signal to noise ratio

We now are in position to derive the maximum signal to noise ratio (SNR) that can be achieved with a thermal light source. Assuming shot noise limited detection, the SNR is directly proportional to the power per spatial mode and inversely proportional to the electronic detection bandwidth BW [13]:

$$SNR = \frac{1}{2} \frac{hI}{hc} \frac{P}{BW}, \quad (14)$$

where h is the detector quantum efficiency, and P the power measured from the sample. For a Gaussian spectrum, the optimal bandwidth can be expressed as [13]:

$$BW = 4 \frac{\Delta I}{I_c} n_D = 8 \frac{\Delta I}{I_c^2} V, \quad (15)$$

where λ_c is the central wavelength, ν_D the Doppler shift frequency, $\Delta\lambda$ the spectral bandwidth (FWHM), and V the scan speed.

The scan speed is the only totally arbitrary parameter to be introduced in the SNR calculation. Since the main advantage of parallel OCT should be fast acquisition speed, we base our calculations on the assumption of video-rate acquisition speed. Thus, assuming a scan length of 1 mm and acquisition in both scan directions, the scan speed is $V = 25$ mm/s.

We calculated SNR values for the cases investigated (Table 1). The power P used in Eq. (14) corresponds to a quarter of the power per mode to account twice for the 50% beamsplitter transmission. Coupling and transmission losses of other optical components are not included.

For the full spectrum we assumed a λ_c corresponding to the central wavelength λ_{max} of the blackbody peak radiation given by the Wien's displacement law. We also assumed that the optical frequency bandwidth $\Delta\nu$ is inversely proportional to the coherence time t_c , which, for a blackbody radiator, is given by [14]:

$$t_c = \frac{h}{2p k_B T} \quad (16)$$

Combining Eq. (14),(15), and (16) and knowing that $\Delta\lambda = \Delta\nu \lambda_c^2/c$, leads to the following analytical expression for the SNR.

$$SNR|_{\Delta\lambda \rightarrow \infty} = \frac{h c p k_B}{192 h V} \sim 71 \text{ dB}, \quad (17)$$

where $c = 5.1 \cdot 10^{-3}$ [m K] is the constant in the ‘‘modal peak displacement law’’.

Quite surprisingly, this purely theoretical value is independent of the temperature thus setting a fundamental limit to the maximum SNR with a thermal light source. However this limit is of moderate interest since the whole spectrum cannot be used in practice. Therefore, it should not be concluded that there is no advantages in having the warmest possible source. As seen before, it is rather a matter of adjusting the modal peak into the therapeutic window.

However, for the relevant practical case considered, the SNR remains below 70 dB. This sets a serious limitation since most useable images of biological tissues could be obtained only with SNR values above 90 dB [12].

In principle, a higher SNR could be obtained by either increasing the power per mode, or by reducing the scan speed. However, these solutions are practically nearly unworkable. On one hand, the higher power per mode can be obtained only with a hotter source and is known that temperature above 6000 K are difficult to reach in practice and would anyway require very special and expensive sources. On the other hand, reducing the scan speed would lead to a lower image acquisition speed with the additional risk of falling at frequencies where the 1/f noise dominates.

In summary, our theoretical study revealed that the maximum power per mode is radiated at a higher wavelength than the spectral peak of a blackbody radiator. This leads to the important practical conclusion that, at 6000 K, the maximum power is collected in the therapeutic spectral window used in OCT (600 - 1300 nm), while at 3000 K this peak is shifted out of the therapeutic window leading to important power losses.

The power per mode being limited by physical laws, a compromise between SNR and acquisition speed must be found. Such a trade-off would seriously limit the fast acquisition speed, which is one of the main advantages of wide-field OCT and the main reason for its further development. Although powerful pulsed laser sources could, to a certain extent, avoid resorting to such a compromise, their use is limited by cross-talk generated noise as seen in chapter 3.

In the following section, we will investigate the possibility to combine the advantage of pulsed lasers (high brightness) with the advantage of thermal light source (low degree of spatial coherence).

4.5 Wide-field OCT with a pseudothermal light source

In Chapter III, we showed that spatially coherent illumination in wide-field OCT can generate a considerable amount of coherent optical cross-talk. In section 4.2 we demonstrated that cross-talk can be suppressed with spatially incoherent illumination provided by a thermal light source. However, the theoretical investigation presented in section 4.4 revealed that the power per spatial mode radiated by thermal light sources, prevents wide-field OCT with a high acquisition speed and sufficient sensitivity. Thus, presently, the wide-field OCT method has a fundamental limit no matter what type of light source is used.

An ideal source for wide-field OCT would consist of a powerful spatially incoherent light source. Such source properties can be obtained by destroying the spatial coherence of a powerful laser so as to obtain a so-called pseudothermal light source [15]. This can be achieved, for instance, by moving a transparent diffuser across the coherent beam path. However, a complete loss of spatial coherence is difficult to obtain in practice. Indeed, the loss of correlation between electromagnetic disturbances, i.e. the loss of spatial coherence, requires a sufficient averaging of phase random fluctuations as explained in section 2.1.1. Generally, the time scale of the generated field random fluctuations must be short enough to ensure sufficient statistical averaging for efficient cross-talk suppression. This requirement is hard to meet in OCT since the measurement time per voxel is relatively short. In the explanations given in section 4.1, we explicitly assumed the absence of correlation between different spatial modes. Such assumption is correct for a thermal light source whose coherent radiation time scale is in the order of the source coherence time, thus allowing sufficient statistical averaging to destroy any correlation between spatial modes.

As discussed at the end of subsection 4.5.1, the potential advantage in terms of brightness of pseudothermal light sources over thermal light sources decreases with the number of pixels used for imaging.

Requirements for the design of a pseudothermal light source providing an efficient cross-talk suppression are defined and explained here below. A preliminary experimental study on pseudothermal light sources in wide-field OCT is also provided.

4.5.1 Method and principle

A simple way to realize a pseudothermal light source is presented in Fig. 14. A superluminescent diode, centered around 810 nm with a bandwidth of 17 nm at FWHM, is coupled to a single mode fiber terminated with an integrated collimator providing a 400 μm large beam (diameter at $1/e^2$) and a power of around 10 mW. The source coherence length leads to an axial resolution of 17 μm . We did not make use of a pulsed laser since the proof of concept presented in this study does not require a very bright source. The beam spatial coherence is destroyed with a holographic diffuser (HD) mounted on a fast rotating motor. The holographic diffuser scatters light forward under an average angle of 10° allowing nearly all light to be collected by the multimode fiber ($\varnothing = 550 \mu\text{m}$, $NA = 0.21$), which is positioned close to the diffuser. In practice, a 75% coupling efficiency could be achieved. The multimode fiber is connected to the interferometer described in section 4.2.1 (see Fig. 2).

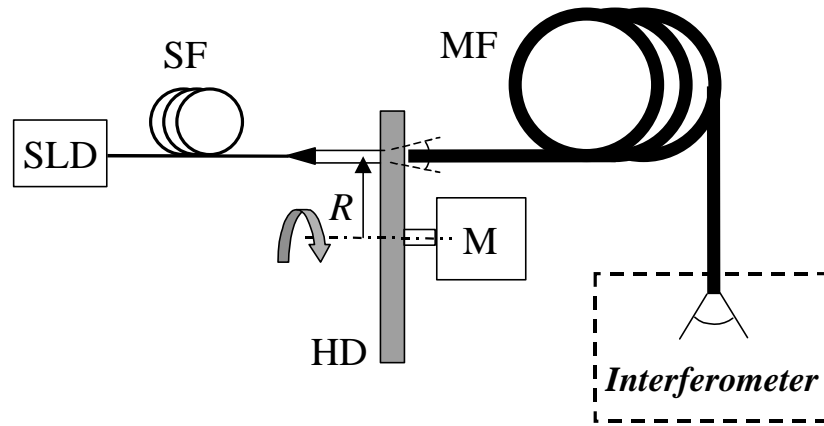


Fig. 14 Scheme of a pseudothermal light source: superluminescent diode (SLD), single mode fiber (SF), 550 μm core multimode fiber (MF), holographic diffusor (HD), rotating motor (M), radial distance (R). The interferometer scheme is shown in Fig. 2 of chapter IV.

Illumination of our diffusor with spatially coherent light generates a speckle pattern with an average speckle size of around 4 μm as determined by the diffusor's scattering angle. The motion of the diffusor creates a time-varying speckle pattern. As the speckle size roughly fills one mode of the multimode fiber, a speckle pattern with identical properties is generated at the multimode fiber exit.

To roughly estimate the fluctuation time scale required for efficient cross-talk suppression, we will analyze the relevant phenomena from the point of view of interfering time-varying speckles.

The time-varying speckle pattern at the multimode fiber exit is imaged on the reference mirror and into the sample. The two speckle patterns are in turn imaged both on the detector located in the detection plane. Interference takes place for each corresponding speckle of the two superimposed patterns. The speckle size matches the size of one detector of the array.

In a first approximation, the cross-talk rejection capability of a pseudothermal light source can be directly related to the number N of different speckles, i.e. different phasors, detected during the time T_D necessary to move from one to the next interference fringe of the OCT correlogram. Indeed, consider a series of N speckle patterns created during T_D , which corresponds to the inverse of the Doppler modulation frequency (6.7 kHz). For the ballistic light component, the phase difference between the reference and the sample arm remains identical, independently of N , and the maximum fringe contrast is obtained. However, for the multiply scattered light component, each individual speckle pattern generates different light propagation paths within the scattering sample. Thus, for a single detector, N speckle patterns generate N phasors with randomly distributed phase differences between the reference and the sample arm. A measurement corresponds to the ensemble average of N uncorrelated phasors, each with a random n th argument $\mathbf{Dy}(n)$. Averaging over cosine terms with arguments $\mathbf{Dy}(n)$ randomly distributed over 2π , yields a zero mean corresponding to complete cross-talk suppression. The average magnitude of cross-talk signals, which are random by nature, corresponds to the standard deviation around the zero mean. When N is extremely large, the standard deviation around the zero mean is negligible leading to nearly complete cross-talk suppression. Such is the case with a thermal light source, which can be considered as a generator of extremely fast time-varying speckle patterns. Here, N is roughly inversely proportional to the source coherence time, typically in the order of 10 femtoseconds, yielding $N \cong 10^{14}$ speckle patterns per second, i.e. $N \cong 10^{10}$ fluctuating speckles during $T_D \cong 150 \mu\text{s}$ in our experimental conditions.

An efficient spatial coherence gating (see 4.2) implicitly relies on a high N value, which is difficult to reach for a pseudothermal light source. Therefore, for a quantitative evaluation of the cross-talk suppression efficiency with a pseudothermal light source, we need to derive a relationship between N and the amplitude of the cross-talk generated current i_{CT} . The finite statistical averaging of the N uncorrelated speckle patterns, added on an intensity basis, leads to a distribution with a constant mean and a standard deviation $\mathbf{s}(N)$. The constant mean is suppressed in the OCT signal processing while $\mathbf{s}(N)$ generates a residual signal proportional to i_{CT} . There is straightforward analogy with the

contrast of a speckle pattern, which is defined by the ratio of the standard deviation to the mean intensity. As seen in section 2.2.1, the phasor amplitude of a sum of uncorrelated speckles obeys a Poisson distribution. Therefore, $\mathbf{s}(N)$ corresponds to the standard deviation of a Poisson distribution, which implies that, in a first approximation, the cross-talk amplitude should decrease with N as follows:

$$i_{CT} \propto \mathbf{s}(N) \propto \frac{1}{\sqrt{N}} \quad (18)$$

Note that the same averaging process, leading to the suppression of random phasors, could be obtained with spatially coherent illumination by averaging a series of N measurements prior to envelope demodulation (see 3.2.6). Here, the ensemble average over random phasors could take place thanks to Brownian motion in the scattering sample inducing different light propagation paths at each measurements. For the case investigated, corresponding to $N = 500$ measurements, the residual signal in Fig. 12 of section 3.2.6, seems indeed lower than the cross-talk signal with spatially coherent illumination by a factor of about 20 ($N^{1/2}$).

4.5.2 Results and discussion

The experiment described for the thermal light source (see 4.2) was repeated with our pseudothermal light source. Fig. 15 shows OCT cross-section images of the pattern's stripes - with the normalized intensity represented along the vertical axis - obtained for spatially coherent illumination with the SLD source (Fig. 15a) and for spatially incoherent illumination with our pseudothermal light source for $\mathbf{n}_{M1} = 10$ Hz and $\mathbf{n}_{M2} = 250$ Hz, generating $N = 50$ (Fig. 15b) and $N = 1250$ (Fig. 15c) speckles during T_D , respectively. Knowing the mean speckle size ΔX_s , the motor rotational frequency \mathbf{n}_M , the Doppler frequency \mathbf{n}_D , and the radial distance R , the number N of single speckles, as observed by one detector, can be calculated from the following equation:

$$N = \frac{2\mathbf{p}\mathbf{n}_M R}{\Delta X_s \mathbf{n}_D} \quad (19)$$

The plots were obtained with 25 demodulated OCT signals.

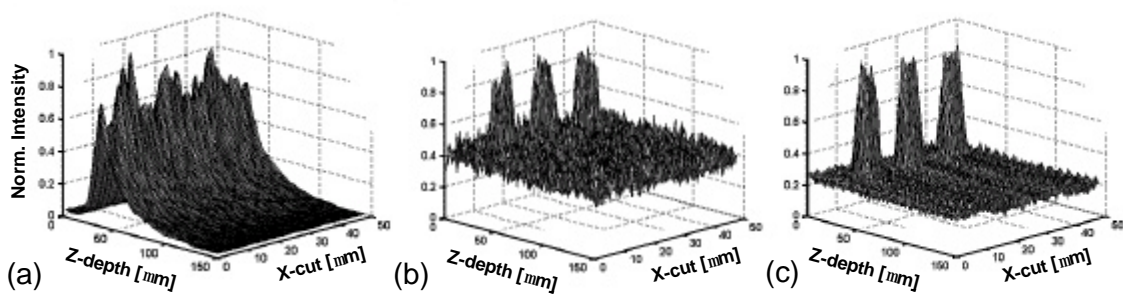


Fig. 15 Cross-section wide-field OCT image of a US air force resolution target covered with scattering solution (8 OD, $g = 0.93$) obtained with: Spatially coherent illumination (a); Spatially incoherent illumination generated by a pseudothermal source with $\mathbf{n}_{M1} = 10$ Hz (b) and $\mathbf{n}_{M2} = 250$ Hz (c). All curves are normalized and correspond to an average of 25 demodulated signals.

With spatially coherent illumination, the reflecting pattern is blurred by cross-talk generated noise. The pseudothermal light source permits to distinguish the 3 reflecting stripes of the pattern. While already visible with a relatively low frequency ($\mathbf{n}_{M1} = 10$ Hz), the 3 reflecting stripes (Fig. 15b) are clearly resolved with a 25 times higher frequency (Fig. 15c). Different rotational speeds were used to

show the influence on cross-talk rejection. However, since they contain a strong background noise generated by our pseudothermal source, these measurements do not provide a valuable demonstration that higher rotational speed leads to better a rejection. Measurements with a sample mirror revealed that this noise corresponds to harmonics generated by the periodicity of our rotating diffuser. Indeed, the noise power spectrum consists of periodic spikes, multiples of the first harmonic of n_M (Fig. 16). Many more harmonics fall within the detection bandwidth (650 Hz with the SLD) for $n_{M1} = 10$ Hz than for $n_{M2} = 250$ Hz. This noise that prevents the experimental verification of the relationship given by Eq. (18).

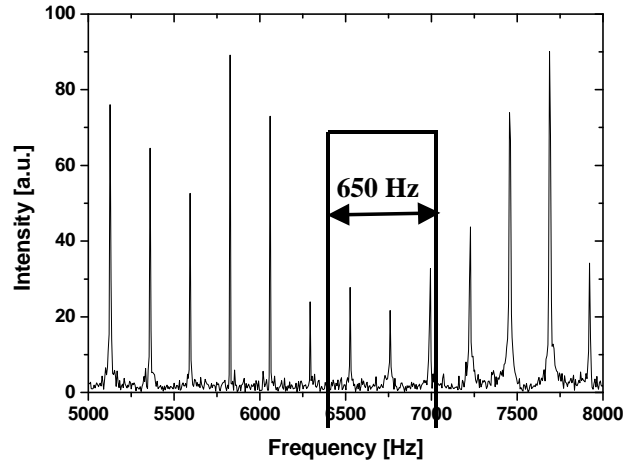


Fig. 16 Harmonics generated by the rotation periodicity of the pseudothermal source diffuser for $n_{M2} = 250$ Hz. The thick lines represent the 650 Hz detection bandwidth centred around the 6.7 kHz Doppler frequency.

To avoid the occurrence of harmonics, a non-periodic speckle pattern should be generated, for instance, by a randomly addressed spatial light phase modulator. However, a modulation frequency in the kHz range as offered by liquid crystal modulators is far too low to permit full cross-talk suppression. The modulation frequency required depends on the amount of cross-talk and on the application. Assuming a modulation frequency of 10 kHz, i.e. $N = 10^4$, cross-talk generated noise would fall only 20 dB lower according to Eq. 18. With arrays of micro-reflectors (SMDs), 25 dB lower cross-talk signals could be obtained. To our knowledge, presently no phase modulator arrays operating in the MHz range or higher, such as electro-optic modulators, is commercially available.

Given these technological limitations a high rotational speed motor could still be a workable solution. To suppress harmonics generated noise, the first harmonic must at least exceed the detection bandwidth and the Doppler frequency must be an odd multiple of the first harmonic frequency divided by two.

It is worth noting that, since the power of a pseudothermal light source is split into many spatial modes, its brightness is limited by the number of pixels in the wide-field, while for a thermal light source, the power per spatial mode depends only on the source temperature. Therefore, a pseudothermal light source is of no advantage when too many of parallel detection channels are employed. For instance, a 1 W pseudothermal source offers an advantage over a thermal light source delivering 1 μ W per spatial mode, only in the case of a wide-field with less than 1000 x 1000 pixels.

4.5.3 Conclusions

We have shown that a pseudothermal light source allows cross-talk suppression in wide-field OCT. Unfortunately, the attractive properties of pseudothermal light sources could be gained at the expense of the simplicity and the economical advantages offered by thermal light sources. In addition, the realization of the high phase scrambling frequency required for a low degree of spatial coherence is

practically difficult to achieve. Moreover, the power per mode of a pseudothermal light source is limited by the number of pixels in the wide-field. Another limitation to bear in mind is the maximum irradiance of biological samples, permitted by ANSI norms. Therefore, a pseudothermal light source could be a valuable solution for some specific cases provided a careful design.

An interesting alternative to pseudothermal light sources could consist of a matrix of temporally low coherent sources [14], where each source would illuminate a single probe volume conjugated to the detector array.

References

- [1] M. Davidson, K. Kaufman, I. Mazor and F. Cohen, "An application of interference microscopy to integrated circuit inspection and metrology," *Proc. SPIE* **775**, 233-341 (1987).
- [2] B.S. Lee and T.C. Strand, "Profilometry with a coherence scanning microscope," *Appl. Opt.* **29**, 3784-3788 (1990).
- [3] M.G. Somekh, C.W. See and J. Goh, "Wide field amplitude and phase confocal microscope with speckle illumination," *Opt. Com.* **174**, 75-80 (2000).
- [4] P.-C. Sun and E.N. Leith, "Broad-source image plane holography as a confocal imaging process," *Appl. Opt.* **33**, 597-602 (1994).
- [5] W. Drexler, U. Morgner, F.X. Kärtner, C. Pitris, S.A. Boppart, X.D.Li, E.P. Ippen, and J.G. Fujimoto, "In vivo ultrahigh-resolution optical coherence tomography," *Opt. Lett.* **24**, 1221-1223 (1999).
- [6] B. Povazay, K. Bizheva, A. Unterhuber, B. Hermann, H. Sattmann, A.F. Fercher, W. Drexler et al., "Submicrometer axial resolution optical coherence tomography," *Opt. Lett.* **27**, 1800-1802 (2002).
- [7] A.F. Fercher, C.K. Hitzenberger, M. Sticker, E. Moreno-Barriuso, R. Leitgeb, W. Drexler and H. Sattmann, "A thermal light source technique for optical coherence tomography," *Opt. Com.* **185**, 57-64 (2000).
- [8] L. Vabre, A. Dubois, and A. C. Boccara, "Thermal full-field optical coherence tomography," *Opt. Lett.* **27**, 530-532 (2002).
- [9] D.L. Marks, A. L. Oldenburg, J. J. Reynolds and S. A. Boppart, "Digital algorithm for dispersion correction in optical coherence tomography for homogeneous and stratified media," *Appl. Opt.* **42**, 204-216 (2003).
- [10] A.F.Fercher, C.K Hitzenberger, M. Sticker, R. Zawadzki, B. Karamata, and T. Lasser, "Numerical dispersion compensation for Partial Coherence Interferometry and Optical Coherence Tomography," *Opt. Exp.* **9**, 610-615 (2001).
- [11] L. Mandel et E. Wolf, "Optical coherence and quantum optics", Cambridge University Press, (1995).
- [12] A.F. Fercher, W. Drexler, C.K. Hitzenberger, and T. Lasser, "Optical coherence tomography - principles and applications," *Rep. Prog. Phys.* **66**, 239-303 (2003).
- [13] E.A. Swanson, D. Huang, M.R. Hee, J.G. Fujimoto, C.P. Lin, C.A. Puliafito, "High-speed optical coherence domain reflectometry," *Opt. Lett.* **17**, 151-153 (1992).
- [14] H.P. Baltes, "Inverse Source Problems in Optics," Springer, Berlin, in : H.P. Baltes (Ed.), 119-154 (1978).
- [15] W. Martienssen and E. Spiller, "Coherence and fluctuations in light beams," *Am. J. Phys.* **32**, 919 (1964).
- [16] M. Pollnau, "Broadband luminescent materials in waveguide geometry," *J. Lumin.* 102-103, 797 (2003).

CHAPTER V

Conclusions and perspectives

Our investigations of the potential and limitations of wide-field OCT have revealed the crucial role played by the spatial coherence of the light source. Spatially coherent illumination generates considerable coherent optical cross-talk, which prevents shot-noise-limited detection and diffraction-limited imaging in scattering samples. Thus, since the system is cross-talk rather than shot noise limited, increasing the source brightness with a powerful pulsed laser does not necessarily lead to a better signal-to-noise ratio. The dependence on several parameters of the optical system and on sample properties was investigated in a comprehensive study. Cross-talk increases with the wide-field diameter, numerical aperture, source coherence length and sample optical density; and strongly depends on sample anisotropy. We have shown that spatially incoherent illumination realized with a thermal light source permits cross-talk suppression, i.e. rejection of multiply scattered light to a level comparable to that of point scanning OCT.

We have performed a theoretical study which revealed that the power per spatial mode radiated by thermal light sources is too low to permit a high signal to noise ratio while maintaining a fast acquisition speed. Therefore, wide-field OCT realized with spatially either spatially coherent or spatially incoherent illumination suffers from inherent fundamental limitations. Presently, wide-field OCT devoid of cross-talk cannot compete with point scanning OCT in image acquisition speed, one of the primordial reasons for developing parallel systems.

To tackle this problem, we have investigated the possibility to use a pseudothermal light source in wide-field OCT. We came to the conclusion that, for a limited number of pixels, such a source can potentially lead to wide-field OCT systems devoid of cross-talk, and to an image acquisition speed higher than that of a point scanning OCT system. However, the attractive properties of pseudothermal light sources could be gained at the expense of the simplicity and the economical advantages offered by thermal light sources. Furthermore, fast acquisition speed also relies on a performing smart pixel detector array. Presently, such detectors do not have sufficient sensitivity and their frequency read-out is too low as shown in our feasibility study. Another serious limitation is the maximum exposure time of biological samples imposed by ANSI norms.

To obtain a wide-field OCT system leading to fast 3-dimensional image acquisition, progress must be made both on the source and detector side. Development of a new generation of smart pixel detector arrays is currently underway. More work will need to be done to obtain usable pseudothermal light sources. Another option could be a matrix of temporally low coherent sources, each of which would illuminate a single probe volume conjugated to the detector array. Such sources are currently developed in our institute. However, further investment into these developments should be driven by relevant applications in life science or elsewhere. So far, this has not been the case. Given the high acquisition speeds reached with phase delay lines OCT systems, the need for faster volumetric acquisition should be carefully evaluated.

We have performed a theoretical investigation of the potential of thermal light sources in terms of axial resolution and power per mode. The former has revealed that the maximum power per mode is radiated at a wavelength higher than the spectral peak of a blackbody radiator. This has led to the important practical conclusion that, at 6000 K, the maximum power is collected in the therapeutic spectral window used in OCT (600 - 1300 nm), while at 3000 K this peak is shifted out of the therapeutic window leading to significant power losses. More generally, our work provides a design tool for choosing the optimal thermal light source for a given therapeutic window in terms of signal-to-noise ratio.

Currently available sources at 6000 K consist of high pressure gas arc lamps providing a spectrum endowed with spectral lines deleterious for OCT. By filtering a portion of the spectrum devoid of spectral lines of a mercury arc lamp, we obtained amongst the highest axial resolution so far reported in OCT.

To the contrary of the widespread belief that a relevant OCT model should account for a partial correlation between interfering fields, we have explained why multiple scattering does actually not induce a loss of spatial coherence of the sample field and shown that the latter is stationary relative to measurement time. This means that the reference and sample fields are fully correlated, and thus interfere with the maximum contrast.

Based on this important result, we have developed a new comprehensive model of OCT where the signal is modeled as a sum of stationary random phasors and treated as a statistical signal. The mean of this signal can be calculated thanks to classical results of statistical optics and to a Monte Carlo simulation. The latter, which is necessary to calculate the raw spatio-temporal distribution of light, makes our model semi-analytical. It is the prize one has to pay for accessing ranges where the diffusion approximation is not verified. Though this removes the elegance of a fully analytical model, it offers the advantage of a high versatility. Indeed, unlike fully analytical models, it is neither restricted to strongly simplified media nor limited by initial assumptions, such as for instance by the diffusion approximation or by the small angle approximation. Moreover, the application of our model is simplified for samples with complex sub-micrometric structures such as most biological samples. Unlike in other models, the source autocorrelation function is accounted for.

Our model was tested against a whole range of experimental data in a comprehensive study of optical cross-talk in wide-field OCT. Very good agreement between theoretical and experimental results was obtained for a wide range of optical system parameters and sample properties.

Our results put in question the applicability of OCT models based on the extended Huygens-Fresnel principle, which involve spatial coherence effects. Indeed, these models rest on the assumption of partially coherent interfering fields, a hypothesis not met in most practical cases in OCT as shown in our study.

In addition, our investigation adds more weight to OCT models based on Monte Carlo simulations. Indeed, the latter models, believed to describe a “worst case scenario” since they implicitly assume that all multiply scattered light within the coherence length interferes, may well provide a more accurate description than expected.

We do hope that our study and model will help to fully appreciate the role of multiple scattering in OCT and stimulate the research in this field. Future work of interest with our model could be a study of multiple scattering effects in point scanning OCT as well as in the Fourier domain OCT for parallel acquisition of cross-sectional images. The stripe illumination necessary for the latter case should generate cross-talk. Polarization effects could also be included in the model. Conclusions of our study

may well concern a wider class of imaging methods limited by cross-talk, such as for instance parallel time-resolved detection or laser Doppler imaging.

Furthermore, the importance of the speckle statistics in OCT has incited us to clarify the origin of a difference between two theoretical results reported in the literature. Indeed, two calculations of the amplitude distribution of speckles in OCT, each of them based on a different mathematical formulation, yield different results. We have shown that a modification of an initial assumption in one of the formulation leads to equivalent results.

In conclusion, a careful consideration of the coherent properties of light has allowed us to (i) deepen our understanding of the potential and limitations of wide-field OCT, (ii) derive important design rules, and (iii) develop a relevant model of OCT putting in question other widely used models.

Acknowledgements

I am very grateful to Prof. Theo Lasser for his trust and for the freedom he gave me in my research activities. Many thanks to Prof. A.C. Boccara for critically reviewing my work, to Prof. R. Dändliker for his availability and the very fruitful discussions we had in Neuchâtel, to Prof A.F. Fercher for the spontaneous collaboration he offered during his stay at our institute, and to Dr. M. Kempe for his numerous valuable comments.

I am immensely grateful to Patrick Lambelet for his precious explanations and guidance throughout my thesis. His deep understanding of physics and unique way of making things simple largely influenced this work and hopefully will continue to influence me in the future.

No doubt that the stimulating scientific and international atmosphere of the LOB group contributed both directly and indirectly to the success of this thesis. Many thanks to the following people:

My first day colleague, Markus Laubscher, with whom I shared daily scientific problems as well as dreams for a better world. His pragmatism, readiness to help and unique enthusiasm both at work and outside make him the ideal colleague and a long lasting friend. Marcel Leutenegger, the man who talks to and understands computers, for the enormous and spontaneous help he provided me on Monte Carlo programming issues. Kai Hassler for his statistical insights and for taking, when I couldn't, advantage of the snowy mountains for the two of us. Stéphane Bourquin for his wise senior advice and vital help in the final rush. Luc Froehly for memorable discussions on the intelligence of photons and light. Jelena Mitic for sharing equipment and music in the lab. Antonio Lopez for all the good squash games we had. Judith Chaubert for her availability and help. And last but not least, my dear two office mates: Alexander Serov and Ramachandra Rao, as well as Tiemo Anhut, Michael Goesh, and Adrian Bachmann, for the scientific discussions and good time we spent.

Not forgetting the alumni: Sebastian Favre for keeping his sense of seriousness under all circumstances. Mathieu Ducros for his help in the lab, "ratatouille" and fearsome "pointé à la pétanque". Karsten Plamann for sharing his passion of physics, for anything from French orthographic subtleties to good wine. Francois Vuille for being my "Coupe des vices" often triumphant partner.

And once again Theo for, under all circumstances, showing all of us the way to the Mont-Blanc.

This work is also the fruit of the numerous interactions I had within the institute (whatever its ever-changing name may now be). My gratitude goes in particular to the following people:

Prof. R.P. Salathé, the head of the institute, for his availability and scientific insight. Thomas Sidler for generously sharing the richness of his Alibaba optics cave, as well as for his constant availability and help. Thierry Blu for reminding me some basics of mathematics from time to time, but always at the right time. Christian Depeursinge for his kindness and interest in my work. Ronald Gianotti for efficiently helping me with electronics problems including ghost* tracking in my lab (*mysterious electro-magnetic noise). Senor Don Salamanca for being a friendly and helpful webmaster, without being a nerd. Michel St-Ghislain for being my Spanish master and glue adviser. Manuelle Borruat for her friendliness and holographic lemon pies. Tristan Colomb for his LabView assistance and Etienne Cuche for never mentioning "le Chasseral" in our many (170 meters long) corridor discussions. Tristan Bret for his unique enthusiasm for anything from science to a good chess game, as well as for his precious feedback on my public presentation.

Last but not least, many thanks to my friends for having kept me away from my thesis as often as possible.

To my parents and my wife Jelena: thank you for being there for me when I needed you most.

Curriculum Vitae

Boris KARAMATA

Swiss/British, born 11.04.70, married

boris.karamata@a3.epfl.ch



Academic background

- 2000-2004* PhD in biomedical optics at the Institute of Applied Optics, Swiss Federal Institute of Technology (EPFL).
- 1990-1995* Degree in microtechnical engineering, EPFL. Diploma work within Erasmus on a laparoscopic sensor in Pisa (Italy).
- 1986-1989* High School, scientific section - Gymnase du Bugnon, Lausanne, Switzerland.

Professional experience

- 1998-1999* National Microelectronics Research Center (NMRC - Ireland). Design of a miniaturised electro-mechanical device for biological fluid actuation and analysis.
- 1997-1998* Research and Technology Center of the European Space Agency (ESTEC - The Netherlands). Analysis and design of novel sub-systems for satellites.
- 1996-1997* EPFL, contracted by Ciba-Vision (Novartis). Design, manufacture and test of an innovative instrument devoted to ophthalmology.

Languages

French:	Mother tongue
English:	Fluent
Spanish:	Very good
German:	Good
Italian:	Good

Hobbies

Sport (badminton, basketball, hiking, snowboarding), photography, chess.

Publications

- B. Karamata, M. Laubscher, P. Lambelet, and T. Lasser, “A pseudothermal light source for optical coherence tomography”, *Optics Letter*, *in preparation*
- B. Karamata, K. Hassler, M. Laubscher, and T. Lasser, “Speckle statistics in optical coherence tomography”, *JOSA A submitted*
- B. Karamata, P. Lambelet, M. Laubscher, M. Leutenegger, S. Bourquin and T. Lasser, “Multiple scattering in optical coherence tomography. Part I: Investigation and Modeling”, *JOSA A submitted*
- B. Karamata, M. Leutenegger, P. Lambelet, M. Laubscher, S. Bourquin and T. Lasser, “Multiple scattering in optical coherence tomography. Part II: Experimental and theoretical investigation of cross-talk in wide-field optical coherence tomography”, *JOSA A submitted*
- B. Karamata, M. Laubscher, P. Lambelet, R.P. Salathé, and T. Lasser, “Spatially incoherent illumination as a mechanism for cross-talk suppression in wide-field optical coherence tomography”, *Optics Letters* 29, No 7, 736-738, (2004)
- M. Laubscher, S. Bourquin, L. Froehly, B. Karamata, and T.Lasser, “Spectroscopic optical coherence tomography based on wavelength de-multiplexing and smart pixel array detection”, *Optics Communications* 237, 275-283 (2004).
- M. Laubscher, L. Froehly, B. Karamata, R.P. Salathé, and T. Lasser, “Self-referenced method for optical path difference calibration in low-coherence interferometry”, *Optics Letter* 28, No 24, 2476-2478 (2003)
- J. West, B. Karamata, B. Lillis, J.P: Gleeson, J. Alderman, J.K: Collins, W. Lane, A. Mathewson, H. Berney, “Application of magnetohydrodynamic actuation to continuous flow chemistry”, *Lab. Chip*. 2, 2002, 224 - 230, (2002)
- M. Laubscher, M. Ducros, B. Karamata, T. Lasser, and R.P. Salathe, “Video-rate three-dimensional optical coherence tomography”, *Optics Express* 10, No 9, 429-435 (2002)
- M. Ducros, M. Laubscher, B. Karamata, S. Bourquin, T. Lasser, R.P: and Salathé, “Parallel optical coherence tomography in scattering smart-pixel detector array”, *Optics Communications* 202(1-3), 29-35 (2002)
- A.F. Fercher, C.K. Hitzenberger, M. Sticker, R. Zawadzki, B. Karamata, and T. Lasser, “Dispersion compensation for optical coherence tomography depth-scan signals by a numerical technique”, *Optics Communications* 204(1-6), 67-74 (2002)
- B. Karamata, M. Sickenberg, H. Van den Bergh., “A fibreoptic light distributor for the preventative photodynamic therapy of secondary cataract”, *Lasers in Medicine and Science* 15, 238-245 (2000)
- B. Karamata, "Design and prototype of an innovative micro-dosing device for delivery of lubricant into space mechanisms", *ESA-report: EWP-1998*.
- B. Karamata, “Investigation on micro-motors for space applications”, *ESA-report: EWP-1945*, 1997.

Conference proceedings

B. Karamata, M. Laubscher, P. Lambelet, T. Anhut and T. Lasser, "Sources for optical cross-talk suppression in wide-field optical coherence tomography", SPIE vol. 5316, 2004

T. Anhut, B. Karamata, T. Lasser, M.G. Raymer, and L. Wenke, "Measurement of scattered light Wigner functions by phase space tomography and implications for parallel optical coherence tomography", Proc. SPIE, vol 4956, 120-128, 2003

M. Laubscher, M. Ducros, B. Karamata, and T. Lasser, "Video-rate high-resolution parallel optical coherence tomography", Coherence Domain Optical Methods in Biomedical Science and Clinical Applications VI 3(11), 107-110, 2002

M. Laubscher, M. Ducros, B. Karamata, S. Bourquin, and T. Lasser, "High-resolution parallel optical coherence tomography in scattering samples", Photon Migration, Optical Coherence Tomography, and microscopy 2(31), 335-340, 2001

Patents

Lubrication system for a mechanism in particular for rotary bearing in a spacecraft, No 6.085.871, (ESA-Estec)

Device and method for irradiating patient's eye for photodynamic therapy, WO 99/04857, Novartis